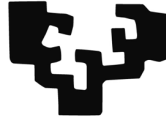


eman ta zabal zazu



Universidad  
del País Vasco

Euskal Herriko  
Unibertsitatea

DEPARTAMENTO DE FISICA DE MATERIALES - MATERIALEN FISIKA SAILA

# **Functionalization of Nanomaterials by Atomic Layer Deposition**

**By Fan Yang**

Academic Dissertation

Supervisor: Mato Knez

2016, July



This PhD thesis has been performed at:



CIC nanoGUNE Consolider

Nanomaterials group

Donostia-San Sebastián, SPAIN

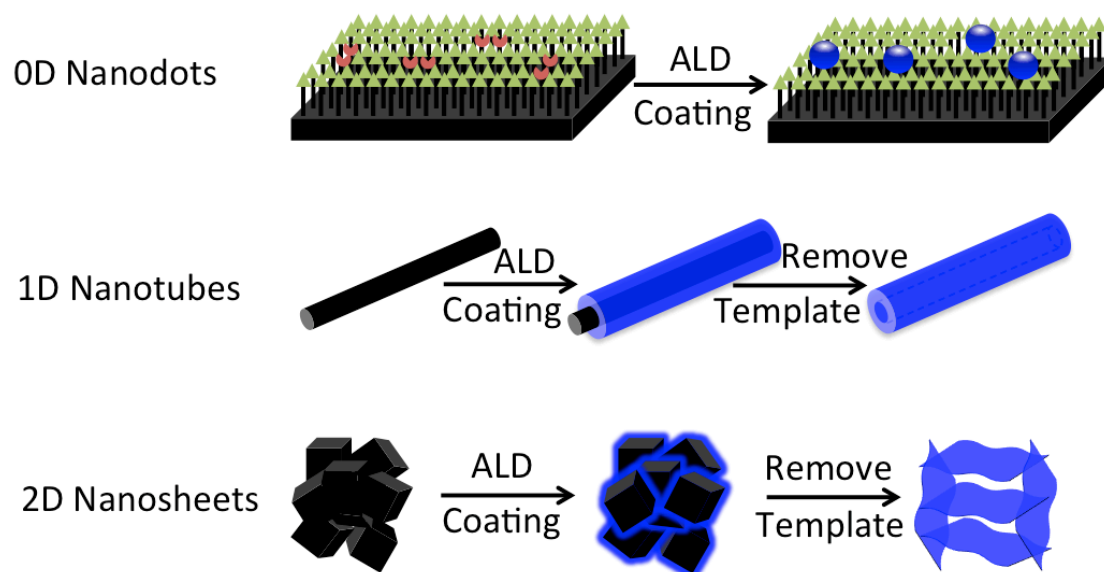


---

# Resumen

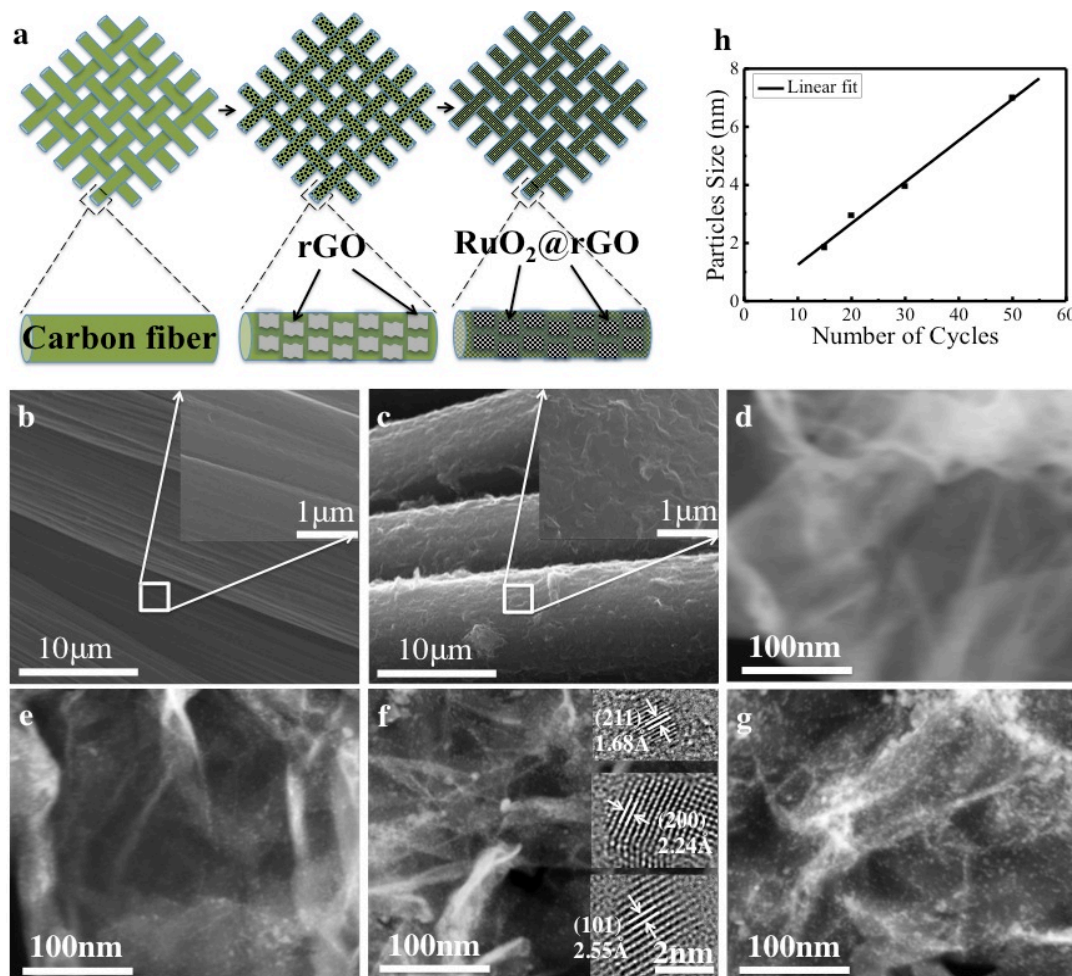
La deposición de capas atómicas o “Atomic Layer Deposition” (ALD) es una técnica sencilla pero poderosa para el recubrimiento y la modificación de los nanomateriales. El proceso se basa en la reacción sólido-gas, en la cual los precursores se introducen por separado en fase gaseosa y reaccionan con la superficie sólida. La introducción de los precursores por fases o ciclos, lleva finalmente, al crecimiento controlado del material deseado. Este mecanismo de trabajo especial, presenta ventajas prometedoras como la alta precisión del espesor, el crecimiento no direccional y la alta uniformidad en comparación con otros métodos de recubrimiento como la Deposición Química de Vapor o CVD (de sus siglas en inglés Chemical Vapor Deposition). Ocasionalmente se suele llevar a cabo un proceso de ALD modificado, llamado infiltración en fase vapor, en el que se introduce y se infiltra un precursor metálico en materiales blandos. Esto a menudo produce interesantes alteraciones en las propiedades intrínsecas de los materiales, incluyendo las propiedades eléctricas, mecánicas, ópticas, etc. Tanto el recubrimiento como la infiltración a través del ALD son cada vez más interesantes para la ciencia de los materiales. Esta tesis estudia desde los aspectos fundamentales del mecanismo de reacción entre los precursores y los grupos funcionales en el ALD, hasta el crecimiento de nanopartículas y la fabricación de nanoestructuras a través del ALD.

En la primera parte de esta tesis, se presenta un método sintético para fabricar distintas nanoestructuras basados en ZnO incluyendo nanopartículas 0D, nanotubos 1D y nanoláminas 2D a través de ALD y de la elección de diferentes plantillas. Por ejemplo, moléculas hidrófobas e hidrófilas son auto-ensambladas como plantillas. Las nanopartículas de ZnO se sintetizan en las zonas hidrófilas de la superficie mediante ALD. Usando nanofibras electrohiladas o nanocubos de NaCl como plantilla, se obtienen nanotubos de ZnO 1D y nanoláminas 2D de ZnO por medio del crecimiento de ZnO con ALD y la posterior eliminación de la plantilla. Esta ruta sintética usando el ALD ofrece nuevas posibilidades para la síntesis sencilla de nanoestructuras, con varias aplicaciones potenciales.

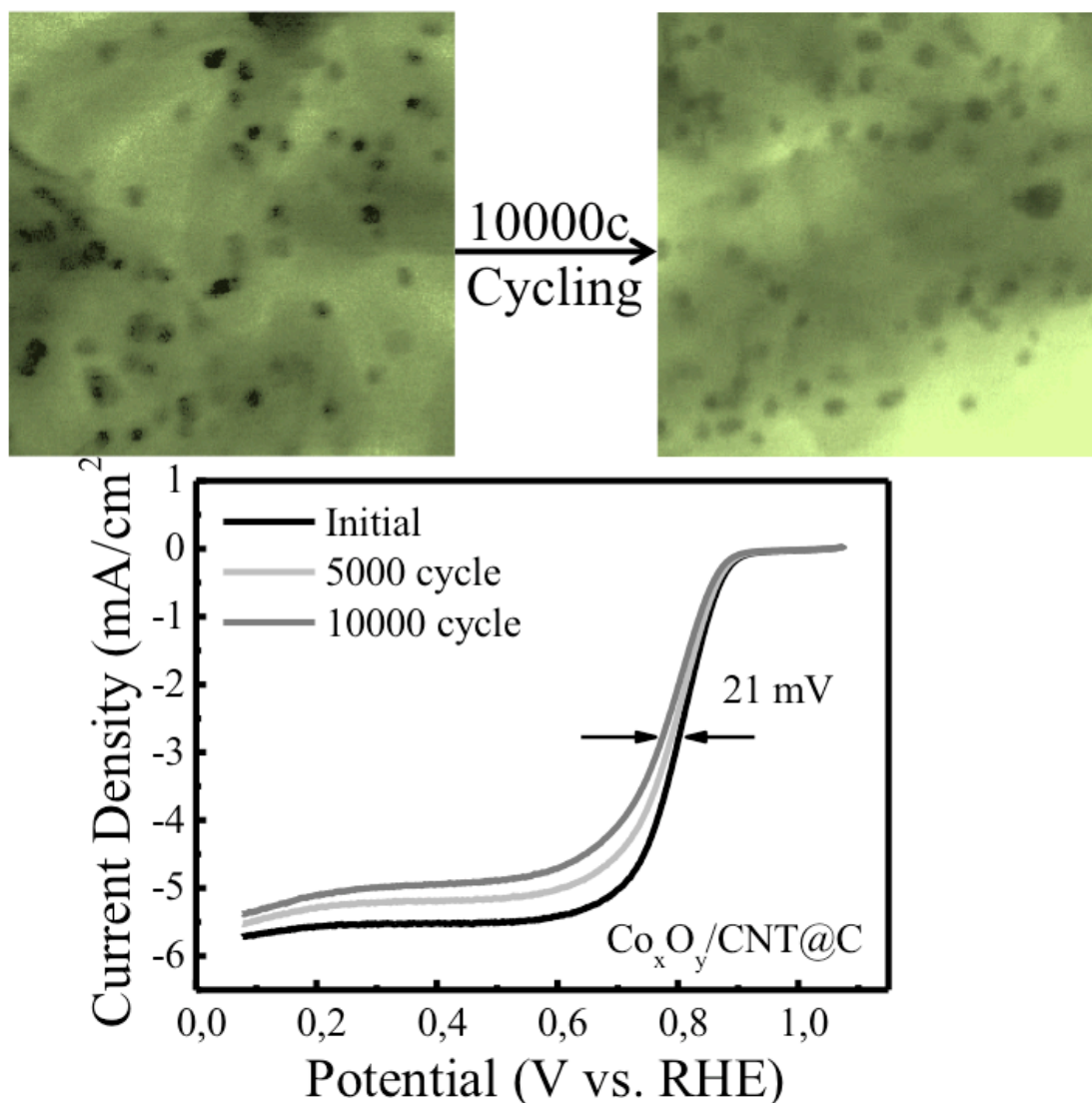


Esquema de la síntesis de ZnO de 0D a 2D basado en la deposición de capa atómica de nanoestructuras. Moléculas hidrófobas e hidrófilas son auto-ensambladas como plantillas. Las nanopartículas de ZnO se sintetizan en las zonas hidrófilas de la superficie mediante ALD. Usando nanofibras electrohiladas o nanocubos de NaCl como plantilla, se obtienen nanotubos de ZnO 1D y nanoláminas 2D de ZnO por medio del crecimiento de ZnO con ALD y la posterior eliminación de la plantilla.

En la segunda parte de la tesis, se estudia la funcionalización a través del ALD de los nanomateriales basados en el carbono, como el grafeno o los nanotubos de carbono. El primer ejemplo es describir métodos de gestión de defectos en el grafeno. Debido a su alta conductividad y área superficial, el grafeno es un candidato prometedor para ser usado como electrodo en aplicaciones electroquímicas, como por ejemplo supercondensadores. Sin embargo, el grafeno contiene a menudo defectos derivados del proceso de producción, que producen un efecto negativo sobre el comportamiento electroquímico final. A través de ALD, y debido a su mecanismo especial, se depositan con precisión nanopartículas de  $\text{RuO}_2$  en los defectos del grafeno. Después de reemplazar los defectos con nanopartículas de  $\text{RuO}_2$ , la actuación capacitiva de grafeno, incluyendo la capacitancia y la estabilidad específica se incrementan considerablemente.



(a) Representación esquemática del proceso de fabricación de los electrodos rGO/RuO<sub>2</sub> en tejido de carbono. El primer paso implica la unión de RGO al tejido de carbono por inmovilización electroquímica (ECI). En la segunda etapa se aplica la deposición de capa atómica (ALD) para depositar nanopartículas de RuO<sub>2</sub> en RGO. Imágenes de microscopio electrónico de barrido (SEM) (b) fibra de carbono, y (c) fibra de carbono cubierto con RGO (recuadro con mayor aumento). Microscopio de transmisión electrónica de barrido (STEM) imágenes (d) RGO, (e) RGO / RuO<sub>2</sub>-15, (f) RGO / RuO<sub>2</sub>-20, (g) RGO/RuO<sub>2</sub>-30. El recuadro de (f) muestra imágenes de HRTEM de nanopartículas de RuO<sub>2</sub>, barra de escala: 2 nm. (h) El promedio del tamaño de las nanopartículas de RuO<sub>2</sub> en función del número de ciclos del proceso.



Imágenes de SEM del catalizador  $\text{Co}_x\text{O}_y/\text{CNT}@C$  antes y después de la prueba de 10000 ciclos. La cifra más baja corresponde a la curva de la LSV  $\text{Co}_x\text{O}_y / \text{CNT} @ C$  a 1 ciclo, 5000 ciclos y 10000 ciclos.

El segundo ejemplo se realiza con nanotubos de carbono. Los nanotubos de carbono son conocidos por su alta conductividad y su alta actividad electro-catalítica. El ALD se aplica para la deposición de nanopartículas de  $\text{Co}_3\text{O}_4$  en nanotubos de carbono. El  $\text{Co}_3\text{O}_4 / \text{CNT}$  muestra una excelente actividad para la reacción de reducción de oxígeno (ORR), que puede ser una alternativa prometedora para los catalizadores caros a base de platino. Una capa de carbono dopado con nitrógeno cubre las nanopartículas  $\text{Co}_3\text{O}_4$  para su inmovilización. El compuesto final muestra una excelente reactividad, así como una estabilidad excepcional para la ORR. Estos dos ejemplos muestran que el ALD tiene grandes ventajas, como la distribución

uniforme de la posición y el tamaño de nanopartículas, y un control preciso de la densidad de las nanopartículas depositadas. Como prueba de concepto, también se espera que en el futuro el ALD sea una técnica prometedora para depositar nanopartículas funcionales, para que sean utilizadas en aplicaciones de energía, de catálisis o de detección.

Por último, se estudian los aspectos fundamentales de la interacción entre los precursores de ALD y grupos funcionales orgánicos. Tres grupos funcionales son elegidos para el estudio de la interacción con el precursor trimetilaluminio (TMA) -OH, -NH<sub>2</sub> y -NO<sub>2</sub>. Se ha descubierto que el precursor de TMA muestra mayor afinidad con los átomos más ricos en electrones del grupo funcional, a los cuales se une. A continuación, se necesita energía adicional para la activación de la reacción entre los grupos metilo del TMA y los H de los grupos funcionales. El último estadio de la reacción depende seriamente de esta barrera de energía de activación. Con el grupo -OH el TMA se quimioabsorbe al -OH y forma una unión Al-O estable; en el caso del -NH<sub>2</sub>, TMA sólo se absorberá al N en condiciones normales, y la unión Al-N sólo se formará cuando se le proporcione energía externa. Para -NO<sub>2</sub>, el TMA solo se adsorberá al O y permanecerá así hasta que no haya H para reaccionar con el grupo metilo del TMA. Si el TMA se adsorbe a los grupos -NH<sub>2</sub> o -NO<sub>2</sub>, los intermediarios serán inmediatamente adheridos si se exponen a la humedad, ya que el TMA reaccionará con los grupos -OH del agua del aire. Esta comprensión de la interacción entre el TMA y los grupos funcionales sin duda será de gran ayuda para el crecimiento controlado de materiales híbridos orgánico-inorgánico o la infiltración en materiales blandos mediante ALD.

En conclusión, el trabajo y la investigación realizada en esta tesis se basan en la tecnología ALD. Por todos los ejemplos, experimentos y resultados que se muestran en esta tesis, se quiere transmitir la idea de que el ALD es una tecnología muy prometedora para la ciencia y desarrollo de los materiales. Se puede utilizar no sólo como una técnica de recubrimiento de película delgada, sino también como una herramienta completa para la deposición de nanopartículas, la fabricación de varias nanoestructuras o la modificación de materiales blandos. La comprensión fundamental del mecanismo de interacción a nivel molecular sin duda ayudará a optimizar el proceso y a una funcionalización controlada de los materiales.



---

# Abstract

Atomic Layer Deposition (ALD) is a powerful technique for the coating of nanomaterials and their modification. The process is based on gas-solid reactions, where precursors are separately introduced in the gas phase and bound to the solid surface. Introduction of a precursor and a counter precursor in a cycle-by-cycle manner, finally leads to a controlled growth of the desired material. This special modus operandi leads to great advantages like high accuracy in thickness, non-in-sight growth and high uniformity compared to other coating methods like Chemical Vapor Deposition (CVD). Sometimes a modified ALD process, called vapor phase infiltration, is also performed, where a metal precursor is introduced to infiltrate soft materials. This often leads to significant alternation of those materials' intrinsic properties including electrical, mechanical, optical or other properties. Both coating and infiltration through ALD technology has become more and more interesting for material science. This thesis studies fundamental aspects regarding the reaction mechanisms between precursors and functional groups that occur in the process, controlled nanoparticle growth and nanostructure fabrication by ALD.

In the first part of this thesis, an ALD-based synthetic method to fabricate various ZnO-based nanostructures including 0D nanodots, 1D nanotubes and 2D nanosheets controlled by the choice of different templates is presented. For example, hydrophobic and hydrophilic molecules are self-assembled onto a substrate and used as template. ZnO nanodots are grown exclusively on the hydrophilic sites of the surface by ALD. The use of electrospun nanofibers or NaCl nanocubes as templates and their removal after growth of ZnO by ALD, result in 1D ZnO nanotubes or 2D ZnO nanosheets. This synthetic route through ALD offers new possibilities for easy synthesis of nanostructures, possibly with various application potentials.

In the second part of the thesis, functionalization of carbon-based nanomaterials like graphene and carbon nanotubes by ALD is studied. The first example is describing ways towards defects management on graphene. For its high conductivity and surface area, graphene is a promising material to be used as electrodes in electrochemical applications like supercapacitors. But graphene often contains defects originating from the production process. Those defects often have

negative effects on the electrochemical performance of graphene. RuO<sub>2</sub> nanoparticles are selectively and controlledly deposited on those defect sites, which is enabled by the working principle of ALD. After replacing those defects with RuO<sub>2</sub> nanoparticles, the capacitive performance of graphene including the specific capacitance and electrochemical stability are greatly enhanced. For the second example, carbon nanotubes are used. Carbon nanotubes are known for their high conductivity and electrocatalytic activity. ALD deposition of Co<sub>3</sub>O<sub>4</sub> nanoparticles is applied for the functionalization of carbon nanotubes. The Co<sub>3</sub>O<sub>4</sub>/CNT composites exhibit excellent activity for the oxygen reduction reaction (ORR), showing great promise as an alternative for expensive platinum-based catalysts. A nitrogen doped carbon shell is further deposited to immobilize those nanoparticles. The final composite shows excellent reactivity as well as exceptional stability for the ORR. These two examples show that for nanoparticle deposition ALD shows great advantages over other techniques particularly for a uniform distribution in both position and size, and an accurate and simple control of the size and density of the deposited nanoparticles. It is expected that in future ALD will prove most powerful for depositing various functional nanoparticles, which will be of great interest for energy, catalysis or sensing applications.

In the last part, fundamental aspects regarding interactions between ALD precursors and organic functional groups are studied. Three organic functional groups including –OH, –NH<sub>2</sub> and –NO<sub>2</sub> are chosen for the study of interaction with a typical ALD precursor trimethylaluminum (TMA). We found that the TMA precursor has strong affinity to the electron rich atoms of the functional group, where it binds first. Additional energy is needed for the activation of a reaction between methyl groups from TMA and H from the functional groups. The final state of the reaction seriously depends on this activation energy barrier. For –OH, TMA will chemisorb to the O and form stable Al-O bonds; for –NH<sub>2</sub>, TMA only adsorbs to the N site of –NH<sub>2</sub> at normal conditions, and Al-N bond forms only when additional energy is provided; for –NO<sub>2</sub>, TMA only adsorbs to the O site and remains as such since there is no H to react with the methyl group of TMA. If TMA adsorbs to –NH<sub>2</sub> or –NO<sub>2</sub> groups, the intermediates will be immediately cleaved if exposed to humidity, since TMA will react with the –OH group of water from air. This understanding of the interaction strength between TMA and functional groups will certainly be very helpful for

controlled ALD growth of organic-inorganic hybrid materials or infiltrations into soft materials.

In conclusion, the research performed in this thesis is strongly related to the ALD technology. For all the examples, experimental and calculation results shown in this thesis, we want to convey the idea that ALD is a very promising technology for material science and development. It can be used not only as a thin film coating technique, but also a comprehensive tool for nanoparticle deposition, fabrication of various nanostructures, and sometimes for modification of soft materials. The fundamental understanding of the interaction mechanisms at a molecular level will certainly help us to optimize those processes, and more further towards controlled functionalization of materials.



---

# Contents

|   |     |
|---|-----|
| Resumen .....                                   | i   |
| Abstract .....                                  | vii |
| 1. Introduction.....                            | 1   |
| 1.1 Background .....                            | 1   |
| 1.2 Atomic Layer Deposition .....               | 2   |
| 1.3 Objective and Structure of the Thesis ..... | 7   |
| 2. Experimental Techniques and Methods .....    | 9   |
| 2.1 Electron Microscopy .....                   | 9   |
| 2.2 X-ray Diffractometer .....                  | 11  |
| 2.3 Atomic Force Microscopy .....               | 13  |
| 2.4 Vibrational Spectroscopy.....               | 13  |
| 2.5 Ultraviolet-Visible Spectroscopy.....       | 14  |
| 2.6 X-ray Photoelectron Spectroscopy.....       | 15  |
| 2.7 Electrochemistry.....                       | 15  |
| 3. Nanostructures Synthesis by ALD.....         | 21  |
| 3.1 Introduction.....                           | 21  |
| 3.2 Experiments .....                           | 22  |
| 3.3 Results and Discussion .....                | 24  |
| 3.4 Conclusions.....                            | 30  |
| 4. ALD Functionalization of Graphene .....      | 31  |
| 4.1 Introduction.....                           | 31  |
| 4.2 Experiments .....                           | 33  |
| 4.3 Results and Discussion .....                | 35  |

|  |     |
|--|-----|
| 4.4 Conclusions.....   | 49  |
| 5. Functionalized Nanoparticles on Carbon Nanotubes by ALD ..  | 51  |
| 5.1 Introduction.....  | 51  |
| 5.2 Experiments .....  | 53  |
| 5.3 Results and Discussion .....                               | 55  |
| 5.4 Conclusions.....   | 78  |
| 6. Interactions between ALD Precursor and Functional Groups .. | 79  |
| 6.1 Introduction.....  | 79  |
| 6.2 Experiments .....  | 81  |
| 6.3 Results and Discussion .....                               | 82  |
| 6.4 Conclusions.....   | 100 |
| 7. Conclusions and Future Perspectives.....                    | 103 |
| Bibliography.....  | 105 |
| List of publications .....                                     | 123 |
| Acknowledgements .....   | 125 |

---

# Chapter 1

## Introduction

### 1.1 Background

Material science is one of the oldest disciplines throughout the entire human history. Since ancient times people started to make use of available natural materials including plant leaves to make “clothes”, bones or stones to make tools, etc., although they knew nothing about the science behind at that time. Whenever new materials were invented, it was always accompanied by a huge change in many aspects of human life. That is also the reason why stone, bronze, iron and steel were chosen to name the various ages of human history. Taking our modern life as an example, it would be very difficult to imagine living in a world without steel and concrete. Also plastics, which were invented only about two hundred years ago, are now omnipresent and in use for making anything from containers to clothes, from paper clips to spaceships. It can be said that the development of our civilization is to a great extent driven by the development of materials.

In the meantime, we have entered the era of nanomaterials. Nanomaterials research belongs to a new subset of materials science, which was introduced recently and accompanied by the developments in nanotechnology. It refers to those materials for which at least one dimension has sizes between 1 nm and 1000 nm, or sometimes 1 nm to 100 nm (the common definition of nanscale)<sup>1,2</sup>. Comparing to their bulk counterparts with the same composition, nanoscaled materials have a high surface area, different surface morphology and electronic states, which frequently lead to unusual physicochemical properties, sometimes very promising for practical applications. Meanwhile, various nanomaterials with different structures from 0D nanoparticles to 3D nanoclusters, are synthesized and broadly investigated<sup>3</sup>.

In this context, nanomaterials became a strongly populated field in materials science. Functionalized nanomaterials are already present in various fields, ranging from energy to medicine, from optics to electronics, from catalysis to sensing, and

many more to be explored<sup>3-7</sup>. Atomic Layer Deposition (ALD) is among the promising technologies for future nanomaterials synthesis and functionalization due to its extreme growth control and special working manner<sup>8</sup>, which bring about great opportunities for further developments.

## 1.2 Atomic Layer Deposition

### History of ALD

The initial experiments on Atomic layer deposition (ALD) were performed by Finnish<sup>9</sup> and Russian groups<sup>10</sup> independently back in the 1960s-1970s. In its early stage, ALD was applied to deposit several materials including ZnS, SnO<sub>2</sub>, GaP, Ta<sub>2</sub>O<sub>5</sub> or Al<sub>2</sub>O<sub>3</sub><sup>9,11</sup>. Initially, it was named Atomic Layer Epitaxy (ALE) (the Russian group called it molecular layering). Scientists soon realized that most grown films were not epitaxial to the substrates, in fact most of the fabricated thin films were amorphous. Therefore, the terminology Atomic Layer Deposition (ALD) was adopted instead.

ALD was first industrially applied for manufacturing thin film electroluminescent displays<sup>9</sup>. Later in the 1990s due to the need of scaling down semiconductor devices, ALD attracted great interest in microelectronic device fabrication for the inherent advantage of depositing high-quality ultra-thin films<sup>12-15</sup>. For example, ALD is meanwhile unavoidable for depositing high-k dielectric films such as Al<sub>2</sub>O<sub>3</sub>, HfO<sub>2</sub> and many others for transistors or capacitors in memory devices<sup>16,17</sup>. It also shows great promise for electrode fabrication through deposition of conductive materials like ruthenium oxides<sup>18-20</sup>. More than that, ALD is also applied in photovoltaics<sup>21</sup> or photocatalyst<sup>22</sup> fabrication, where a functional thin film layer is needed as the photosensitive layer<sup>23-26</sup>, passivation layer<sup>27-29</sup> and sometimes encapsulation material<sup>30-33</sup>.

With the boom in nanoscience, ALD has now evolved beyond a thin film deposition technology into a powerful technique for the synthesis many kinds of nanomaterials ranging from oxides, nitrides, sulphides, to noble metals and many others including various complex materials<sup>8</sup>. For example, ALD has been used to deposit nanoparticles of noble metals such as Pt or Pd onto Al<sub>2</sub>O<sub>3</sub> supports, which showed excellent catalytic activities<sup>34,35</sup>. Nanotubes like TiO<sub>2</sub> have been synthesised by low temperature ALD processes inside tobacco mosaic viruses (TMV)<sup>36</sup>. Or

templates like anodic aluminum oxide (AAO) have been used to fabricate nanotube arrays through ALD.<sup>37,38</sup> More complicated nanostructures like inverse opal crystals has been synthesized by choosing proper templates<sup>39-42</sup>. Wrapping of different structured nanomaterials, like nanoparticles with a thin oxides shell by ALD were also demonstrated, and showed great potential for the use in photocatalysis or in ion batteries<sup>43-47</sup>.

## Fundamentals of ALD

As a thin film technology, ALD is a conceptual evolution of chemical vapor deposition (CVD). In CVD, two or more precursors are simultaneously introduced into a chamber or a reactor. This causes a chemical reaction between precursors and a simultaneous film growth. In ALD, the chemistry is confined to a substrate reaction by temporally separating the precursors, and enforcing two half-gas/solid reactions. With this separation, only one gaseous precursor is introduced into the reactor and reacts with the substrate surface at a time. Upon saturation, the excess precursors and by-products are purged and pumped away. This assures that a maximum of one monolayer of precursor is bound to the substrate and can react with the second precursor, which is handled individually, too. Repeating this procedure results in a constant growth rate and an accurate total thickness control depending on the applied cycles.

In Figure 1.1, the ALD process is schematically illustrated on the example of aluminum oxide ( $\text{Al}_2\text{O}_3$ ) deposition using trimethylaluminum (TMA) and water. In the first step, TMA is pulsed and delivered to the substrate by a high purity carrier gas (normally  $\text{N}_2$  or Ar). It binds to the hydroxyl group  $\ast\text{OH}$  ( $\ast$  represents the surface) on the substrate to form  $\ast\text{Al}(\text{CH}_3)_2$  and the volatile by-product  $\text{CH}_4$  (step 1 in Figure 1.1). When the surface is saturated with  $\ast\text{Al}(\text{CH}_3)_2$ , excess TMA and the by-product  $\text{CH}_4$  are purged with the carrier gas and pumped away (step 2 in Figure 1.1). In the next step,  $\text{H}_2\text{O}$  as counter precursor is pulsed into the reactor, which hydrolyzes the  $\ast\text{Al}(\text{CH}_3)_2$  and forms  $\ast\text{Al}-\text{OH}$  (step 3 in Figure 1.1). In step 4, the excess  $\text{H}_2\text{O}$  and the by-product  $\text{CH}_4$  are purged and pumped again, defining one cycle of the process. Thus, with one cycle up to one monolayer of  $\text{Al}_2\text{O}_3$  is grown on the substrate. By repeating this cycle, an  $\text{Al}_2\text{O}_3$  thin film will be grown, of which the thickness is a function of the applied number of cycles.

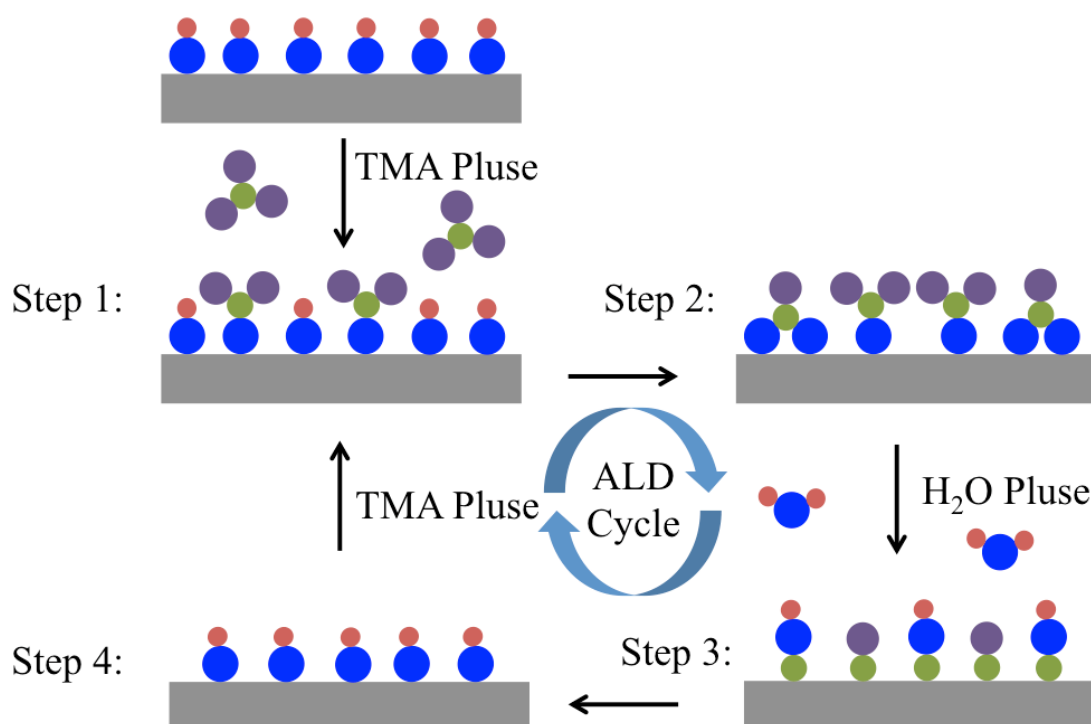


Figure 1.1 Schematic of the ALD deposition of Al<sub>2</sub>O<sub>3</sub> using trimethylaluminum (TMA) and H<sub>2</sub>O.

In each half cycle, three time-parameters, pulse time, exposure time and purging time, are important for the process. Pulse time, meaning the duration of pulsing the precursor into the reactor, controls the amount of the precursor supplied. Too short pulse times often cause under-saturation, and too long pulse times waste the precursor. Exposure times define the duration of exposure of the substrate to the precursor. Too short exposure times limit the chemisorption of the precursor, while too long exposure times extend the process duration or sometimes even trap in highly porous substrate. Purging time defines the time needed for complete removal of the excess precursors and byproducts by purging and pumping. Too short purging times leave excess precursor in the reactor and cause a CVD type of growth when the second precursor is supplied. An optimal ALD process requires proper control of these three parameters.

The process temperature also plays an important role and can seriously affect the ALD processes. As can be seen in Figure 1.2, the growth rate depends strongly on the deposition temperature. In the low temperature range, the precursor may condense on the substrate physically rather than chemically, leading to a CVD like growth mechanism; or the surface reaction may not happen in case of insufficient thermal

energy. While at too high temperatures, the precursor might decompose and result in an enhanced growth rate; or the thermal energy may be too high causing desorption of the precursor off the substrate. Thus, a steady ALD process only occurs within a material-specific temperature window.

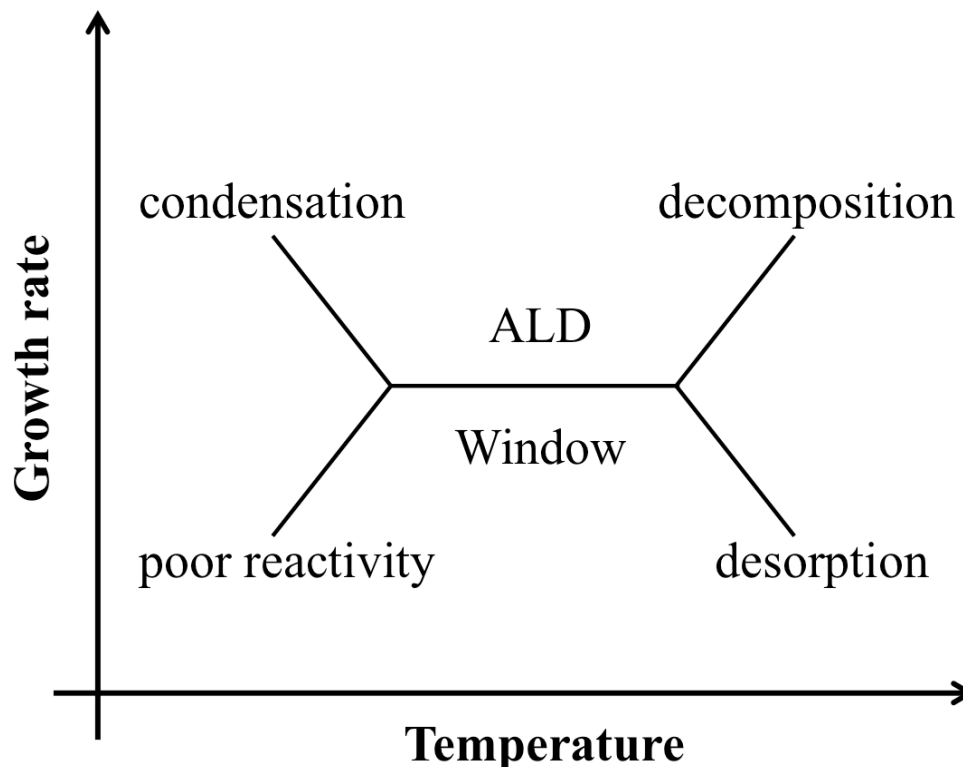


Figure 1.2 Temperature dependence of the ALD growth rate

## Working modes of ALD

Since ALD relies on chemical interactions between a gaseous precursor and functional groups on the surface, it can also be modified to use a single precursor for infiltrating a soft substrate such as a polymer and react with it. Therefore, although ALD is by design a thin film deposition method, there are two different working modes: material deposition and vapor phase infiltration (VPI).

The deposition mode works the way as described before and in Figure 1.1. It involves two different types of materials that may be grown. One type includes inorganic materials such as oxides, nitrides, sulphides and so on<sup>8</sup>. A more recent modified ALD process was developed to deposit polymers or organic-inorganic hybrid materials<sup>48-50</sup>. This process is called Molecular Layer Deposition (MLD), as organic molecules are involved. MLD has been successfully applied to deposit various polymers like such as polyamides, polyimides and so on<sup>51-54</sup>. Organic-

inorganic hybrid materials grown by MLD including zincones<sup>55-59</sup>, alucones<sup>60-62</sup> and titanicones<sup>63-65</sup>, attract great interest for their mechanical, electrical and optical properties, which are often very different from the properties of their oxide counterparts<sup>63,64,66-68</sup>. MLD has also been shown as an effective doping method. Nanoporous nitrogen-doped TiO<sub>2</sub> has been fabricated via MLD and a subsequent annealing process, showing excellent photocatalytic activity in the visible<sup>69</sup>.

Vapor phase infiltration is another working mode of ALD. Here, the gas phase precursor is allowed to infiltrate and react with the bulk of soft materials<sup>70,71</sup>. In this mode, the exposure time of the precursor to the substrate is largely extended, which enables diffusion of the precursor into subsurface areas of the soft substrate and binding to the functional groups as illustrated in Figure 1.3. The infiltration method was successfully applied for tuning the mechanical properties of biopolymers such as spider silk, egg collagen and so on<sup>72-75</sup>. The fracture toughness of spider silk was greatly enhanced after a diethyl zinc (DEZ)/water infiltration<sup>72</sup>. Synthetic polymers have also been studied in a similar way. Polytetrafluoroethylene (PTFE), which is considered to be among the most inert polymers, shows obvious changes after an infiltration with DEZ<sup>76</sup>. These results show that functionalization of polymers through this technique (vapor phase infiltration) is a very promising way for material development. However, the detailed interactions between the polymers and the ALD precursors are still under investigation.

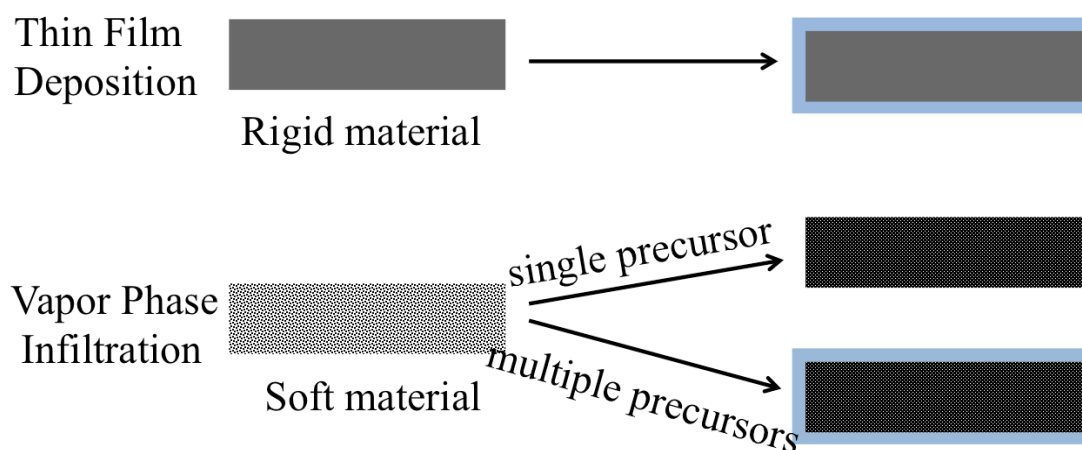


Figure 1.3 Schematic differences of a regular ALD thin film deposition and a vapor phase infiltration applying single or multiple precursors.

## Advantages of ALD

ALD has great advantages over other coating technologies like CVD, PVD (physical vapor deposition) or sol-gel methods, owing to its special working mechanism. Thanks to the self-limiting feature, one layer of a precursor is chemisorbed on the surface during each half cycle and a maximum of one monolayer is grown in each cycle. This assures the deposited film being smooth and uniform in thickness. Also the growth rate in an ALD process is constant, resulting the final thickness with extreme control to the Ångstrom level. Since ALD is based on gas/solid reactions, the gaseous precursor will diffuse and chemisorb on the entire accessible surface, leading to excellent step coverage. In contrast, CVD or PVD, if applied to samples with complex surfaces, will coat only the surfaces in the line-of-sight. With sol-gel strategies, all surfaces can be coated but sometimes small pores or cavities can not be easily reached due to aggregation of precursors, leading to non-uniform coatings<sup>8</sup>.

## 1.3 Objective and Structure of the Thesis

On the one hand, this thesis aims at studying the functionalization processes enabled by ALD, and exploring the potential uses of the resulting functionalized materials. On the other hand, the fundamental aspects regarding interaction mechanisms between precursors and substrates are investigated, which will be helpful for understanding and optimizing coating or infiltration processes in future.

Chapter 2 gives an overview over the experimental aspects performed in this research. All the characterization tools and equipment involved in this thesis are briefly introduced.

Chapter 3 focuses on the research of template-assisted nanostructure synthesis by ALD. Using various templates, synthesis of ZnO-based 0D nanodots, 1D nanotubes and 2D nanosheets were performed using ALD.

Chapter 4 describes the functionalization of graphene defects (structural defects and functional groups). ALD was applied to deposit ruthenium oxide (RuO<sub>2</sub>) nanoparticles onto graphene defects. The electrochemical capacitive performances of graphene before and after the ALD functionalization were studied.

Chapter 5 presents the growth of cobalt oxide ( $\text{Co}_3\text{O}_4$ ) nanoparticles onto carbon nanotubes (CNTs) by ALD. The electrochemical catalytic activity of the composite for the oxygen reduction reaction (ORR) was investigated.

Chapter 6 focuses on fundamental aspects of the interaction mechanism between sequential organic and metal precursors in ALD. The interactions between TMA and various organic functional groups including  $-\text{OH}$ ,  $-\text{NH}_2$  and  $-\text{NO}_2$  were explored experimentally and theoretically.

Finally, a summary of the work and future perspectives are given in Chapter 7.

---

## Chapter 2

# Experimental Techniques and Methods

This chapter summarizes the details of the used experimental techniques and methods. The characterization methods mainly relate to structural and compositional characterization, or electrochemical characterization, which were routinely applied throughout the whole thesis. Methods or techniques specific to an individual task will be discussed in the relevant sections and chapters.

## 2.1 Electron Microscopy

The electron microscope is one of the most important tools for analyzing the structure and composition of nanomaterials. Since the resolution of an optical microscope is limited to around 200 nm depending on the wavelength of visible light, such a microscope is certainly not useful for most characterizations in nanoscience and nanotechnology. The wavelength of an electron can be up to 100,000 times shorter than that of visible light, which makes the accelerated electron beam an excellent alternative illumination sources. An electron microscope can span magnifications ranging from thousands to millions with resolutions ranging from nanometers to Ångstroms. Figure 2.1 schematically shows the interactions between the accelerated electron beam and matter (sample). With respect to the way of collecting electrons by the detector, electron microscopy can be referred to as scanning electron microscopy (SEM) and transmission electron microscopy (TEM).

**Scanning electron microscopy (SEM)** is one of the most common tools used in nanoscience for inspecting the microstructure including shape, topography and morphology. In SEM, the electron beam scans across the sample surface and the detector collects the secondary electrons or backscattered electrons emitted from the sample surface resulting from excitation by the electron beam. Secondary electrons refer to the electrons ejected from sample surface by inelastic scattering interaction with the incident electrons, and depend on the sample topography. Thus, it is more commonly used in SEM.

In all experiment performed in this thesis, a Quanta<sup>TM</sup> 250 FEG (FEI) SEM was used. The accelerating voltage ranged from 1 kV to 30 kV, and the chamber pressure ranged from standard high vacuum ( $< 6 \times 10^{-4}$  Pa) to low vacuum (10 - 2600 Pa). The samples were prepared as thin films, or as powders initially dispersed in a solution and then drop-casted onto a silicon substrate.

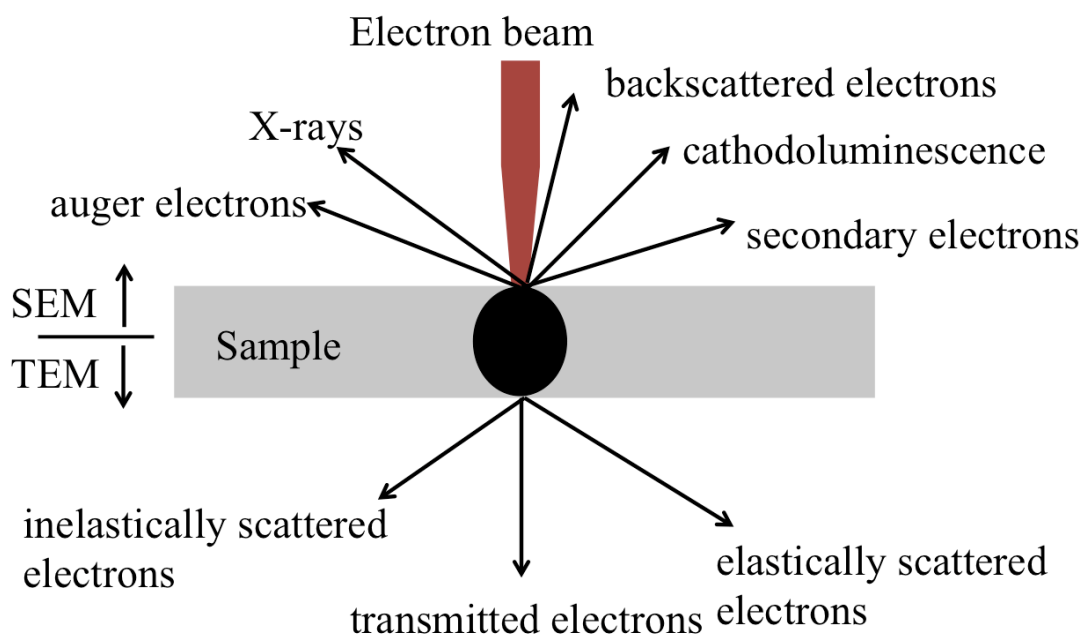


Figure 2.1 Schematic interactions between an accelerated electron beam and matter (sample) in an electron microscope.

**Transmission Electron Microscopy (TEM)** enables collecting information from transmitted electrons, and can operate at very high magnifications up to million fold. This is about an order of magnitude better than that in a typical SEM. Under TEM, crystalline lattices of materials, sometimes even single atoms, can be observed provided good alignment of the instrument.

In all experiments performed in this thesis, a Helios NanoLab Dual Beam (FEI, NL) was used to examine samples in scanning transmission mode. In addition, a high resolution TEM (FEI, Titan G2 60-300) was used to obtain detailed information of the samples. Both STEM and TEM can operate with a bright field (BF) and an annular dark field (ADF) detector. Samples were prepared by dispersion in a solution and drop casting onto a TEM grid.

Both the TEM and SEM microscopes are equipped with an Energy-dispersive X-ray spectroscopy (EDX) detector, which is used for the elemental analysis or chemical characterization.

## 2.2 X-ray Diffractometer

An X-ray diffractometer is a powerful tool to characterize the crystallinity of samples, but also the thickness of thin films. In an X-ray diffractometer, a monochromatic X-ray beam irradiates the sample at a grazing incident angle  $\theta$ , while at an angle  $2\theta$  with respect to the incident beam, a detector collects the reflected beam. When at a specific angle, the Bragg's equation

$$2d\sin\theta = n\lambda$$

is fulfilled, diffraction occurs (here is the spacing between diffracting planes, is the incident angle, is any integer, and is the wavelength of the beam, Figure 2.2 (a)). Crystalline information of the sample can be extracted from the characteristic peaks in the collected X-ray diffraction (XRD) spectrum.

The X-ray reflectivity (XRR) method can be used to analyze the thickness of a thin film. According to the Snell Law, the refractive index of all materials is below the unity for X-ray electromagnetic radiation. Thus, there exists a critical incident angle  $\theta_c$ , which depends on the material density. For an incident angle  $\theta$  equal to  $\theta_c$ , the incident X-rays will propagate along the sample surface; below  $\theta_c$  all incident X-rays will be reflected. For an incident angle  $\theta$  above  $\theta_c$ , the X-rays will partly penetrate into the material by refraction, thus the reflection will occur at both the bottom and top interfaces of the thin film. These two reflected waves will interfere with each other with an intensity decaying as a function of the incident angle. The decay shows interference fringes (also called Kiessig fringes), from which the thickness of the thin film can be obtained according to the Snell Law:

$$\frac{\sin(90 - \theta)}{\sin(90 - \theta')} = \frac{\lambda}{\lambda'} = \frac{n'}{n}$$

and Bragg's Law:

$$\begin{aligned} m\lambda &= 2 \frac{d}{\sin\theta'} \cdot \frac{n'}{n} - 2 \frac{d}{\sin\theta'} \cdot \cos\theta' \cdot \cos\theta \\ &= 2d\sin\theta' \cdot \frac{n'}{n} \end{aligned}$$

Therefore:

$$d = \frac{m\lambda}{2\sin\theta'} \cdot \frac{n}{n'}$$

Here  $\theta$  and  $\theta'$  are the incident angle and refraction angle with respect to the sample surface;  $\lambda$  and  $\lambda'$  are the incident wavelength and refraction wavelength,  $n$  and  $n'$  are the refraction index of air and the thin film;  $d$  is the thickness of the thin film; and  $m$  is the interference order.

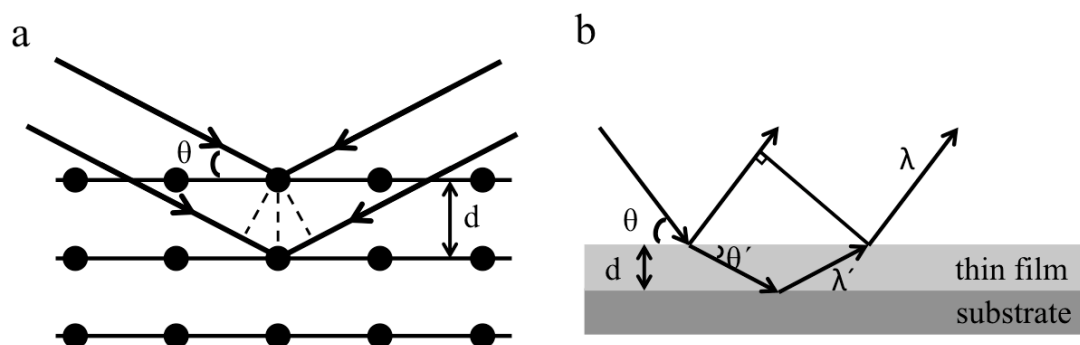


Figure 2.2 Schematics for (a) X-ray diffraction (XRD): the X-ray beam irradiates a crystal at a grazing incident angle  $\theta$  and is scattered by the atoms in the crystal. When the Bragg's equation is conditioned, characteristic peaks resulting from diffraction appears in the collected spectrum. (b) X-ray reflectivity (XRR): the X-ray beam irradiates a thin film, part of the beam reflects on the top interface of the thin film, part of the beam penetrates into the thin film and reflects at the bottom interface of the thin film and become refracted in air. Two reflected beams interfere with each other. After applying the Snell Law and the Bragg's equation, the thickness of the thin film can be obtained.

In this work, XRD and XRR measurements were performed in an X-ray diffractometer (X'Pert, PANalytical) with a Cu  $K\alpha$  ( $\lambda=0.154$  nm) radiation source. The working voltage and current for the X-ray tube were 45 kV and 40 mA, respectively. Both powders and thin film samples can be measured with different setups. All collected spectra were compared with the standard JCPDS (joint committee on powder diffraction standards) database. In the XRR measurements, the thickness of the thin films can be extracted by fitting the spectra using the Panalytical X'Pert Reflectivity software. The growth rates for different ALD processes were calculated based on the thickness measured by the XRR method.

## 2.3 Atomic Force Microscopy

Atomic force Microscopy (AFM) is a common tool to analyze the surface structure and morphology of nanomaterials. The AFM uses the interaction between the sample and a sharp tip. A cantilever, to which the tip is attached, is deflected during measuring due to the attractive and repulsive forces between the tip and the sample surface. Focusing a laser onto the cantilever and recording the movement of the reflected laser when scanning the sample, allows for imaging the morphology.

Tapping mode is the most frequently used AFM mode when operating in ambient conditions. In tapping mode, the cantilever oscillates up and down near its resonance frequency at a constant amplitude. When the tip comes close to the surface, the interaction between the tip and sample surface causes the oscillation amplitude of the cantilever to change. This change of the amplitude is used as feedback to adjust the height of the cantilever above the sample with a piezo crystal. Therefore, the tip intermittently contacts with the surface, which causes very little damage to the sample. The response of the piezo crystal is recorded for imaging.

In this work, an Agilent AFM enclosed in a noise reduced cage was used. All experiments were performed in tapping mode, the scanning area ranged from  $100\ \mu\text{m} \times 100\ \mu\text{m}$  to  $1\ \mu\text{m} \times 1\ \mu\text{m}$ . Gwyddion software was used to analyze the raw data.

## 2.4 Vibrational Spectroscopy

Vibrational Spectroscopy can be performed with two techniques: Infrared Spectroscopy (IR) and Raman Spectroscopy. Both methods can provide qualitative information about chemical functional groups in a non-destructive way. By irradiating the sample with an electromagnetic wave, specific molecular vibrations in the samples can be excited when the molecule absorbs a photon with an energy of  $E = h\nu = hc(\nu/c)$ , where  $h$  is Planck's constant,  $c$  is the velocity of light and  $\nu/c$  is the wave number.

In IR, the energy of the irradiation beam is in the infrared region with wave numbers between  $10000$  and  $200\ \text{cm}^{-1}$ , but frequently a smaller width between  $4000$  and  $400\ \text{cm}^{-1}$  is used. The molecule becomes excited to a high vibrational energy state by directly absorbing the photons. The energy-specific absorption is visible as signal at the corresponding wavenumber in the recorded spectrum. Attenuated total

reflection (ATR) is a frequently used mode in IR. In ATR, an infrared beam is directed into an ATR crystal (an optical material with a high refractive index) at a certain angle. The total internal reflection, a physical phenomenon when a wave reaches the interface from the side of a material with a high refractive index to the side of a material with a low refractive index at an incident angle above the critical angle, occurs at the interface of ATR crystal and the sample, forming an evanescent wave. The evanescent waves are attenuated or altered after penetrating into and interacting with the sample. The attenuated evanescent wave is passed back to the IR beam, exits the ATR crystal and is finally collected by the detector. The recorded signal reflects to the sample fraction in near vicinity of the ATR crystal. In ATR mode, samples can be for measured directly without further preparation.

Raman Spectroscopy stands in contrast. The irradiation beam is usually in visible range. The molecule absorbs photons with frequency  $\nu_1$  and becomes excited to a high virtual energy state. Some of the molecules relax back to the initial vibrational energy state by emitting photons with the same energy at frequency  $\nu_1$ , while others relax to another vibrational energy state by emitting photons with different different frequencies  $\nu_i$ . Those photons with  $\nu_i$  frequency are recorded, and stand in relation to the molecules' vibrational frequencies.

In this work, IR measurements were performed on a Fourier Transformed Infrared (FTIR) spectrometer (FT-IT spectrometer Frontier, PerkinElmer) equipped with an ATR operational mode. All the samples are measured in powder form.

Raman spectroscopy measurements were carried out in a confocal Raman spectrometer (Alpha 300S, WITec), with a light source at a wavelength of 532 nm. The samples were placed on a glass slide. The collected data were analyzed with the WIT spectra software.

## **2.5 Ultraviolet-Visible Spectroscopy**

Ultraviolet-visible Spectroscopy (UV-Vis) is very useful for determining the different molecules, ions and nanoparticle sizes or their concentrations in solutions. In UV-Vis, the light in the ultraviolet and visible spectral range is passed through the sample. Wavelength-dependent absorption or reflection is correlated to the electronic states of the samples. From the position and intensity of the characteristic peaks, the concentration of the sample, and sometimes the species of ions or chemicals in the

solution can be extracted. The UV-Vis measurements were performed in a Nanodrop 2000C spectrophotometer (Thermo Scientific), and the data were analyzed using the Nanodrop software.

## 2.6 X-ray Photoelectron Spectroscopy

X-ray photoelectron spectroscopy (XPS) is commonly used for analyzing the element composition, chemical states and electronic states of a sample. In XPS, the sample is irradiated with an X-ray beam under ultra-high vacuum conditions (UHV). The X-ray beam penetrates into the sample and interacts with the electrons in the sample. Electrons are excited after absorbing energy from the X-ray beam. Due to photoelectric effect electrons close to the surface escape from the sample, the numbers and kinetic energies of which are recorded by the detector. The binding energy of the emitted photoelectrons are determined by the equation below:

$$E_{binding} = E_{photon} - (E_{kinetic} + \phi)$$

where  $E_{binding}$  is the binding energy of the electrons,  $E_{photon}$  is the energy of the irradiating X-ray photons,  $E_{kinetic}$  is the kinetic energy of the electrons measured by the instrument, and  $\phi$  is the work function that depends on the material and the spectrometer and is normally constant in practice. The binding energy of recorded electrons depends on their origin, which allows identifying the specific atoms, neighboring atoms and specific orbitals. Quantitative analysis can also be made through analyzing the intensity of the recorded photoelectrons. It is worth to note that XPS is a surface sensitive method, because only electrons from an area of several nanometers close to the surface can escape from the sample and be recorded.

In this work, XPS experiments were performed using a Phoibos photoelectron spectrometer equipped with an Al K $\alpha$  X-ray source as incident photon radiation. Samples were drop-dried onto silicon or gold substrates. Si 2p or Au 4f signals were used for calibration of the measured spectra. The base pressure of the UHV chamber was at  $10^{-9}$ - $10^{-10}$  mbar.

## 2.7 Electrochemistry

Electrochemistry studies the transfer of electric energy to chemical energy and vice versa. It specifically investigates the chemical reactions that take place at

electrode interfaces, which often involves electrical charge transfer between electrode and electrolyte. As mentioned in the former chapter, nanomaterials show great potential for electrochemical catalysis, electrochemical energy conversion and storage applications. This section will give a brief introduction into the theory and methods used in this thesis.

## Cyclic Voltammetry

Standard Cyclic Voltammetry (CV) tests are performed with a three-electrode setup: a working electrode, which is the object of study, a reference electrode, which has a stable and well-known electrode potential that is used as a reference for the applied potential on the working electrode, and a counter electrode that closes a complete circuit together with the working electrode and allows the generated current to flow. In CV measurements, the potential of the working electrode is ramped linearly versus time, with the ramping rate being known as scan rate. The applied potential is cyclic, meaning that when the applied potential reaches the maximum (or minimum) value it scans back to the opposite direction towards the minimum (or maximum) potential (Figure 2.3 a).

The scanned data are often plotted as generated current versus applied voltage as shown in Figure 2.4. In the forward scan (potential increasing with time), the analyte in the electrolyte is oxidized and the generated cathodic current increases with the applied potential until it reaches the peak current  $I_{pc}$ , afterwards the current decreases with the potential; while in the backward scan (potential decreasing with time), the analyte is reduced and the anodic current first increases to the peak anodic current  $I_{pa}$  and then decreases. The corresponding applied potentials  $E_{pa}$  and  $E_{pc}$  are called oxidation and reduction potential. Sometimes, more than one cathodic or anodic peak currents occur, thus more than one corresponding oxidation and reduction potentials are obtained. This indicates that more than one redox reaction happens in the electrolyte.

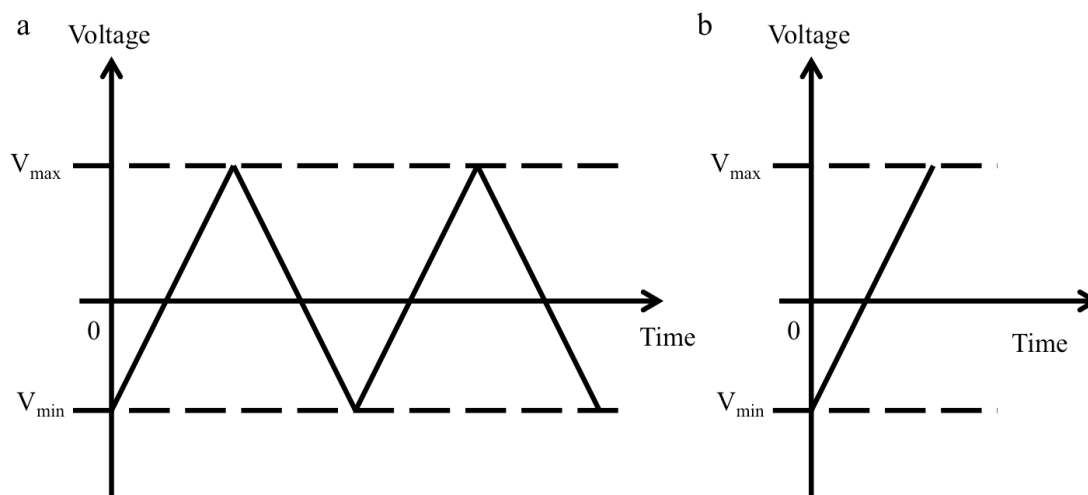


Figure 2.3 (a) Waveform in cyclic voltammetry, (b) Waveform in linear sweep voltammetry.

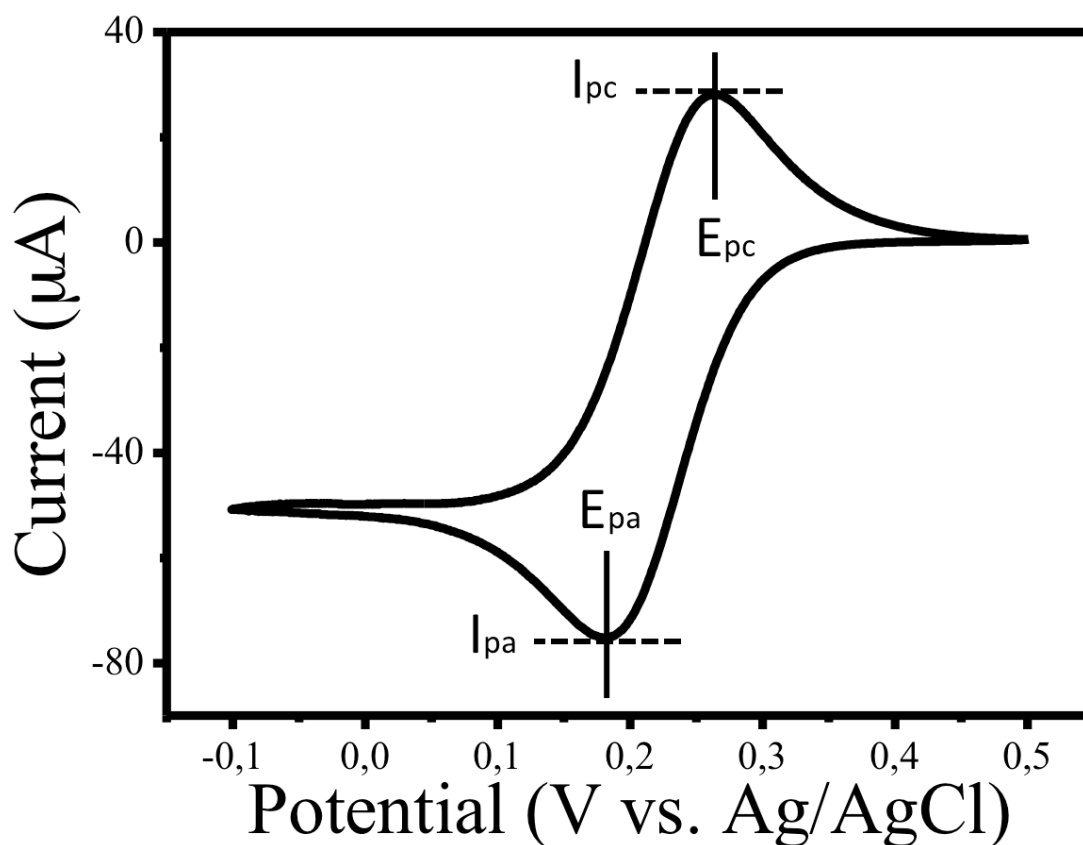


Figure 2.4 CV curve of a glassy carbon electrode in 5 mM potassium ferricyanide and 100 mM potassium chloride at a scan rate of 100 mV/s.

The CV measurement can also be applied to study the electrochemical capacitive performances of a material system with the working electrode acting as an

electrical double layer capacitor. No reduction and oxidation peaks will occur since there is no redox reaction involved but only ions adsorb to or desorb from the surface of the electrode. With the electrode acting as a pseudocapacitor, a redox reaction still happens near the surface of the electrode. In both situations, the CV method is applied in a three-electrode or two-electrode setup for characterization, which will be discussed in more detail in Chapter 4.

## Linear Sweep Voltammetry

Linear Sweep Voltammetry (LSV) is another common voltammetry method used in electrochemistry. In contrast to CV, in LSV the potential applied on the working electrode is only swept linearly versus time within a fixed range from a lower limit to an upper limit or vice versa (Figure 2.3.b). Therefore, only oxidation (or reduction) peaks will occur, giving more detailed information about the oxidation (or reduction) reaction. Especially for irreversible reactions where the analyte can be only oxidized or reduced, LSV is better suitable than CV. One example is the oxygen reduction reaction that is deeply studied in Chapter 5. In the reaction, the  $O_2$  dissolved in the solution will be the analyte, which can be only reduced, but not oxidized. The use of LSV method to study the ORR will be discussed in more details in Chapter 5.

## Rotating Disk Electrode

A rotating disk electrode (RDE) is a special hydrodynamic working electrode. In a conventional working electrode, the mass transfer in the electrolyte is controlled by diffusion since the electrolyte solution is stationary. In case of a RDE, the working electrode rotates to ensure a dynamic diffusion of the electrolyte, and attain a controlled mass transfer to the electrode depending the rotating speed. If combined with a voltammetric method such as LSV, reaction mechanisms including the electron transfer number and reaction rates of each step of the reaction can be investigated. Figure 2.5 gives an example of a setup that uses RDE and a LSV intended to study the oxygen reduction reaction catalyzed by Pt/C. This reaction will be detailed in more depth in Chapter 5.

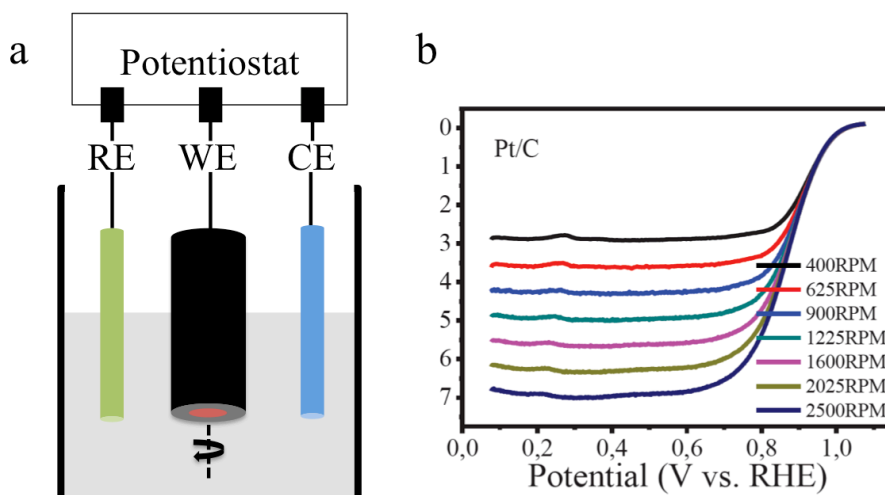


Figure 2.5 (a) Schematic of the use of a rotating disk electrode as working electrode in a three-electrode system. (b) Typical rotating-disk linear voltammetric profiles on the example of Pt/C catalyzing the oxygen reduction reaction in  $O_2$ -saturated 0.1 M KOH with a sweep rate of 10 mV/s at various rotation rates ranging from 400 rpm to 2500 rpm.

## Electrochemical Impedance Spectroscopy

Electrochemical impedance spectroscopy (EIS) is used to study the electric and dielectric properties of materials and systems. Applying a very small AC voltage at various frequencies and measuring the generated currents results in so-called Nyquist plot. It is a plot of a frequency response of the calculated impedance in the electrochemical cell, obtained by plotting the real part of calculated impedance on the X-axis and the imaginary part on the Y-axis. By matching the plot with a suitable electrical circuit composed of elements such as resistors and capacitors or many others, more detailed information about individual electrochemical processes can be obtained which is useful for determining the suitability of a material system in devices such as energy storage devices or similar.

Other methods like chronoamperometry (or chronopotentiometry), where a constant voltage (or current) is applied and the current (or voltage) is recorded as a function of time, or repeated charging-discharging tests, are also applied for specific tests in this thesis and will be introduced in more detail in the corresponding sections and chapters.

All mentioned electrochemical measurements were performed with an Autolab Electrochemical Workstation (PGSTAT 302N). The data were analyzed with the Nova 1.9 software from the workstation supplier.

---

# Chapter 3

## Nanostructures Synthesis by ALD

As introduced in chapter 1, ALD is a non-in-sight coating technology, which can be applied for uniform coating of various solid templates. Upon removal of the templates, various nanostructures resulting from the coated nanomaterials can be obtained, reflecting the used templates. This chapter shows examples of the synthesis of various ZnO-based nanostructures including 0D nanodots, 1D nanotubes and 2D nanosheets enabled by ALD.

### 3.1 Introduction

Transition metal oxides as some of the main components of nanomaterials have been broadly studied. With their unoccupied d electron orbitals, transition metal oxides often exhibit very interesting physical and chemical properties that promise great application potential in optics, electronics, sensing, catalysis, energy and so on<sup>77-81</sup>. ZnO is among the most studied transition metal oxides. Being a wide bandgap semiconductor, ZnO is a good candidate material for transistors working at harsh conditions like high voltages<sup>82</sup>, and a suitable material for making light emitting diodes or photodetectors<sup>83,84</sup>. It is found that ZnO based nanostructures show the piezoelectric effect, which has recently been used for energy harvesting<sup>85-87</sup>. Great efforts have been put into the investigations, but there are still many possibilities for further broadening the application range as well as optimization.

The structure of nanomaterials often plays an important role for the final performance of the applications or devices. Various techniques for the synthesis of various structures including 0D nanodots or nanoparticles, 1D nanowires or nanotubes, 2D nanosheets or nanoribbons and 3D nanoclusters are already mature. Those techniques include dominantly solution based and vapor based methods. Among the solution-based techniques, sol-gel methods, in which the oxides form from molecular precursors through polymerization reactions in solution, and hydrothermal methods where the reactions often take places at elevated temperatures and high pressures, are

the dominant strategies. Chemical vapor deposition (CVD) is the main vapor-based method for fabricating nanowires, nanotubes and nanosheets. Based on the working mechanism, those can be divided into two main groups, vapor-solid (VS) and vapor-liquid-solid (VLS) CVD. In vapor-liquid-solid (VLS) CVD, a catalyst is often used, which is present in its liquid phase on the substrate during the process and adsorbs the vaporized precursor until saturation. Finally a crystal grows at the liquid-solid (substrate)-interface. In vapor-solid (VS) CVD, no catalyst is used. The vapor precursor simply condenses at the colder area of the substrate.

Atomic layer deposition is based on gas/solid reactions and does not involve any catalysts. The excellent uniformity and perfect step coverage are intrinsic for ALD and optimal for nanostructure synthesis and replication. Scientists have synthesized various nanotube arrays using nanoporous anodic aluminum oxide (AAO) as templates for an ALD deposition. However, fabrication of nanoparticles and nanosheets was only rarely reported. In this work, we show that ALD can be a useful tool for the fabrication of various nanostructures. ZnO based 0D nanodots, 1D nanotubes and 2D nanosheets are synthesized by an appropriate choice of templates. This synthetic method can be easily extended to many further transition metal oxides.

## 3.2 Experiments

### ZnO nanodots

***Self-Assembled Monolayers (SAM) on Si:*** Octadecylphosphonic acid (ODPA) and 16-Phosphonohexadecanoic acid (PHDA) were purchased from Sigma-Aldrich and dissolved in isopropanol (99.99%, Sigma-Aldrich) with a concentration of 1 mM. Cut pieces (1 cm × 1 cm) of a (100) silicon wafer were first cleaned with acetone (99.99%, Sigma-Aldrich), then with ultrapure water (18.2 MΩ), dried in a high purity N<sub>2</sub> stream and finally exposed to oxygen plasma for 5 min. The samples were immersed into ODPA and PHDA mixed solutions with various ratios (1:2, 1:5 and 1:50) for 12 hours, washed with isopropanol to remove excess physically absorbed molecules and dried with N<sub>2</sub>.

***ALD depositions of ZnO:*** Diethyl zinc (DEZ) and water were used as zinc and oxygen sources. First, DEZ was pulsed for 0.015 s and purged with N<sub>2</sub> for 20 s; then water was pulsed for 0.015 s and purged with N<sub>2</sub> for 20 s. Here zero exposure time is

used for preventing the precursor getting trapped in the SAMs. The precursors were kept at room temperature. Two different chamber temperatures 120 °C and 200 °C were used. The processes were performed in a Savannah 100 (Cambridge Nanotech) ALD reactor.

## **ZnO nanotube**

***Polyvinyl Alcohol (PVA) fiber synthesis by electrospinning:*** PVA with a molecular weight of around 8000 was purchased from Sigma-Aldrich. The PVA was dissolved in hot water (90 °C) in a weight concentration of 10%. The fibers were synthesized by electrospinning method. The cooled PVA solution was loaded into a syringe equipped with a pump controlling the flow rate to 10 uL/min. A voltage of 15 kV was applied to the needle of the syringe while keeping the distance between the needle and the aluminum substrate at 30 cm. After 1 hour of electrospinning, the resulting PVA fiber mat was delaminated from the aluminum substrate and cut into small pieces.

***ALD deposition of ZnO:*** DEZ was pulsed for 0.015 s, allowed an exposure time of 30 s in the reactor and then purged with N<sub>2</sub> for 30 s. Water was pulsed for 0.015 s, allowed an exposure time of 30 s in the reactor and then purged with N<sub>2</sub> for 30 s. The precursors were kept at room temperature, while the chamber temperature was at 120 °C. The processes were performed in a Savannah 100 (Cambridge Nanotech) ALD reactor.

***Removal of the PVA fiber template:*** After the ALD process, the ZnO coated PVA fibers were soaked in hot (90 °C) water for different periods of time (30 min and 90 min), washed with water, centrifuged and collected.

## **ZnO nanosheet**

A saturated aqueous solution of NaCl was drop casted onto a cleaned glass slide and dried in air. The glass slide was placed in the ALD reactor. Two different chamber temperatures 150 °C and 80 °C were used. Al<sub>2</sub>O<sub>3</sub> was first deposited using TMA and water, with 0.015 s/ 30 s/ 30 s as pulse, exposure and purge times, respectively. Then DEZ and water was pulsed, exposed and purged with 0.015 s/ 30 s/ 30 s. After the ALD process, the samples were collected from the glass slide and

dissolved in water. The solution was centrifuged, washed several times with water, finally dried and collected.

## Characterization

AFM, SEM, STEM and XRD were performed to characterize the fabricated ZnO nanostructures. The experimental details are the same as described in chapter 2.

## 3.3 Results and Discussion

### ZnO Nanodots

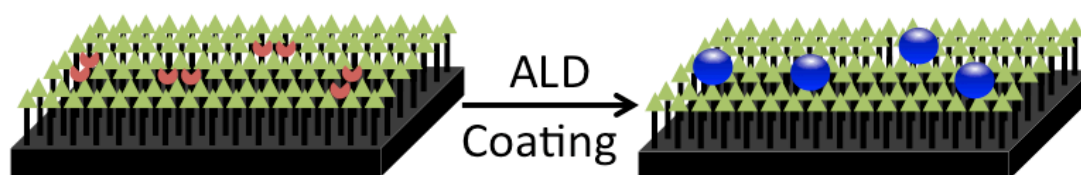


Figure 3.1. Schematic of synthesizing nanodots on SAMs by ALD.

As introduced in Chapter 1, the ALD process proceeds in a way that a gaseous precursor reacts with a solid surface and gets chemically absorbed onto it. However, if the surface terminated with a hydrophobic H-terminated functionality, no deposition will occur. Thus, by tuning the surface properties of the substrate, one can easily deposit 0D nanodots on the substrate by ALD as schematically shown in Figure 3.1. Hydrophobic and hydrophilic molecules are first self-assembled for the modification of the surface, by which hydrophilic sites are created (red crescents in Figure 3.1). During the ALD process, only these hydrophilic sites are reactive with the precursors and the process will result in dots deposition (blue dots in Figure 3.1) rather than a continuous film on the surface.

In this experiment, octadecylphosphonic acid (ODPA) and 16-phosphonohexadecanoic acid (PHDA) are selected as the hydrophobic and hydrophilic molecules (Figure 3.2). After self-assembling these two molecules onto a silicon sample, the surface is terminated with two types of functionalities:  $-\text{CH}_3$  and  $-\text{COOH}$ . During the ALD process, chemisorption of DEZ will selectively occur at the

-COOH terminals, but not the -CH<sub>3</sub> terminals for their chemical inertness. Subsequently the H<sub>2</sub>O will react with the chemisorbed DEZ only to form ZnO. After only a few cycles, ZnO nanodots can be obtained on the surface.

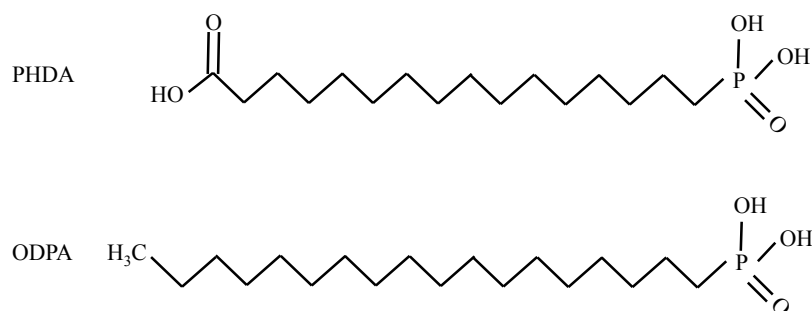


Figure 3.2 Structural formulas of 16-phosphonohexadecanoic acid (PHDA) and octadecylphosphonic acid (ODPA)

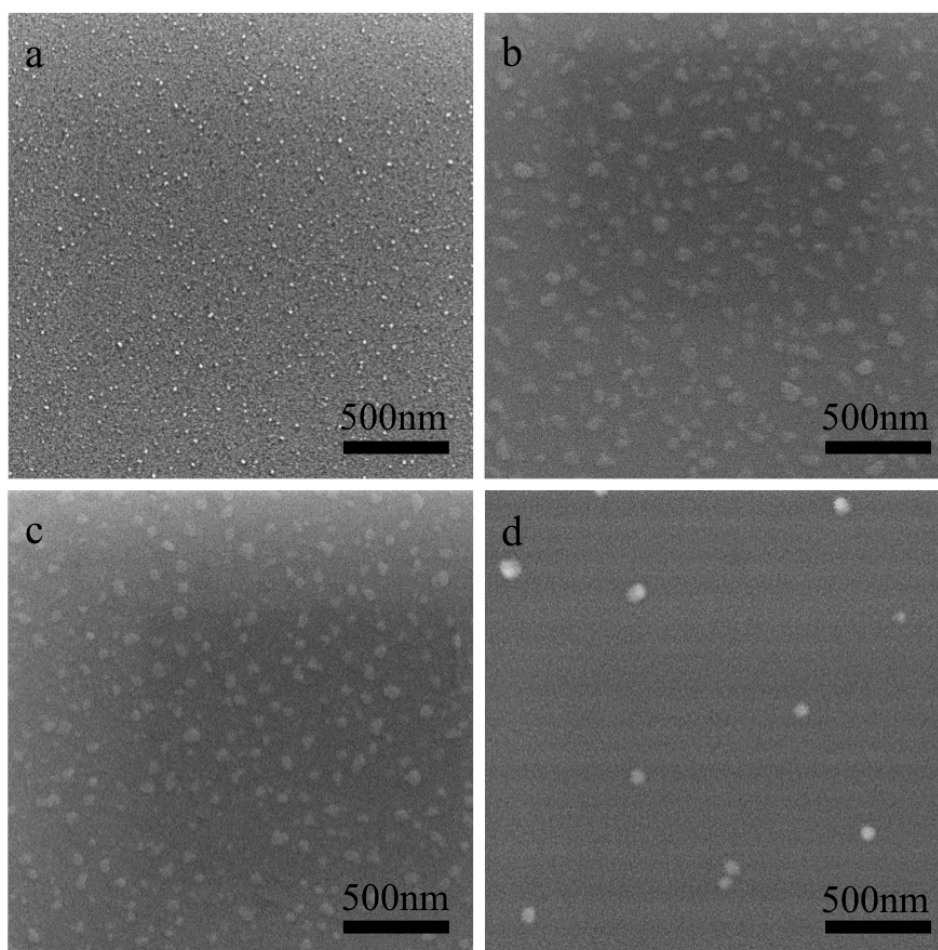


Figure 3.3 SEM image of a silicon wafer covered with SAMs and after 10 cycles of ZnO ALD, (a) at 200 °C with 1:2 of PHDA and ODPA, (b) at 120 °C with 1:2 of PHDA and ODPA, (c) at 120 °C with 1:5 of PHDA and ODPA, and (d) at 120 °C with 1:50 of PHDA and ODPA.

Figure 3.3 shows SEM images of ZnO nanodots after ALD growth. It can be seen that the temperature plays an important role for the size of the nanodots (Figure 3.3 a and b). At higher temperatures (200 °C), the ZnO resembles rather a nanoparticle structure while at lower temperatures (120 °C) nanodisk-like structures form. The reason may be that the precursor chemically binds to -COOH groups in the SAMs at only high processing temperatures, while at low temperatures physisorption of the precursor to the substrate might happen. The SAMs may also trap precursor molecules and slowly release leading to a high growth rate in the direction parallel to the surface. According to Figure 3.3 b, c and d, the sizes of the ZnO nanodots appear similar for different ratios of PHDA and ODPA. However, their density changes significantly. Figures 3.3 c and d reflect such variations in density with 1:5 and 1:50 ratios of PHDA and ODPA.

This initial experiment demonstrates that control of the surface chemistry allows area-selective ALD deposition and in this way replication of nanoparticles. Besides ALD allows identifying location and density of heterogeneously structured surfaces.

## ZnO Nanotubes

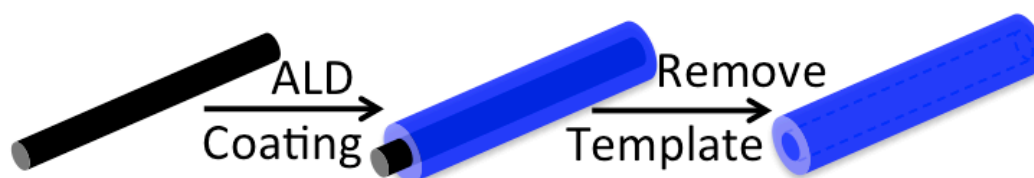


Figure 3.4. Schematic of synthesizing nanotubes by ALD.

Besides the nanodots, nanotubes can also be synthesized by ALD using appropriate templates such as nanowires or nanofibers (Figure 3.4). After ALD, a layer of materials is uniformly deposited on the templates. Upon removal of the templates, nanotubes can be obtained. In this experiment, electrospun PVA fibers are selected as templates (Figure 3.5 a). Figures 3.5 b and d show SEM images of ZnO-coated on PVA fibers. By simply soaking the PVA-ZnO sample in hot water, the PVA cores are dissolved. The resulting tubular structures of ZnO are shown in Figures 3.5 c and e. The number of deposition cycles defines the wall thickness of the

nanotubes. In Figures 3.5 c and e, samples after 80 and 100 ALD cycles indeed show a variation in their transparency for the electron beam of the SEM.

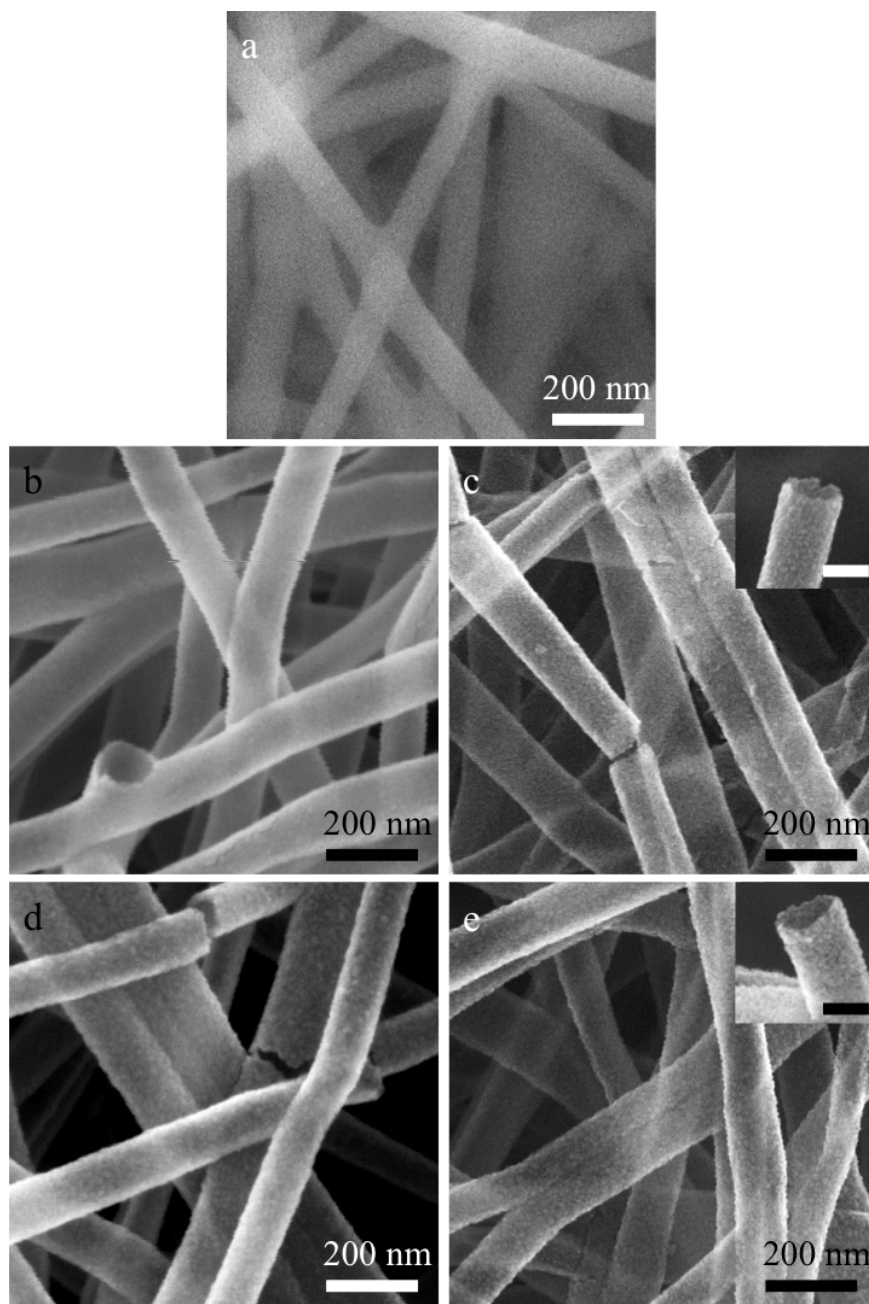


Figure 3.5 SEM images of (a) pristine PVA fibers after electrospinning, (b) PVA fibers after 80 cycles of ZnO deposition (PVA-ZnO-80), (c) PVA-ZnO-80 after removal of the PVA cores; (d) PVA fibers after 100 cycles of ZnO deposition (PVA-ZnO-100) and (e) PVA-ZnO-100 after removal of the PVA cores. Insets in (c) and (d) show higher magnifications of the synthesized ZnO nanotubes at their ends. Scale bar: 100 nm. The sample after 100 ALD cycles shows a thicker wall than that of sample after 80 ALD cycles by comparing the insets in (c) and (e).

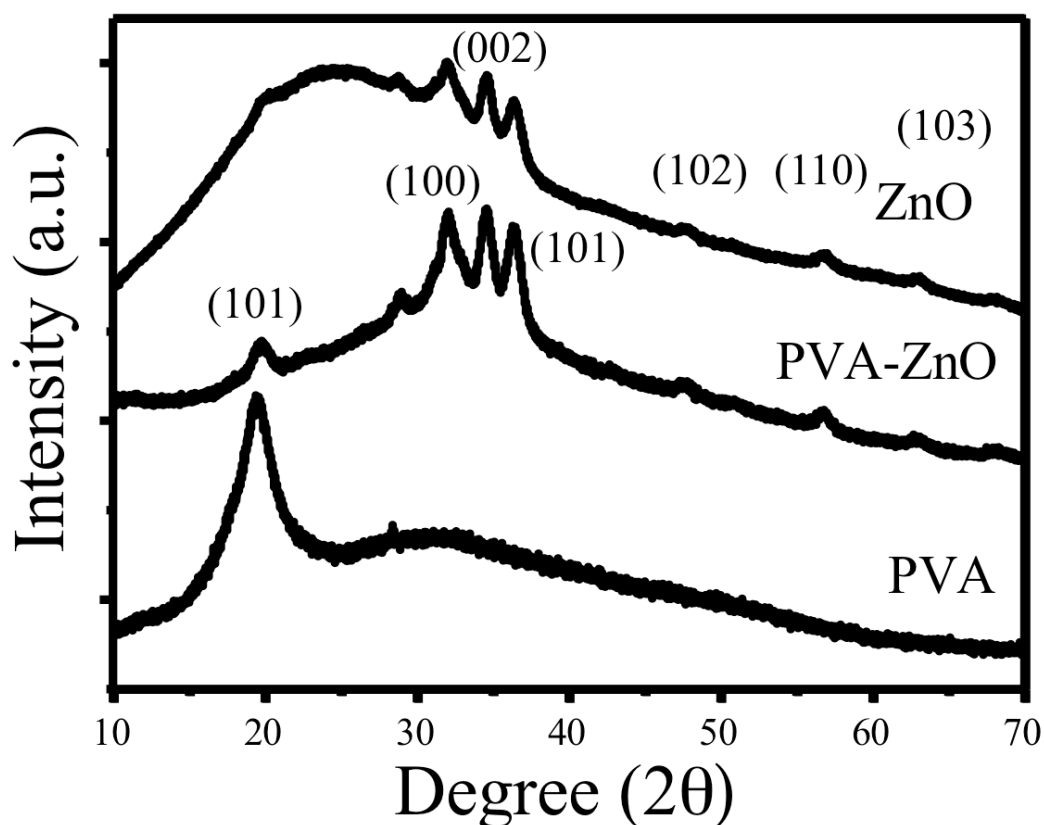


Figure 3.6 XRD spectra of (a) PVA, (b) PVA-ZnO, (c) PVA-ZnO after removal of the PVA fibers.

XRD spectra collected from PVA, PVA with ZnO coating and ZnO nanotubes are shown in Figure 3.6. Besides the (101) peak arising from PVA at around  $20^\circ$ , clear ZnO peaks at (100), (002), (101), (102) and (110) appear after the ALD coating. Interestingly, after immersing the sample into hot water for 30 minutes, the peak corresponding to PVA is still present. Thus, extended time is necessary for the complete removal of the PVA. Figure 3.7 shows how the soaking time of PVA-ZnO affects the final nanotube structure. The longer the soaking time, the more porous the nanotube will be. Possible explanations can be manifold: i) firstly during the dissolving process the water and PVA diffuse through the wall of the nanotube and might detach some of the ZnO at the grain boundaries; ii) ZnO might slowly dissolve in hot water; iii) the dissolved organic molecules might attack and etch the wall of the nanotubes. Further investigations are still needed to verify either of these speculations. However, this approach may serve as a route for the synthesis of highly porous nanotubes in further experiments.

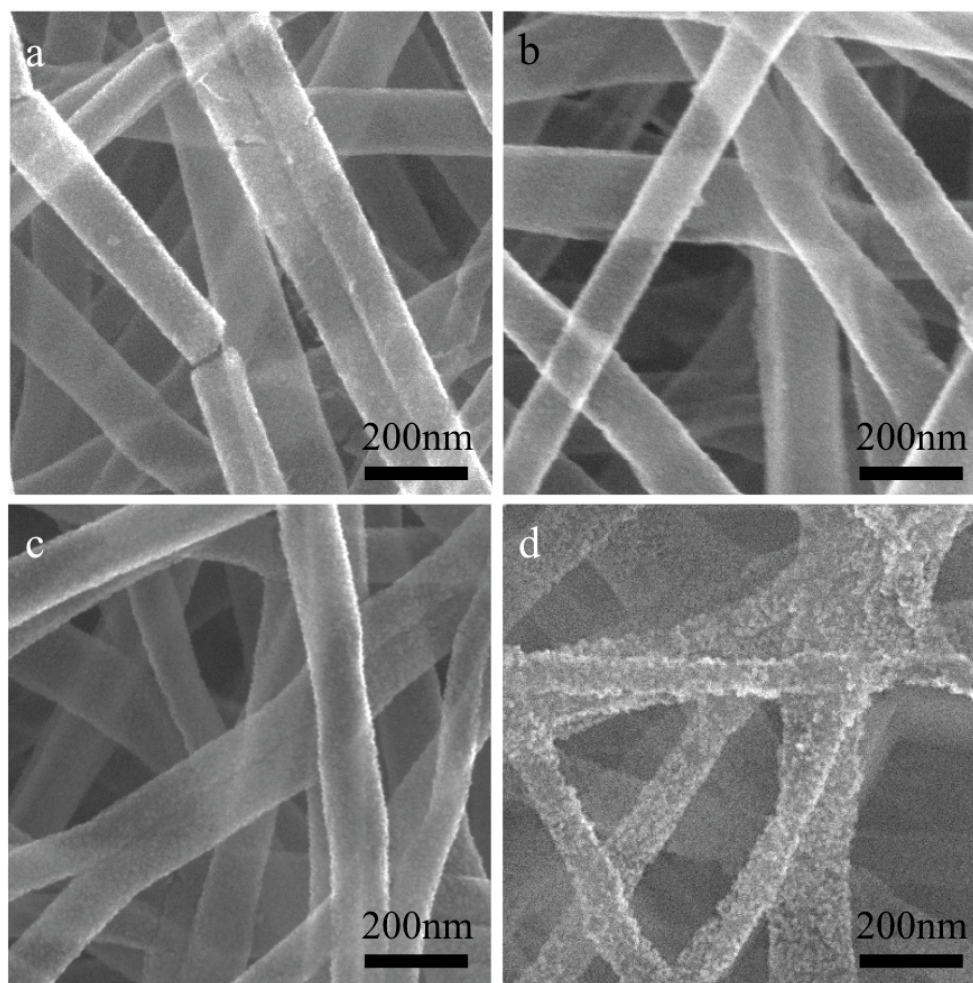


Figure 3.7 SEM images of PVA-ZnO-80 soaked in 90 °C water for (a) 30 mins, (b) 60 mins; PVA-ZnO-100 soaked in 90 °C water for (c) 30 mins, (d) 60 mins.

## ZnO Nanosheet



Figure 3.8 Schematic of synthesizing nanosheets by ALD.

The concept of synthesizing nanotubes by ALD above can also be extended for the synthesis of 2D nanosheets using a complex 3D template as schematically shown in Figure 3.8. In this experiment, recrystallized NaCl nanocubes are chosen as

templates for a  $\text{Al}_2\text{O}_3/\text{ZnO}$  hybrid nanosheet synthesis.  $\text{Al}_2\text{O}_3$  was first deposited on the NaCl nanocubes on the one hand serving as seed layer for the nucleation of ZnO, and on the other hand as a component of the hybrid material. Subsequently, ZnO is deposited. The  $\text{Al}_2\text{O}_3/\text{ZnO}$  hybrid nanosheets are obtained after the removal of NaCl as shown in Figure 3.9.

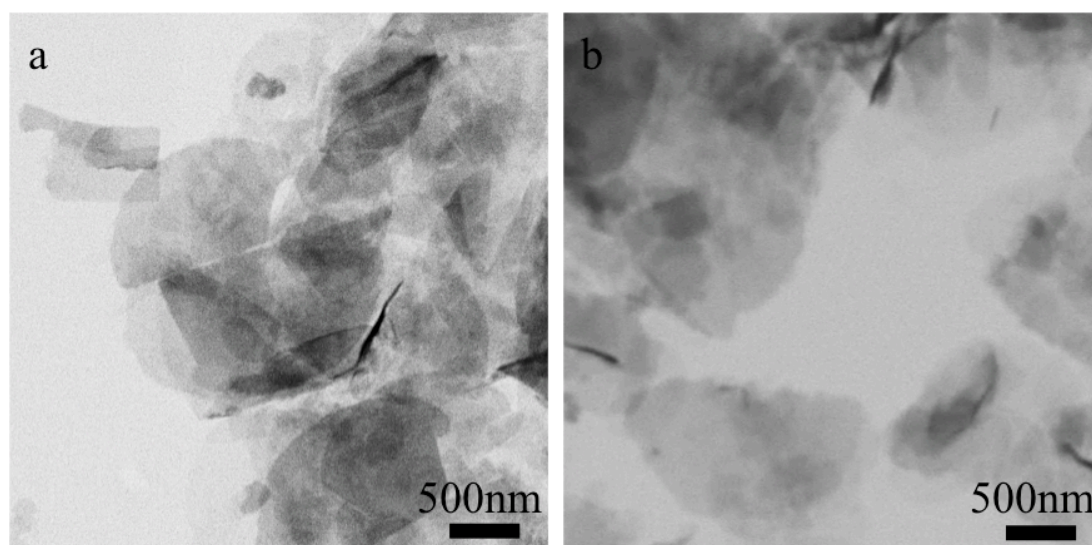


Figure 3.9 SEM images of  $\text{Al}_2\text{O}_3/\text{ZnO}$  hybrid nanosheets obtained after applying 50 cycles of  $\text{Al}_2\text{O}_3$  at  $80^\circ\text{C}$  and 25 ALD cycles of ZnO deposited at (a)  $150^\circ\text{C}$  and (b)  $80^\circ\text{C}$ .

### 3.4 Conclusions

This chapter shows a phenomenological approach towards controlled nanostructure fabrication based on templates. We showed examples of ZnO based synthesis of 0D nanodots, 1D nanotubes and 2D nanosheets through ALD. Such processing can also be extended to other metal oxide based structures as a general synthetic method. By modifying the surfaces with SAMs, nanodots or nanoparticles can be grown even area and density selective. While using a sacrificial template nanotubes or nanosheets can be synthesized.

The general route for each individual nanomaterial fabrication appears valid. Substrates or templates as well as coating materials need to be adjusted and optimized for a specific problem that requires a solution. Based on the procedures, a build-up of more complex fabrication strategies will be described in the following chapters.

---

# Chapter 4

## ALD Functionalization of Graphene

Based on the previously (chapter 3) elaborated strategy to grow nanoparticles of materials selectively on functional groups of a substrate, the process was adopted to a more complex system. This chapter reports on the functionalization of graphene defects including structural defects and functional groups with RuO<sub>2</sub> nanoparticles applying ALD. It shows that the chemical interaction between the RuO<sub>2</sub> nanoparticles and graphene, and the degree of functionalization by means of control over sites and density of RuO<sub>2</sub>, can be optimally exploited. The electrochemical capacitive performance and stability of the graphene are greatly enhanced after the ALD functionalization. This work on defects functionalization might pave ways for future optimized graphene based applications.

### 4.1 Introduction

#### Background

Graphene is a material with exciting physical properties and therefore of great interest for numerous applications including, but not limited to, electronics, energy storage and conversion, etc<sup>88-93</sup>. Although meanwhile vapor based synthetic processes for defect-free graphene have been established<sup>94</sup>, wet chemical procedures that yield graphene oxide (GO) in large amounts are most common<sup>95</sup>. The drawback of those materials is their large number of defects, commonly oxidized carbon, that have serious negative impact on the physical or electrochemical properties of this graphitic compound. The chemical reduction of such defects is a common procedure and yields reduced graphene oxide (rGO) that, in spite of still having defect sites, closely resembles the properties of graphene. Functionalization of the remaining defect sites with precise control may be of great benefit for any anticipated application and pave ways for novel graphene-based devices with high efficiency.

Among the applications for which graphene is considered beneficial, supercapacitors attract considerable attention. Supercapacitors are of current interest for their high power density, fast charge/discharge rate, excellent cycling stability as well as operational safety<sup>96-99</sup>. A serious amount of research and development is devoted to investigation of various types of graphene-based electrodes, including graphene only<sup>100-102</sup>, graphene-metal oxide composites<sup>103-106</sup> and so on. In a recent work, hydrous RuO<sub>2</sub> particles have been anchored to graphene sheets through sol-gel techniques and low temperature annealing, eventually resulting in a high specific capacitance of the composite<sup>105</sup>. Such heterogeneous compositions are very interesting from the scientific perspective. Namely, occasionally specific capacitances are observed that are beyond the ones expected from a theoretical sum of the constituting components. Such additive effects are believed to result from synergies between the materials and may have multiple chemical or physical origins. If one considers rGO, one major reason for deviation of the physico-chemical properties from the expected ones may lie in the intrinsic defect sites that affect both the conductivity and the capacitance of the rGO. Such defects are, however, not easy to be chemically modified in a controlled way.

As described in former chapters, ALD offers the possibility to grow nanoparticles on a variety of substrates<sup>48,107</sup>. Firstly, ALD enables covalent bonding of the precursors to functionalities of the substrate in each half reaction, allowing for intimate and stable contact of the substrate and deposit. Secondly, the self-saturating mechanism in ALD processes allows extreme control of the amount of the deposited material, even at the atomic scale, by simply controlling the number of deposition cycles. Therefore, it would be quite convenient to functionalize the defects of rGO with high accuracy by applying ALD.

In this work, we show an approach towards optimization of the electrode material based on the already mentioned system of RuO<sub>2</sub> nanomaterials in combination with rGO. The deposition of tiny amounts of RuO<sub>2</sub> on reduced graphene oxide (rGO) is performed by ALD with its loading being controlled with the number of processing cycles. The electrochemical capacitive performance and stability of graphene are greatly enhanced after the ALD functionalization compare to the non-processed graphene.

## Supercapacitors

Supercapacitors, also named as ultracapacitors, are electrochemical capacitors with much higher capacity than the conventional ones. Often two charge storage processes are involved: electrostatical storage of charges at the interface or storage of charges in the electrode subsurface through faradaic reactions.<sup>108</sup> Capacitors relying on the former process are called electric double layer capacitors and in the latter case pseudocapacitors. A supercapacitor may sometimes involve both processes. Due to their fast charging and discharging rates, high power densities and excellent stabilities upon numerous charge/discharge cycles, supercapacitors attract great interest among researchers and are considered key components in future energy systems.

## 4.2 Experiments

### rGO/RuO<sub>2</sub> electrode fabrication

The rGO/RuO<sub>2</sub> was fabricated in two steps. First, rGO sheets were electrochemically immobilized onto carbon cloth. For this purpose, carbon cloth with a thickness of about 300  $\mu\text{m}$  (12  $\text{mg}/\text{cm}^2$ ) was cut into rectangular strips (1  $\text{cm} \times 2$   $\text{cm}$ ) to be used as the substrate. Commercially available reduced graphene oxide (rGO) powder (Graphenea, Spain) was dispersed in water ( $\sim 0.1$   $\text{mg}/\text{mL}$ ) assisted with ultrasound. One slice of carbon cloth was used as the positive electrode; a gold plate was used as counter electrode. The two electrodes were vertically immersed into the rGO solution in a beaker with a 1  $\text{cm}$  distance between them. A Constant current of 0.25  $\text{mA}$  was applied for 5  $\text{h}$  to immobilize the rGO on the carbon cloth. Subsequently the carbon cloth was removed and dried in air. The weight of the electrode was measured by a microbalance before and after the immobilization. In the second stage, ruthenium oxide was deposited onto the rGO sheets by ALD (Savannah 100, Cambridge).<sup>109–113</sup> The reactor was kept at 250  $^\circ\text{C}$ , while the Ruthenium precursor Ru(EtCp)<sub>2</sub> (bis-(ethylcyclopentadienyl) ruthenium) was maintained at 75  $^\circ\text{C}$ . High purity O<sub>2</sub> (99.99%) was used as oxygen source, and high purity N<sub>2</sub> (99.99%) was used as carrier gas and purging gas. All gas lines were kept at 130  $^\circ\text{C}$  to prevent cold spots and precursor condensation. For each ALD cycle, the pulse time, exposure time and purging time of Ru(EtCp)<sub>2</sub> and O<sub>2</sub> precursors were 1 s/60 s/90 s and 3 s/60 s/90 s, respectively. The size of the RuO<sub>2</sub> particles was accurately controlled by the number

of ALD cycles and the loadings were quantified by inductively coupled plasma-mass spectrometry (ICP-MS, NexION® 300).

## Physical characterization

The morphologies and microstructures of all prepared samples were examined by scanning electron microscopy (FEI, Quanta 250 FEG) and transmission electron microscopy (FEI, Titan G2 60-300) at various magnifications. XRD examinations were performed with a powder diffractometer (X'pert, PANalytical). Raman spectroscopy was performed using a Raman microscope (Alpha 300S, WITec). XPS experiments were performed using a Phoibos photoelectron spectrometer equipped with an Al K $\alpha$  X-ray source (12 mA, 8.33 kV) as the incident photon radiation. Tantalum foil was used to create an electrical contact between the sample surface and the sample holder to avoid charging effects, also acting as calibration of the binding energy.

## Electrochemical characterization

All prepared electrodes were first tested in a three-electrode cell, where a Pt sheet served as the counter electrode, Ag/AgCl (3 M KCl) as the reference electrode and a 1 M H<sub>2</sub>SO<sub>4</sub> aqueous solution as the electrolyte. Cyclic voltammetry curves were recorded in a potential range between 0 and 1 V at various scanning rates. The galvanostatic charge/discharge processes were performed from 0 to 1 V at different current densities. Both CV tests and galvanostatic charge/discharge tests were also performed in a classical two-electrode configuration, where two rGO/RuO<sub>2</sub>-20 electrodes (or rGO electrodes) were assembled to a supercapacitor device using laboratory filter paper (Carl Roth, Germany) as separator in 1 M H<sub>2</sub>SO<sub>4</sub> aqueous solution. The cycling stabilities were characterized using cyclic voltammetry at a scanning rate of 100 mV/s for more than 4000 cycles. All electrochemical tests were carried out using an Autolab electrochemical working station (PGSTAT 302N).

## Calculation methods

For the three-electrode system, the specific capacitance of rGO/RuO<sub>2</sub>-X (X indicates the applied ALD cycles) was calculated based on galvanostatic charge/discharge tests according to the equation:

$$C_s = \frac{\int i dV}{2m\Delta V(dV/dt)}$$

The specific capacitance of RuO<sub>2</sub> only was calculated based on cyclic voltammetry tests according to the equation:

$$C_{s,RuO_2} = \frac{\int i_{rGO/RuO_2} dV - \int i_{rGO} dV}{2m_{RuO_2} \Delta V(dV/dt)}$$

Where  $\Delta V$  is the applied voltage window,  $i$  is the current and  $dV/dt$  is the scanning rate,  $m$  and  $m_{RuO_2}$  are the total weight of rGO/RuO<sub>2</sub>-X and the weight of RuO<sub>2</sub> nanoparticles only.

For the two-electrode system, the specific capacitance of rGO/RuO<sub>2</sub>-X was calculated based on galvanostatic charge/discharge tests according to the equation:

$$C_s = 2 \frac{it}{m\Delta V}$$

where  $i$  and  $t$  are the discharge current and time,  $\Delta V$  is the potential drop during discharge and  $m$  is the weight of the active materials present on one single electrode.

The energy density and power density were calculated based on the equation:

$$E = \frac{1}{4} \times \frac{1}{2} C_s \Delta V^2$$

$$P = E/t$$

The individual contributions of rGO and RuO<sub>2</sub> to the energy density were calculated based on the equation:

$$C_s = C_{s,rGO} * wt_{rGO} \% + C_{s,RuO_2} * wt_{RuO_2} \%$$

### 4.3 Results and Discussion

The anticipated functionalization of rGO is easiest shown on a practical example. Therefore, we chose the supercapacitor as demonstrator and initially fabricated the electrodes. The fabrication process contains two steps: (1) electrochemical immobilization (ECI) of rGO sheets onto carbon cloth and (2) growth of RuO<sub>2</sub> nanoparticles on the immobilized rGO by ALD (Figure 4.1 a). In the first step, a contacted carbon strip was immersed into an rGO suspension with a gold plate as counter electrode. By applying a constant current to the electrodes, the negatively charged rGO sheets were adsorbed to the surface of the carbon cloth. Figures 4.1 b and c show the surface morphology change of the carbon electrodes after the ECI

process. In Figure 4.1 c, individual carbon fibers fully covered with rGO sheets containing one or more graphene layers can be seen.

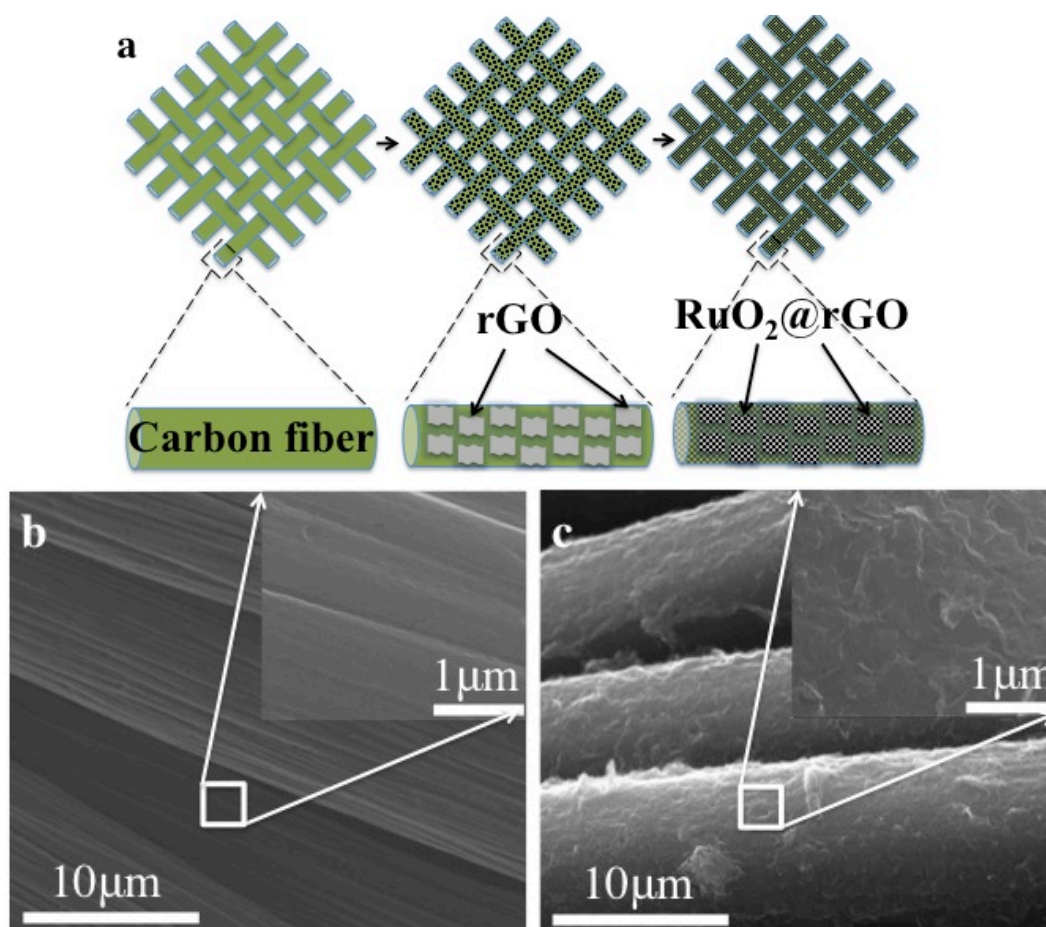


Figure 4.1 (a) Schematic of the fabrication process of the rGO/RuO<sub>2</sub> electrodes on carbon cloth. The first step involves attachment of rGO to carbon cloth by electrochemical immobilization (ECI). In the second step atomic layer deposition (ALD) is applied to deposit RuO<sub>2</sub> nanoparticles on rGO. Scanning electron microscope (SEM) images of (b) carbon fiber, and (c) carbon fiber covered with rGO (insets with higher magnification).

In the second step, the rGO was functionalized with RuO<sub>2</sub> by applying an ALD process with Ru(EtCp)<sub>2</sub> (ris-(ethylcyclopentadienyl) ruthenium) and O<sub>2</sub> as precursors<sup>109–113</sup>. Commonly one would expect the deposition of a thin RuO<sub>2</sub> film by ALD<sup>8</sup>, but given the chemical inertness of graphene, the growth of RuO<sub>2</sub> proceeded on distinct sites only. This can be attributed to the chemistry between precursor and substrate, namely the ALD precursors require a functional site for chemisorption during the first half-reaction. The functional sites are commonly defects and in the

case of oxidized graphene those may be carboxylic or alcoholic functionalities present intrinsically or induced by oxidative pretreatment with plasma or ozone<sup>114</sup>. The distribution of the defects is reflected in the distribution of the RuO<sub>2</sub> nanoparticles on rGO after the ALD process and is very uniform. With fully functional surfaces, a 2-dimensional ALD film would grow into the third dimension, i.e. the film thickness will be a function of the number of ALD cycles applied. Since the initially deposited RuO<sub>2</sub> on defect sites of the rGO act as zero-dimensional seeds, the growth proceeds in three dimensions, eventually resulting in highly controllable nanoparticle growth. The nanoparticle diameters become a function of the number of applied cycles.

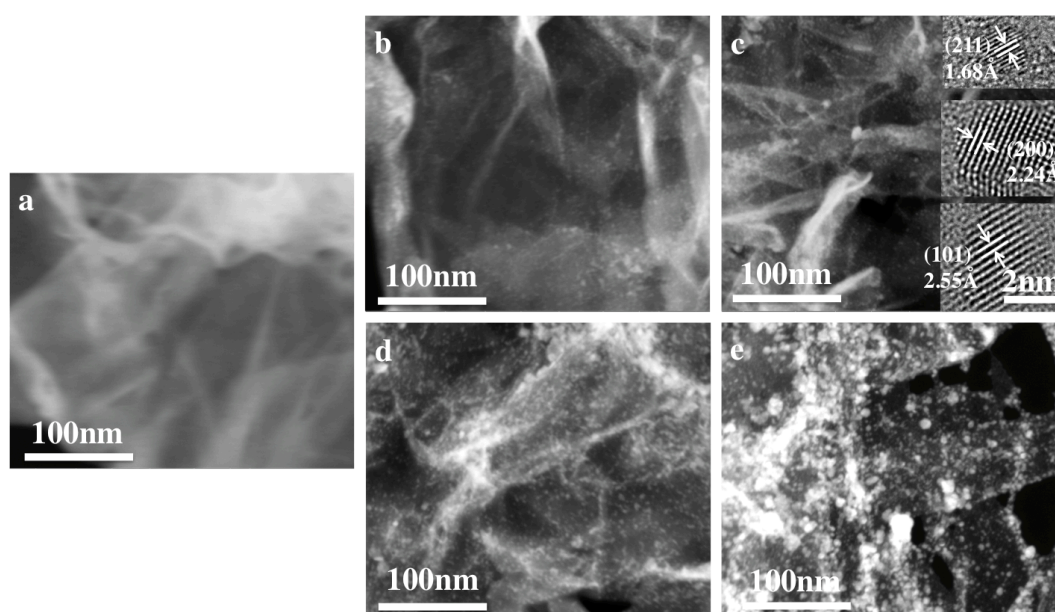


Figure 4.2. Scanning Transmission Electron Microscope (STEM) images of (a) rGO, (b) rGO/RuO<sub>2</sub>-15, (c) rGO/RuO<sub>2</sub>-20, (d) rGO/RuO<sub>2</sub>-30 and (e) rGO/RuO<sub>2</sub>-50. The inset of (c) shows HRTEM images of RuO<sub>2</sub> nanoparticles, scale bar: 2 nm.

Figure 4.2 shows STEM micrographs of rGO and rGO-X (X = 0, 15, 20, 30 or 50 applied ALD cycles) samples with randomly distributed RuO<sub>2</sub> nanoparticles that grew on rGO. Occasionally, bigger particles were observed. Those are the result of either merging of neighboring particles during growth<sup>8,115</sup>, or are optical illusions resulting from imaging through semitransparent graphene sheets in folded or overlapped regions of graphene. These seemingly bigger particles become particularly obvious with the ALD cycle numbers increasing beyond 30, especially for the 50

ALD cycles sample in Figure 4.2 e. Once the number of applied ALD cycles increases beyond 50, the nanoparticles start merging into a continuous film.

Figures 4.3 a-d show the size distribution of RuO<sub>2</sub> nanoparticles on rGO after 15 to 50 ALD cycles. The sizes of the grown particles had a very small deviation for each sample. Furthermore, the dependence of the average size of RuO<sub>2</sub> nanoparticles on the number of ALD cycles shows an almost perfect linear relationship in Figure 4.3 e. Therefore, one can tune the particle size (and resulting mass loading) by easily altering the number of ALD cycles applied. This precise control over the deposited RuO<sub>2</sub> is sine qua non for an optimal functionalization of the defect sites of rGO.

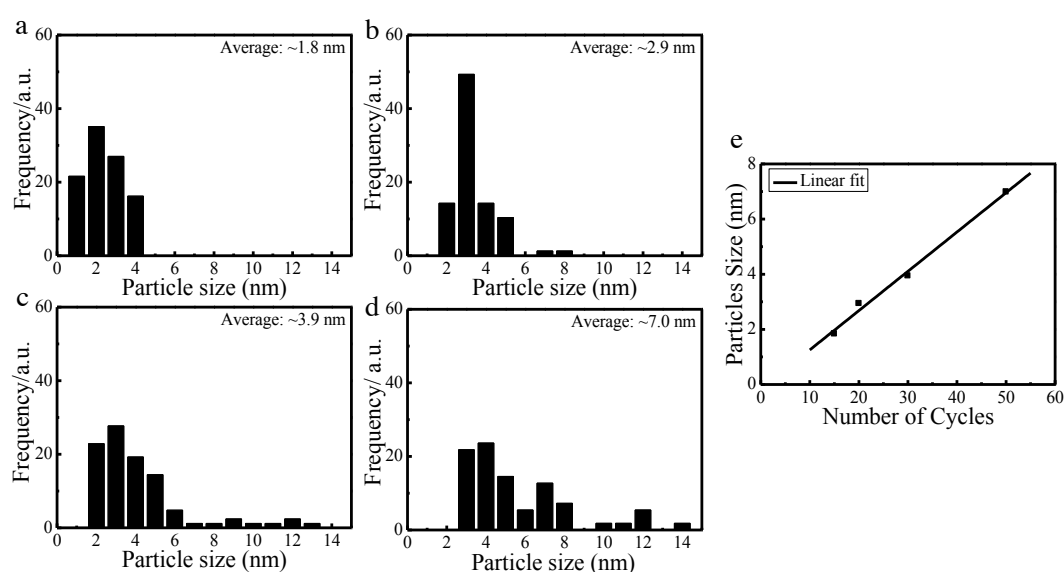


Figure 4.3 Size distributions of the RuO<sub>2</sub> nanoparticles grown on rGO after (a) 15, (b) 20, (c) 30, (d) 50 applied ALD cycles. (e) Dependence of the average size of RuO<sub>2</sub> nanoparticles on the number of applied ALD cycles.

The grown RuO<sub>2</sub> particles were characterized by high-resolution transmission electron microscopy (HRTEM). Well-defined crystalline lattices can be clearly seen in the inset of Figure 4.3 c, and lattice spacings of 2.55 Å, 2.24 Å and 1.68 Å perfectly match the (101), (200), and (211) crystallographic planes of the tetragonal RuO<sub>2</sub> (JCPDS#00-040-1290). XRD and Raman spectroscopy characterization are also performed with the functionalized samples. The XRD spectrum of RuO<sub>2</sub>-decorated rGO on carbon cloth in Figure 4.4 a shows four clear peaks at  $2\theta=28.1^\circ$ ,  $35.1^\circ$ ,  $40.6^\circ$  and  $54.3^\circ$  that correspond to the rutile (tetragonal) phase of RuO<sub>2</sub> at (110), (101), (200) and (211) orientation, respectively, according to the standard RuO<sub>2</sub> spectrum

(JCPDS#00-040-1290). Note that no peak characteristic for metallic Ru was found, thus confirming the ALD deposition of RuO<sub>2</sub> only. For comparison, X-ray diffraction was recorded both from native and ALD-processed rGO samples. Figure 4.4 b shows clear RuO<sub>2</sub> features around 520 cm<sup>-1</sup>, 680 cm<sup>-1</sup> and 708 cm<sup>-1</sup> obtained by Raman spectroscopy<sup>116,117</sup>. Note that samples of the 50 ALD cycles were used since the loading of RuO<sub>2</sub> on samples with lower numbers of ALD cycles was too low and resulted in spectra with a poor resolution and signal to noise ratio. A more precise characterization of the deposited material after fewer numbers of cycles is reserved for future studies as more sophisticated techniques need to be applied and the instrumentation for such characterizations still requires engineering until it becomes operational.

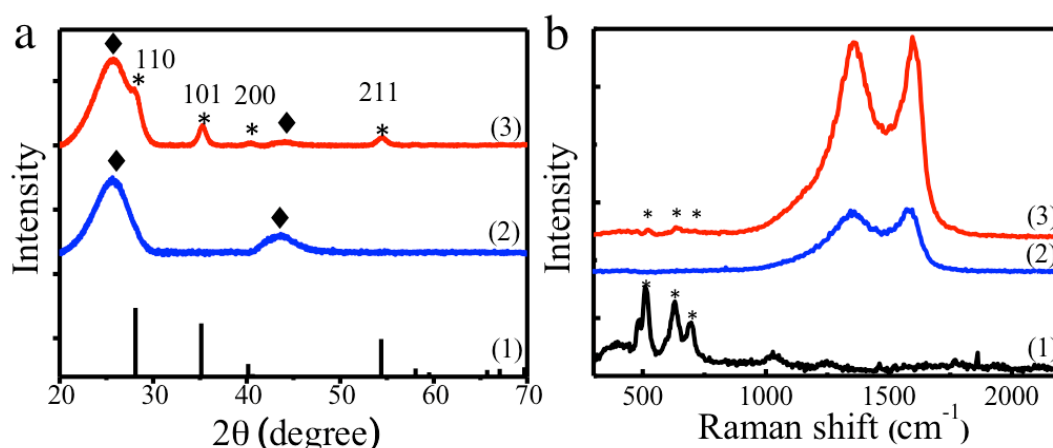


Figure 4.4 (a) XRD of (1) standard rutile RuO<sub>2</sub> (JCPDS#00-040-1290), (2) CC-rGO and (3) CC-rGO/RuO<sub>2</sub>-50, (b) Raman spectra of (1) commercial RuO<sub>2</sub> powder, (2) CC-rGO and (3) CC-rGO/RuO<sub>2</sub>-50.

XPS studies were conducted in order to understand the nature of the chemical interaction between the RuO<sub>2</sub> particles and the rGO substrate. Figure 4.5 a shows that after the RuO<sub>2</sub> growth the O 1s peak for the rGO changed significantly. In the low binding energy region I, a new peak appears that can be attributed to the RuO<sub>2</sub> nanoparticles ( $\sim 529.3$  eV)<sup>118,119</sup>, while the O signal in region II, which originates mainly from C=O ( $\sim 531.2$  eV)<sup>120-122</sup>, decreases. In the high binding energy region, the intensity of the signal also increases. In region III, the peak can be assigned to C-OH ( $533.7$  eV)<sup>120-122</sup>. However, due to the same Pauling electronegativity of H and Ru (both 2.2), the C-O-Ru peak is expected in this region as well. Thus, it can be

expected that during the ALD growth of  $\text{RuO}_2$ , some of the  $\text{C}=\text{O}$  type defects in rGO are attacked by the Ru precursor to form  $\text{C}-\text{O}-\text{Ru}$ . For the GO sample, the increase in region I and III and the decrease in region II, is even more pronounced than in the case of rGO, since the GO has a seriously higher defect density than rGO. Thus, we conclude that the ALD functionalization proceeds in a covalent way.

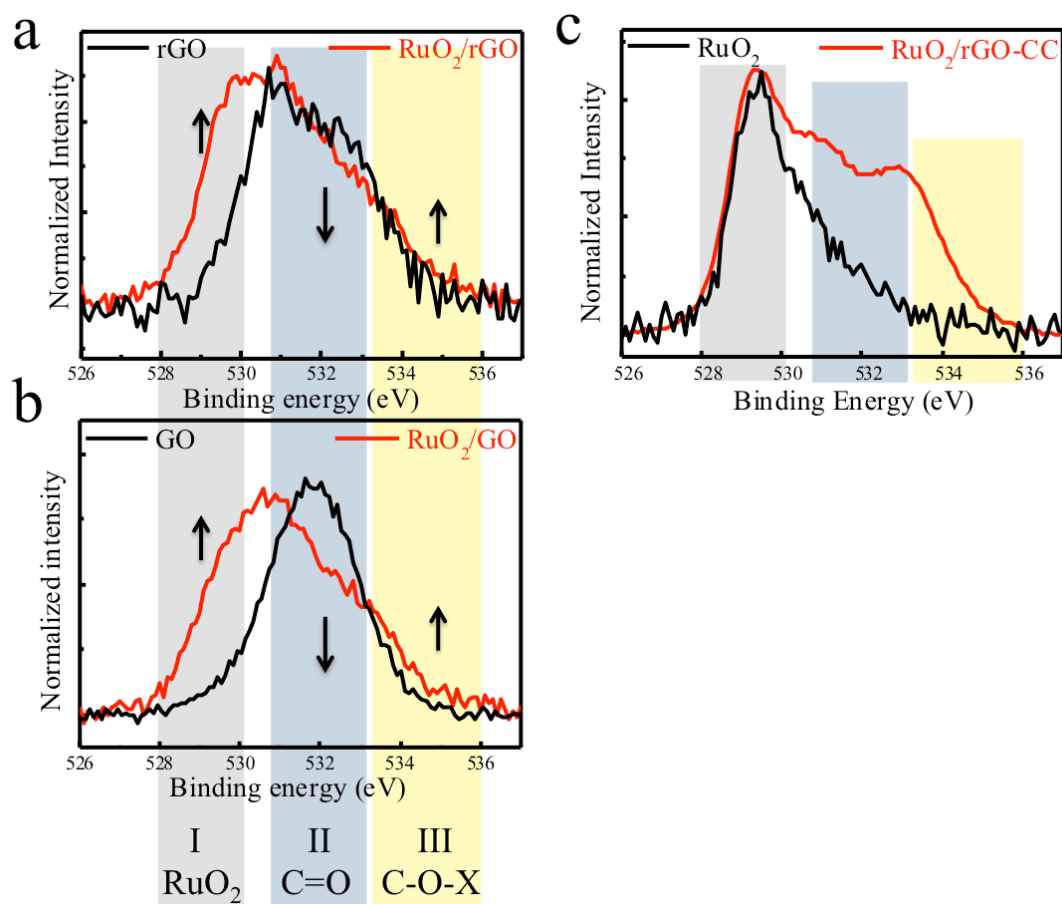


Figure 4.5 O 1s XPS spectra of (a) rGO and 40 cycles of  $\text{RuO}_2$  deposited on rGO, (b) GO and 40 cycles of  $\text{RuO}_2$  deposited GO and (c) 80 cycles  $\text{RuO}_2$  deposited on rGO immobilized on carbon cloth and  $\text{RuO}_2$  on gold covered silicon.

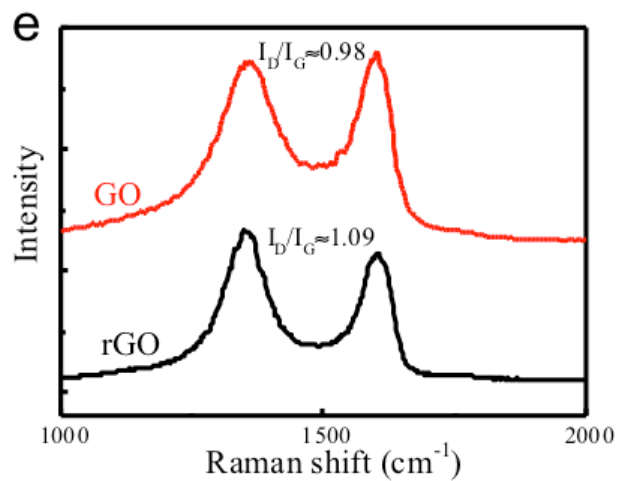
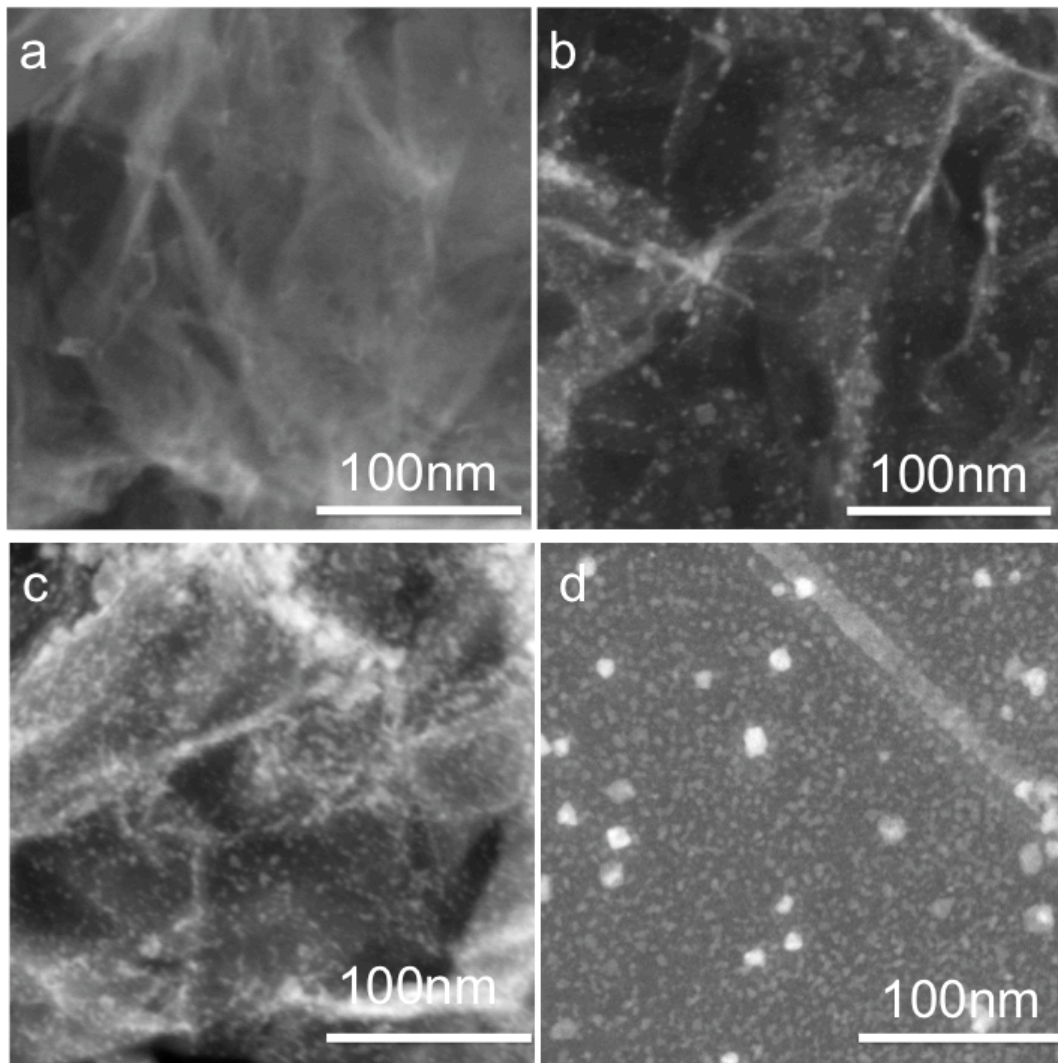


Figure 4.6 RuO<sub>2</sub> ALD functionalization (30 cycles) of (a) non-activated rGO, (b) 10 min, ozone activated rGO, (c) 20 min, ozone activated rGO and (d) GO; (e) Raman spectra of native rGO and GO.

Graphene sheets with different oxidation degrees were tested with the same ALD process in order to demonstrate the potential to control the  $\text{RuO}_2$  loading with the control of the defect density. As shown in Figures 4.6 a-d, the density of  $\text{RuO}_2$  nanoparticles increased with the oxidation degree (density of structural defects and functional groups in graphene). This further shows that the ALD functionalization strategy can be applied to graphene oxide in various defect density states and that the ALD growth mechanism drives the particles to grow on defect sites and functional groups. This is in strong agreement with earlier work which demonstrated the growth of Pt particles on grain boundaries of CVD grown graphene during the ALD deposition<sup>123</sup>.

The electrochemical capacitive performances of the rGO and rGO/ $\text{RuO}_2$ -X electrodes were evaluated by cyclic voltammetry (CV) and galvanostatic charge/discharge tests. It can be seen from Figure 4.7 that the graphene seriously enhances the total electrochemical capacitance of the electrodes, thus the capacitance was considered to dominantly originate from the rGO (or rGO/ $\text{RuO}_2$ ), while the capacitance from the carbon cloth substrate was neglected for convenience in the forthcoming discussion.

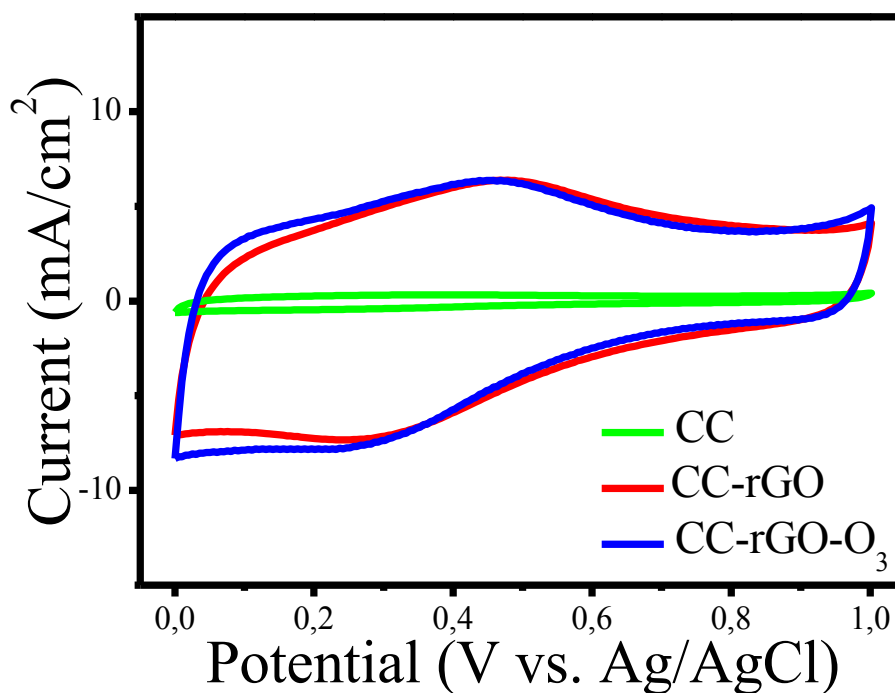


Figure 4.7. Cyclic voltammetry curves of native carbon cloth (CC), carbon cloth with rGO (CC-rGO) before and after  $\text{O}_3$  treatment of the electrodes at a scanning rate of 100 mV/s in 1 M aqueous  $\text{H}_2\text{SO}_4$ .

Figure 4.8 shows CV curves of electrodes containing bare rGO, rGO/RuO<sub>2</sub> after 15, 20, 30 and 50 ALD cycles at potential intervals ranging from 0-1 V vs. Ag/AgCl. The curves were measured in a three-electrode setup in 1 M aqueous H<sub>2</sub>SO<sub>4</sub> and the scanning rates were varied between 10 and 100 mV/s as indicated. In Figure 4.3.8 a, redox peaks can be observed in the CV of the rGO sample, which can be attributed to defects and chemical functional groups existent on the rGO, which are presumably active sites for redox reactions during the CV scanning. Those defects are most likely the intrinsically present oxidized sites of the rGO. Similar peaks have also been observed in studies of the capacitive performance of carbon nanotube/graphene composites<sup>124</sup>.

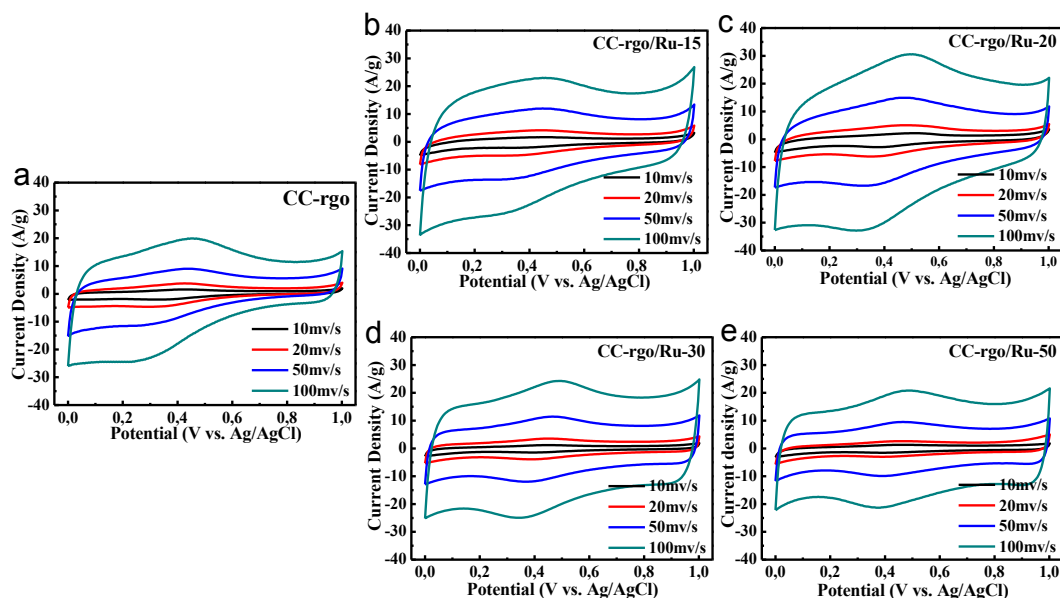


Figure 4.8. Cyclic voltammetry curves of (a) rGO, (b) rGO/RuO<sub>2</sub>-15, (c) rGO/RuO<sub>2</sub>-20, (d) rGO/RuO<sub>2</sub>-30 and (e) rGO/RuO<sub>2</sub>-50 at scanning rates of 10, 20, 50 and 100 mV/s, measured in 1 M aqueous H<sub>2</sub>SO<sub>4</sub> in a three-electrode setup.

As the number of ALD cycles increased, the CV curves of rGO/RuO<sub>2</sub>-X electrodes also gradually changed their shape becoming more symmetric and rectangular. The oxidation peak gradually shifted from around 0.42V (rGO and rGO/RuO<sub>2</sub>-15) to 0.49V (rGO/RuO<sub>2</sub>-20), and further to 0.5V (rGO/RuO<sub>2</sub>-30), which is obviously related to the increasing quantity of RuO<sub>2</sub>. The growing RuO<sub>2</sub> nanoparticles substitute the defects and functional groups of the graphene, thus the

oxidation peak can be attributed to the Faradaic electrochemical reaction related to  $\text{RuO}_2$ <sup>105,125–127</sup>. With higher loading, the contribution of  $\text{RuO}_2$  increases. This is particularly expressed with the rGO/ $\text{RuO}_2$ -30 electrode as depicted in Figures 4.8 d and e. Here, the CV curves approach higher symmetry. However, a better performance does not necessarily stand in direct relation to the increasing quantity of  $\text{RuO}_2$ . The current density showed highest values with samples after 20  $\text{RuO}_2$  deposition cycles. Both higher and lower numbers of cycles resulted in lower current densities. The calculated specific capacitances of rGO and rGO/ $\text{RuO}_2$ -X, based on charge/discharge measurements in the same three-electrode system, are shown in Figure 4.9 a. The unmodified rGO electrode shows a specific capacitance of 184 F/g at a discharging rate of 1 A/g, which is in agreement with reports from literature.<sup>100</sup> In comparison, the rGO/ $\text{RuO}_2$  samples showed a significant increase with the best value being 278 F/g, which is an increase of ~51%. However, the corresponding sample was produced with 20 ALD cycles and contained very low amounts of  $\text{RuO}_2$  (~9.3wt% of Ru) as measured with inductively coupled plasma-mass spectrometry (ICP-MS).

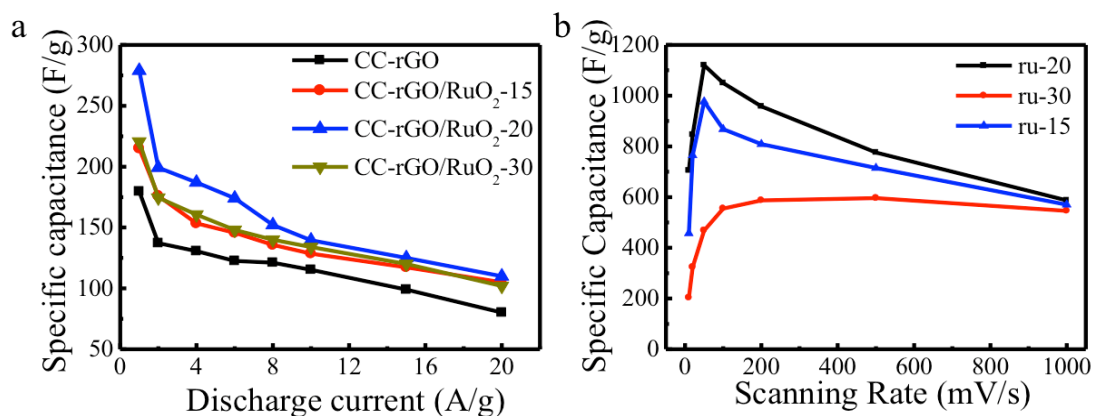


Figure 4.9 Calculated specific capacitances of (a) composites of rGO/ $\text{RuO}_2$  with cycle numbers as depicted in the graph and (b)  $\text{RuO}_2$  nanoparticles only. See the experimental section of this chapter for the details of the calculation methods.

The specific capacitances of the rGO/ $\text{RuO}_2$  electrodes don't correlate with the increase of the  $\text{RuO}_2$  quantity in Figure 4.9 a. This may have various reasons. On the one hand, the particle size may play an important role. Namely, with increasing particle size the surface to volume ratio of the  $\text{RuO}_2$  decreases. Without any doubt, an

optimal surface to volume ratio of RuO<sub>2</sub> exists. As the Faradaic reaction only takes place at the near surface area, only the RuO<sub>2</sub> located at the surface or in subsurface areas of the particles is involved in the reaction. From the electrochemical point of view, the best performance can only be obtained at a critical point, where the total content of RuO<sub>2</sub> in the nanoparticles is considered as accessible surface species and no or just a minimum of bulk type RuO<sub>2</sub> is present. Any further increase of the RuO<sub>2</sub> quantity will alter this delicate balance with negative impact on the specific capacitance. On the other hand, the interface chemistry of the RuO<sub>2</sub> and the rGO may have an impact on the capacitance. The oxidized parts of the rGO can be considered defects that affect the capacitance of graphene. Binding Ru to those defects will chemically modify the substrate by substituting C-O sites with C-O-Ru in the first place and subsequently grow further as RuO<sub>2</sub>. The nature of the bonding is of critical importance for best possible synergy of the materials. In our case, the bonding is covalent and direct, i.e. without linkers or mediators, thus enabling direct electron transfer between the materials. Such synergies between the constituting materials add value to the specific capacitance of the electrode, beyond the theoretical individual contributions of the involved materials.

The specific capacitances of RuO<sub>2</sub> only within the samples processed with 15, 20 and 30 ALD cycles were calculated and compared (Figure 4.9 b). The maximum specific capacitance of RuO<sub>2</sub> is observed at a scanning rate of 50 mV/s instead of 10 mV/s, indicating a serious contribution of the active sites to the capacitance at low scanning rates. The RuO<sub>2</sub> nanoparticles grew on defects or functional groups of the rGO, thus part of the capacitance can be attributed to RuO<sub>2</sub> substituting the capacitance of the initial, unaltered active sites. A similar effect has been observed for the specific capacitance of MnO<sub>2</sub> from porous gold/MnO<sub>2</sub> hybrid electrodes<sup>128</sup>. The highest value for the specific capacitance of RuO<sub>2</sub> was 1132 F/g that is very close to the theoretical value (1300-1500 F/g)<sup>125,129</sup>.

A very interesting relation of specific capacitance and number of ALD cycles can be observed in Figure 4.9 b, namely the peak values are highest with samples processed with 20 cycles, while higher and lower cycle numbers result in lower peak values. This peculiar behavior indicates that the composite undergoes a modification more complicated than the simple attachment of nanoparticles to the substrate and their growth. Although further investigations have to be performed in order to gain more clarity, we propose that the initial deposition of RuO<sub>2</sub> with few ALD cycles only

results in an increasing replacement of oxidized carbon groups on defect sites with Ru, thus altering the effects of the intrinsic defects of the rGO. The deposited  $\text{RuO}_2$  is fully accessible for the Faradaic reaction and enhances the specific capacitance of the electrode. With 20 cycles, a peak value is reached, which indicates that nearly all defect sites have been saturated with  $\text{RuO}_2$  (Figure 4.10 b). Further deposition of  $\text{RuO}_2$  emphasizes the  $\text{RuO}_2$  contained in the growing nanoparticles on the expense of the specific capacitance rather than the fraction bound to rGO (Figure 4.3.10 c).

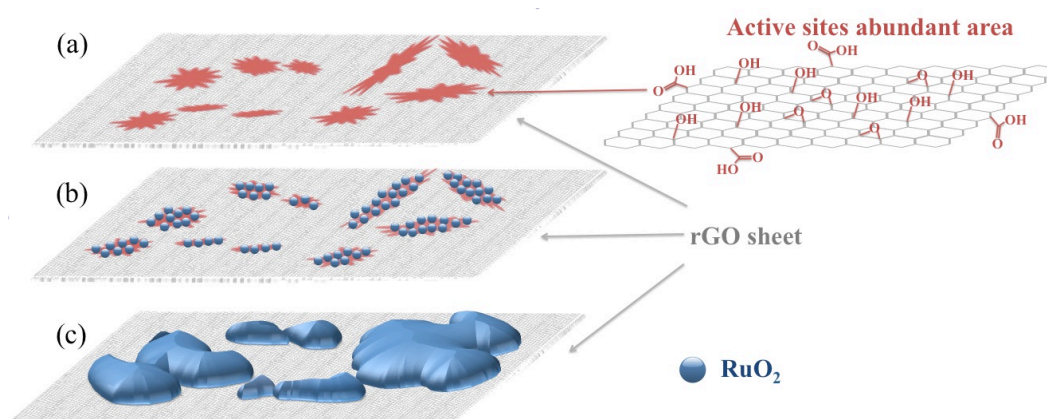


Figure 4.10. Schematic of the morphology of ALD deposited  $\text{RuO}_2$  on rGO. (a) rGO sheet with active sites, (b)  $\text{RuO}_2$  nanoparticles fully replace the defects on rGO sheets (corresponding to 20 deposition cycles), (c)  $\text{RuO}_2$  nanoparticles merge with nearby particles to form a bulk  $\text{RuO}_2$  (corresponding to 30, 50 or even more deposition cycles).

We chose the above-mentioned rGO/ $\text{RuO}_2$ -20 electrode for further studying the properties under more realistic conditions, i.e. in a classical two-electrode configuration using filter paper as separator and 1 M aqueous  $\text{H}_2\text{SO}_4$  as electrolyte. In contrast to the CV curves of the bare rGO electrodes (Figure 4.11 a), the CC-rGO/ $\text{RuO}_2$ -20 samples show an almost perfect symmetric rectangular shape, characteristic of a perfect capacitor (Figure 4.11 b). Obviously, the rGO/ $\text{RuO}_2$  composite absorbs the  $\text{H}^+$  cations in a fast, reversible and successive way, showing its great suitability as electrode for electrochemical capacitors. The absence of redox peaks can be explained with the devices having been charged and discharged at a pseudo-constant rate over the entire voltammetric range<sup>128</sup>. In the galvanostatic charge/discharge tests, the charging and discharging times for CC- rGO/ $\text{RuO}_2$ -20

samples are much shorter than those for the CC-rGO samples in Figures 4.11 c and d, indicating a higher capacity.

Resulting from the galvanostatic charge/discharge test, the specific capacitances of rGO and rGO/RuO<sub>2</sub>-20 were calculated to be 106 F/g and 148 F/g (Figure 4.12), respectively, at a 1 A/g discharging rate. Although the increase of ~40% is somewhat lower than the ~51% obtained with the three-electrode setup, it is significant, particularly in view of the very low amount of material loaded. For a better comparison and evaluation the RuO<sub>2</sub> utilization, the individual contributions of RuO<sub>2</sub> and rGO to the energy density of the electrode at the designated values of power density are shown in the Ragone plot in Figure 4.12 b. Given the significantly lower loading with RuO<sub>2</sub>, the total energy density of the composite is lower than that of the composites described in relevant literatures.

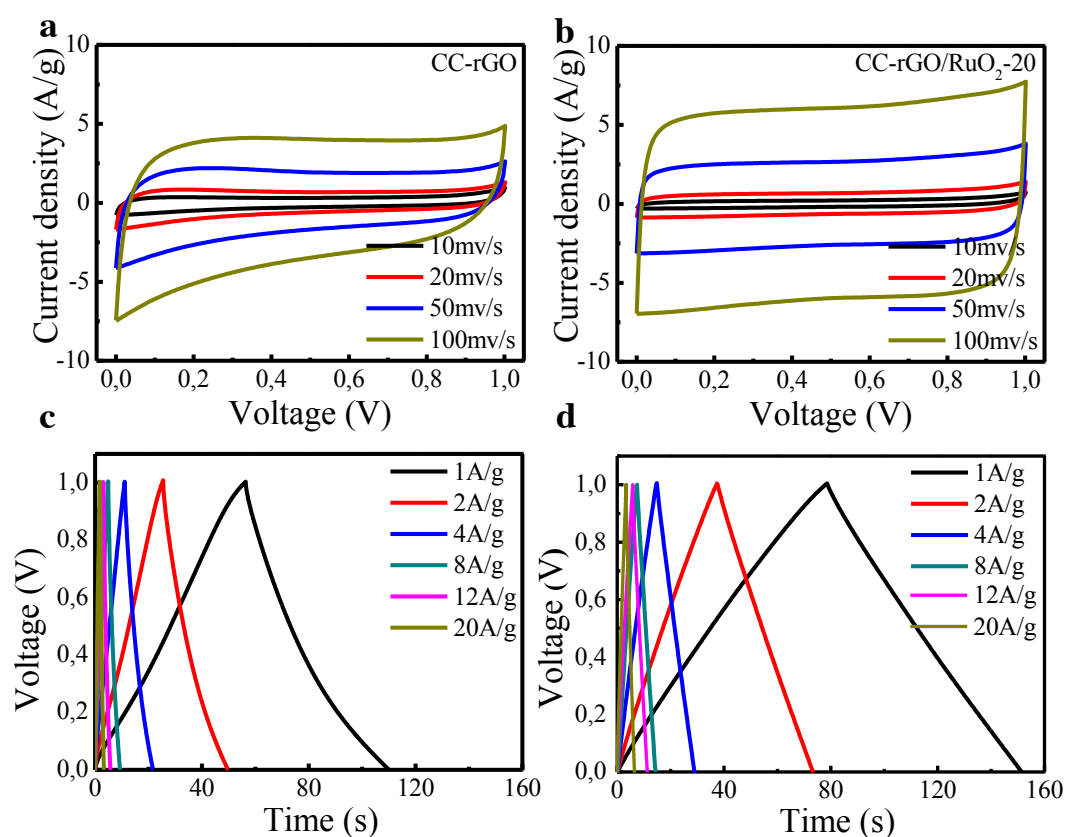


Figure 4.11. Cyclic voltammetry curves of (a) rGO, and (b) rGO/RuO<sub>2</sub>-20 at various scanning rates. Charge-discharge measurements of (c) CC-rGO and (d) CC-rGO/RuO<sub>2</sub>-20 at various charging-discharging rates. All measurements were performed in 1 M aqueous H<sub>2</sub>SO<sub>4</sub> in a two-electrode setup.

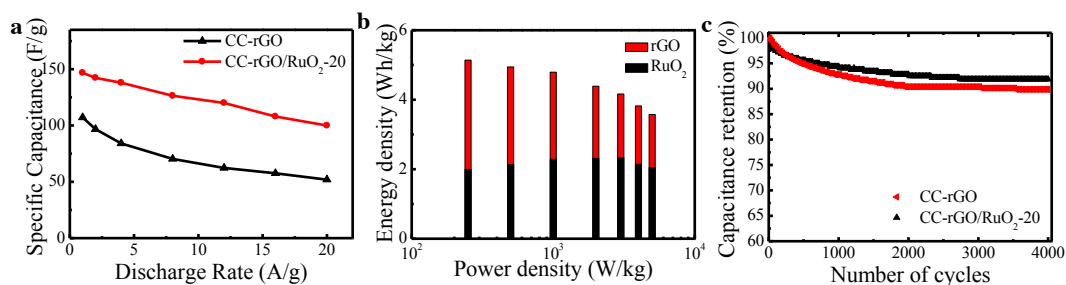


Figure 4.12. (a) Calculated specific capacitances of rGO and rGO/RuO<sub>2</sub>-20. (b) Ragone plot of energy density vs. power density of this work indicating the individual contributions of rGO and RuO<sub>2</sub> to the energy density. (c) Cycling stability of rGO and rGO/RuO<sub>2</sub>-20 electrodes measured by cyclic voltammetry at a scanning rate of 100 mV/s.

The more interesting aspect is, however, related to the individual contributions of the constituting materials of the composite. A closer look to the bars in Figure 4.12 b reveals that the total energy density is composed of significant contributions of rGO and RuO<sub>2</sub>, indicating serious exploitation of both constituents. A more peculiar effect can be seen from the lower, black parts of the columns showing that the specific energy density contribution by RuO<sub>2</sub> is constant against the power density, thus stabilizing the electrode towards higher power densities. Namely, with increasing power density the contribution of RuO<sub>2</sub> to the specific energy density increases to a peak value and subsequently decreases again. This effect can be attributed to the defect-optimized rGO. Namely, the oxidized carbon sites are nearly fully replaced with RuO<sub>2</sub>, which is fully involved in the Faradaic reaction.

In addition to the size control, another great advantage of the ALD approach lies in the chemical bonding of RuO<sub>2</sub> nanoparticles to graphene sheets, which is intrinsic to the ALD processes. This tight chemical bonding can largely prevent the agglomeration of RuO<sub>2</sub> nanoparticles, which is one of the major obstacles causing performance degradation of supercapacitors based on nanoparticle related materials or structures. Indeed, the resulting rGO/RuO<sub>2</sub> based device becomes very stable during cycling. Figure 4.12 c shows that the rGO electrodes have a retention of ~90%, while the rGO/RuO<sub>2</sub>-20 have a value of ~92% after 4000 CV cycles at a scanning rate of 100 mV/s. These results are significantly higher than those reported in literature<sup>104,105,125,129</sup>.

## 4.4 Conclusions

In this chapter, ALD is demonstrated as a method-of-choice for defect management in rGO. The intrinsically present oxidized carbon can be precisely modified with functional materials and in this way the electronic properties efficiently altered. On the example of a supercapacitor, a controlled deposition of RuO<sub>2</sub> resulted in electrodes with excellent capacitive performance and stability. This excellent performance is a consequence of the selective chemical binding of RuO<sub>2</sub> to defect sites of the rGO substrate that changes the chemical nature of those defects. Within the range of few ALD deposition cycles only, the specific capacitance of the electrode can be maximized, which in realistic circumstances yields an ideal capacitor with stable energy densities over a broad range of power densities. The deposited RuO<sub>2</sub> is tightly bound, thus agglomeration of the formed nanoparticles is prevented. The possibility to identify the optimal loading with RuO<sub>2</sub> and the precise control of the growth by ALD, allows a more economical fabrication of such composite electrodes in addition to saving resources. Current state of the art ALD instrumentation uses high-speed valves and thus offers good control over the precursor dosing, which in an optimized process allows for decreasing the precursor consumption to a minimum of waste. Combined with simplicity and potential for up scaling towards mass-production, ALD has great potential to become the method of choice to modify a range of substrates with various interesting functional materials in a similar way.



---

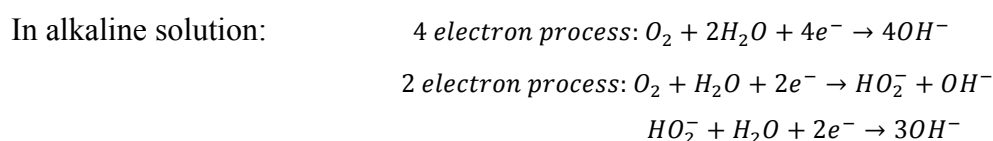
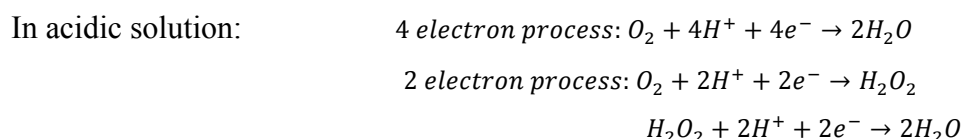
# Chapter 5

## Functionalized Nanoparticles on Carbon Nanotubes by ALD

Similar to previous chapters, an application driven selection of substrate and ALD process was chosen in order to match the properties of desire, and also demonstrate the versatility of the process. This chapter reports on the growth of functional  $\text{Co}_3\text{O}_4$  nanoparticles on carbon nanotubes (CNTs) with perfect distribution in both position and size by ALD. The fabricated  $\text{Co}_3\text{O}_4/\text{CNT}$  composite exhibits excellent oxygen reduction reaction (ORR) activity. As a further development, a coating step for covering the nanoparticles with a nitrogen doped carbon shell is introduced. Owing to the embedding, the nanoparticles are immobilized, resulting in the stability over long-term operation being greatly enhanced and at the same time the ORR activity being maintained.

### 5.1 Introduction

The oxygen reduction reaction (ORR) is of great importance for both life science processes, like biological respiration, and energy converting systems like fuel cells or batteries. The ORR process in aqueous solution occurs mainly in two pathways: the four-electron transfer process reducing  $\text{O}_2$  directly to  $\text{H}_2\text{O}$ , and the two-electron transfer process reducing  $\text{O}_2$  to  $\text{H}_2\text{O}_2$ . The ORR in acidic and alkaline aqueous solutions are formulated as follows.



The sluggish kinetics of the ORR at the cathode is one of the largest obstacles for the massive use of a variety of fuel cells or metal-air batteries.<sup>130–132</sup> The efficiency of the ORR catalyst determines with great share the overall performance of the device or system, which makes it a crucially important component. Seemingly, a set of good catalysts has been identified with platinum or its alloys exhibiting exceptional catalytic performance and efficiency<sup>133–135</sup>. However, use of platinum in large quantities for mass production is economically not feasible. Moreover, Pt-based catalysts often suffer from electrochemical and temporal instability, which is primarily a result of the highly reactive Pt-based nanostructures. The stability of a catalyst in long-term operation is considered to be one of the most important hurdles to be overcome for implantation into real devices and commercialization. Thus, finding cheap, efficient and stable alternatives to Pt for the ORR is highly desired.

The recent years have witnessed a tremendous progress in identifying and characterizing such cost-effective and efficient catalysts for the ORR, like nitrogen (N) or transition metal (M) doped carbon or M-N co-doped carbon<sup>136–139</sup>. Besides carbon-based materials, transition metal oxides came into focus as good alternatives for the non-noble metal based ORR catalysts. In various attempts,  $\text{Fe}_3\text{O}_4$ <sup>140</sup>,  $\text{Co}_3\text{O}_4$ <sup>141</sup>,  $\text{CoO}$ <sup>142</sup> and some further oxides<sup>143–146</sup> were shown to be excellent candidates. Those often have comparable or sometimes even slightly better reactivity than Pt, which gives rise to optimism for finding a suitable system to replace Pt, at least from the perspective of activity. However, the stability/durability for long-term operation still remains being a great challenge<sup>147</sup>.

The proposed metal oxide-based catalysts for ORR consist of a variety of nanostructures. The collapse of nanostructures, like leaching or agglomeration of active materials seriously contribute to the instability of the catalyst<sup>147</sup>. Maintaining this nano-architecture during operation is expected to ensure long-term stability and preserve high activity, but this is a great challenge. In the following, we describe our approach towards stabilizing the ORR catalyst. The system is based on  $\text{Co}_x\text{O}_y$  nanoparticles that are grown on carbon nanotubes (CNTs). For stabilization, the system was covered with a thin N-doped carbon shell by coating the CNT-nanoparticle composite with polydopamine (PDA) and subsequent pyrolysis. The final construct of nanoparticles, CNTs and doped carbon, will be referred to as  $\text{Co}_x\text{O}_y/\text{CNT}@C$  in the following. The stability and durability of the  $\text{Co}_x\text{O}_y/\text{CNT}@C$ , if compared to the commercial Pt/C, is truly exceptional. After a standard cycling test,

the half wave potential of  $\text{Co}_x\text{O}_y/\text{CNT}@C$  showed a negative shift of only 21 mV after 10.000 cycles, which is one third of that observed with the commercial Pt/C (63 mV). Furthermore, after 100.000 s operation at a constant potential the current decreased by only 17%, which is only half of the decrease observed from Pt/C (35%). This exceptional stability and durability of  $\text{Co}_x\text{O}_y/\text{CNT}@C$  is a result of the special architecture, in which the N-doped carbon shell prevents the embedded  $\text{Co}_x\text{O}_y$  nanoparticles from agglomeration and detaching off of the CNTs. This synthetic strategy and the resulting nano-architecture are not specific for this problem but may also be applied more universally, showing promise for a plethora of further energy-related or catalytic applications.

## 5.2 Experiments

### Materials synthesis

Atomic layer deposition (ALD) was used to deposit  $\text{Co}_3\text{O}_4$  onto commercial multi-walled carbon nanotubes (MNCNTs) in a commercial ALD coater (Savannah 100, Cambridge Nanotech Inc.). Bis(cyclopentadienyl) cobalt (II) ( $\text{Co}(\text{Cp})_2$ ) and  $\text{O}_3$  were used as cobalt and oxygen sources. The reactor was kept at 200 °C, and the  $\text{Co}(\text{Cp})_2$  source was maintained at 65 °C. High purity  $\text{N}_2$  (99.99%) was used as both carrier and purging gas. All gas lines were kept at 120 °C to prevent cold spots and precursor condensation. For each ALD cycle, the pulse time, exposure time and purging time of  $\text{Co}(\text{Cp})_2$  and  $\text{O}_3$  precursors were 1 s/ 60 s/ 90 s and 0.8 s/ 60 s/ 90 s, respectively.

CNT or  $\text{Co}_3\text{O}_4/\text{CNT}$  were dispersed in water (6 mg/mL), then mixed with 60 mM Tris buffer (PH 8.8) and 6 mg/mL dopamine solution in a ratio of 1:1:1. The mixed solution was stirred for 24 hours at room temperature. Afterwards, the samples were washed by centrifugation with water for at least three times, then dried and collected.

The collected  $\text{Co}_3\text{O}_4/\text{CNT}$ ,  $\text{CNT}@PDA$  or  $\text{Co}_3\text{O}_4/\text{CNT}@PDA$  samples were annealed in an oven at elevated temperatures (400 to 800 °C) under  $\text{N}_2$  flow in vacuum ( $10^{-9}$ - $10^{-10}$  mbar) for 2 hours individually. The  $\text{Co}_3\text{O}_4/\text{CNT}$ ,  $\text{CNT}@PDA$  and  $\text{Co}_3\text{O}_4/\text{CNT}@PDA$  were also annealed in-situ in an XPS chamber without exposure to air before measuring.

## Physical characterization

Electron microscopy samples were prepared by drop-drying ethanolic suspensions of the samples onto copper grids. The morphologies and microstructures of the synthesized samples were characterized with scanning transmission electron microscopy (FEI, Helios 450S). Transmission electron microscopy (FEI, Titan G2 60-300) was carried out to characterize the structure of the nanoparticles and to perform element analysis at higher magnifications. XRD examinations were performed with a powder diffractometer (X'pert, PANalytical). XPS experiments were performed using a Phoibos photoelectron spectrometer equipped with an Al K $\alpha$  X-ray source as the incident photon radiation. Samples were drop-dried onto silicon or gold substrates, using the Si 2p or the Au 4f signals for binding energy calibration. In-situ heating experiments were performed inside the UHV chamber, with a base pressure of  $10^{-9}$  mbar. XPS spectra of Co 2p, O 1s, N 1s and C 1s core levels were measured for Co<sub>3</sub>O<sub>4</sub>/CNT, CNT@PDA and Co<sub>3</sub>O<sub>4</sub>/CNT@PDA as received (RT) and after annealing processes at 400 °C (below the ex-situ annealing process) and at 600 °C (ex-situ annealing process).

## Electrochemical characterization

For the catalyst preparation, 2 mg of a sample were dispersed in a mixture of 750  $\mu$ l water, 200  $\mu$ l ethanol and 50  $\mu$ l Nafion solution (5 wt.%), and then ultrasonicated for 15 min to form a homogeneous ink. For the electrochemical measurements 20  $\mu$ l of the catalyst ink was loaded onto a glassy carbon electrode of 5 mm in diameter (loading 0.20 mg/cm<sup>2</sup>). Commercial Pt/C catalyst samples were prepared in the same way. The catalytic performances of the catalysts were analyzed in a standard three-electrode system with a Pt sheet as counter electrode and Ag/AgCl (3 M KCl) as reference electrode in 0.1 M KOH solution. The electrolyte was saturated with O<sub>2</sub> (or N<sub>2</sub>) by bubbling O<sub>2</sub> (or N<sub>2</sub>) prior to the start of each experiment. Cyclic voltammetry (CV) tests were performed in both O<sub>2</sub> and N<sub>2</sub> saturated 0.1 M KOH electrolytes at a scanning rate of 50 mV/s. Before recording the data, the electrodes were cycled at least 5 times until a stable curve was obtained. Linear sweep voltammetry (LSV) was also carried out in O<sub>2</sub> saturated 0.1 M KOH at a scanning rate of 10 mV/s with a rotating electrode speed ranging from 400 to 2500 rpm. The Koutecky–Levich plots ( $J^{-1}$  vs.  $\omega^{-1/2}$ ) were analyzed at various electrode potentials.

The slopes of their linear fit lines were used to calculate the number of electrons transferred ( $n$ ) based on the Koutecky-Levich equation below:

$$\frac{1}{J} = \frac{1}{J_L} + \frac{1}{J_K} = \frac{1}{B\omega^{1/2}} + \frac{1}{J_K}$$

$$B = 0.62nFC_o(D_o)^{2/3}\nu^{-1/6}$$

$$J_K = nFkC_o$$

where  $J$  is the measured current density,  $J_L$  is the diffusion-limiting current density,  $J_K$  is the kinetic-diffusion-limiting current density,  $\omega$  is the angular velocity,  $n$  is the electron number transferred,  $F$  is the Faraday constant,  $C_o$  is the bulk concentration of  $O_2$ ,  $\nu$  is the kinematic viscosity of the electrolyte, and  $k$  is the electron-transfer rate constant. For the Tafel plot, the kinetic current density was calculated according to the equation:

$$J_K = \frac{J * J_L}{J_L - J}$$

The cycling stabilities were characterized using CVs with a small potential window at high scanning rates of 500 mV/s for 10.000 cycles. After every 1.000 cycles LSVs were recorded (scanning rate 10 mV/s, rotating speed 1600 rpm). The durability tests were carried out by chronoamperometry at a bias potential of 0.65 V (vs. RHE) for 100.000 s in the constantly  $O_2$ -saturated electrolyte with a rotating speed of 1600 rpm. All electrochemical tests were carried out using an Autolab electrochemical workstation (PGSTAT 302N).

## 5.3 Results and Discussion

Atomic layer deposition (ALD) was applied to deposit cobalt oxide onto commercial carbon nanotubes (CNTs, Figure 5.1 a), as it offers the possibility to grow uniformly distributed oxide nanoparticles on complex surfaces or structures with extreme control<sup>8,107</sup>. Cobaltocene ( $CoCp_2$ ) and  $O_3$  were used as metal and oxygen sources. In our earlier work<sup>114,148</sup>, we demonstrated that  $O_3$  preferentially oxidizes the carbonaceous debris on the outer wall of CNT, creating functional groups or defects. These functional groups or defects act as anchoring sites for the chemisorption of  $CoCp_2$  during the initiation of the ALD growth. Subsequently supplied  $O_3$  will react with the immobilized Co precursor to produce  $Co_3O_4$ . Due to the discrete anchoring sites on the otherwise inert surfaces of the CNTs, an island growth rather than a

compact film growth is favored<sup>115</sup>. After the initial few cycles,  $\text{Co}_3\text{O}_4$  seeds are formed on the CNTs, which in the continuation of the process act as preferential sites for further  $\text{Co}_3\text{O}_4$  deposition, giving rise to a particle growth throughout the deposition process. Consequently, uniformly distributed  $\text{Co}_3\text{O}_4$  nanoparticles are formed on CNTs (Figures 5.1 b-e). By altering the number of ALD cycles, the size of nanoparticles can be further optimized.

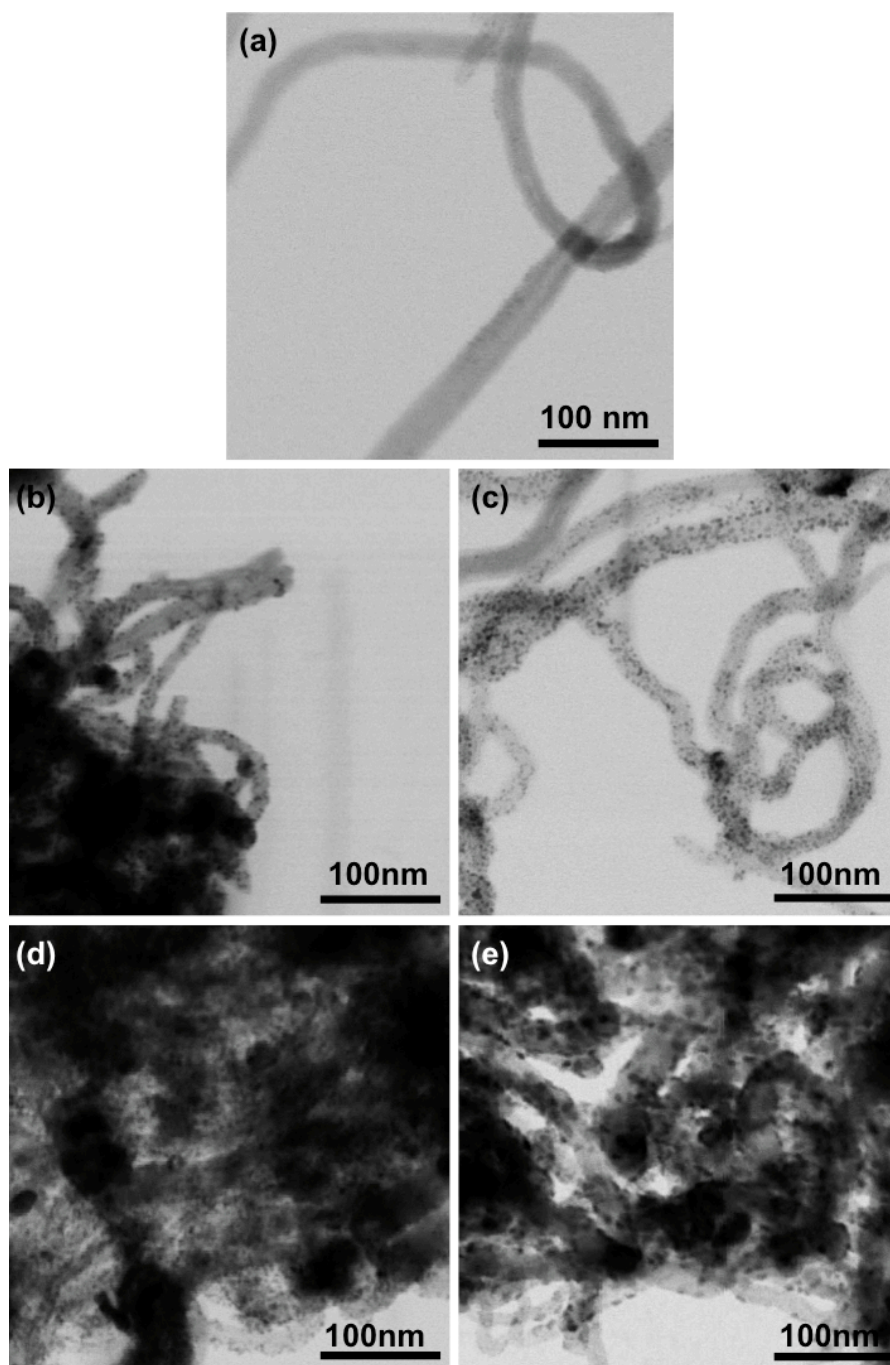


Figure 5.1 STEM images of (a) pristine CNTs and  $\text{Co}_3\text{O}_4$  nanoparticles grown on CNTs by ALD with (b) 100 cycles, (c) 300 cycles, (d) 500 cycles and (e) 700 cycles.

After the  $\text{Co}_3\text{O}_4$  deposition,  $\text{Co}_3\text{O}_4/\text{CNTs}$  were further coated with a thin layer of polydopamine (PDA) (Figure 5.2) by suspending the composite in a dopamine solution and gently stirring at room temperature, as dopamine tends to oxidatively self-polymerize in appropriate pH environment<sup>149–151</sup>. An inspection of a PDA-coated sample with high magnification STEM (Figure 5.3) revealed that the PDA layer uniformly covered the surface of the CNTs, including the  $\text{Co}_3\text{O}_4$  nanoparticles.

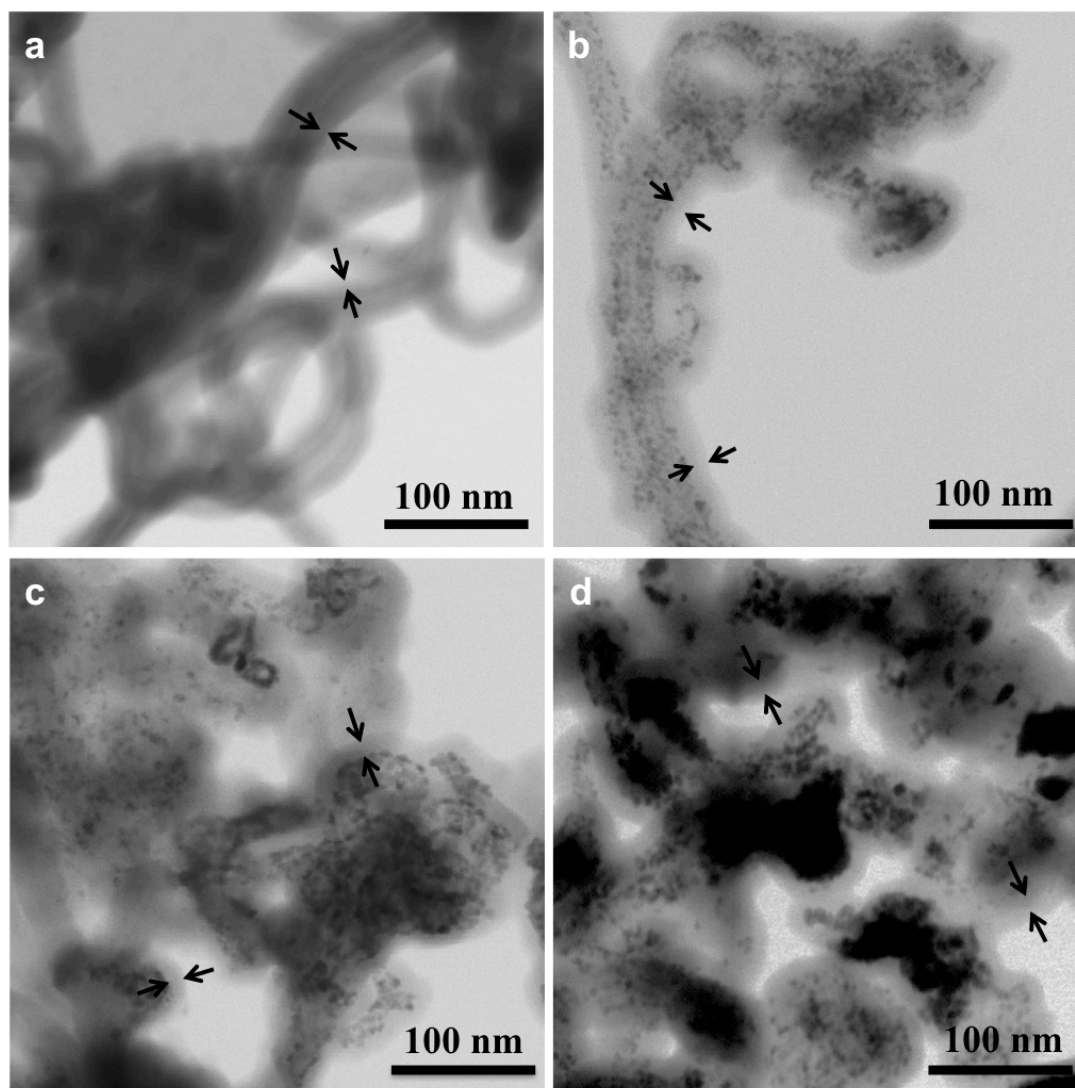


Figure 5.2 STEM image of PDA coated (a) CNTs, (b) Co-300/CNTs, (c) Co-500/CNTs and (d) Co-700/CNTs. The homogeneous light gray shadow indicated by the arrows shows the polymer coating.

In the next step, the  $\text{Co}_3\text{O}_4/\text{CNT@PDA}$  samples were annealed at elevated temperatures in a  $\text{N}_2$  atmosphere. The annealing resulted in the PDA polymer decomposing to an embedding carbon shell and a slight growth of the nanoparticles

due to some limited Ostwald ripening (Figure 5.4). The size of the final nanoparticles also depends on the initially applied number of ALD cycles. As the cycle number increases, the density of the  $\text{Co}_3\text{O}_4$  increases (Figure 5.1), and the nanoparticles will merge and grow during annealing. The PDA layer also plays a role here, as it will decrease the mobility of the nanoparticles, thus seriously lowering the final particle size as shown in Figure 5.5.

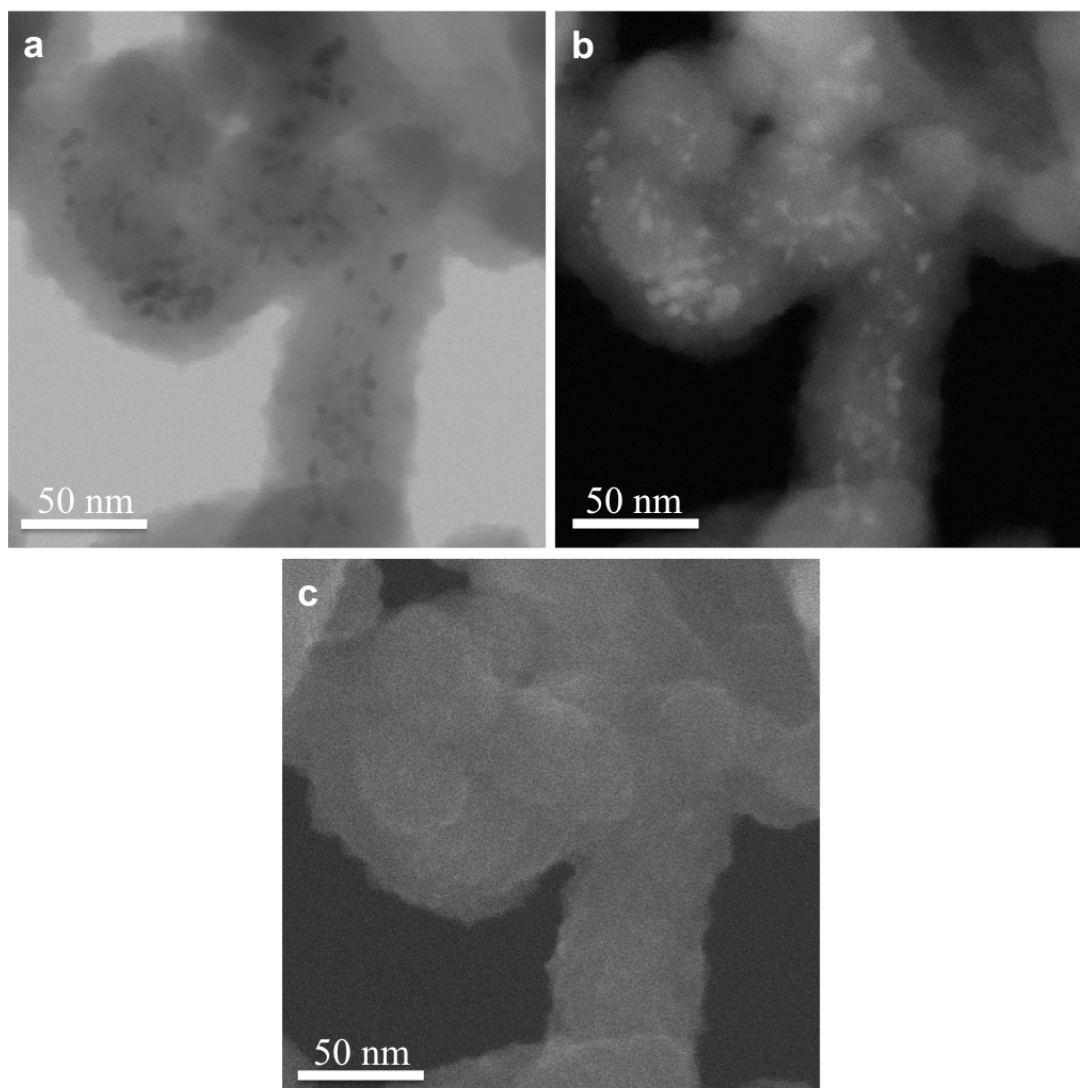


Figure 5.3. High magnification STEM images of  $\text{Co}_3\text{O}_4/\text{CNT}@PDA$  (a) bright field, (b) dark field and (c) morphology.

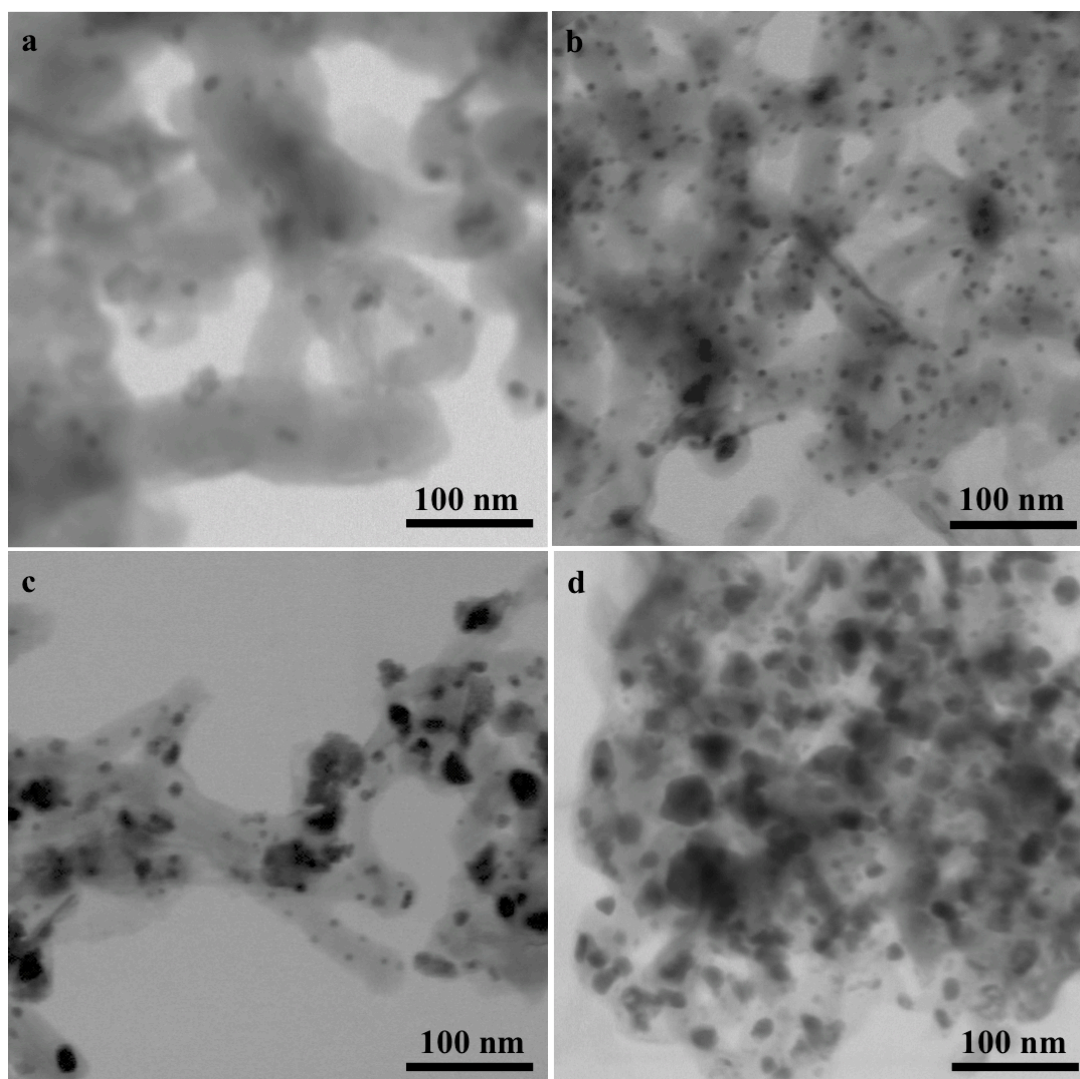


Figure 5.4 STEM images of  $\text{Co}_3\text{O}_4/\text{CNT}@PDA$  after (a) 100 cycles, (b) 300 cycles, (c) 500 cycles and (d) 700 cycles of ALD and subsequent annealing at  $600\text{ }^\circ\text{C}$  for 2 hours.

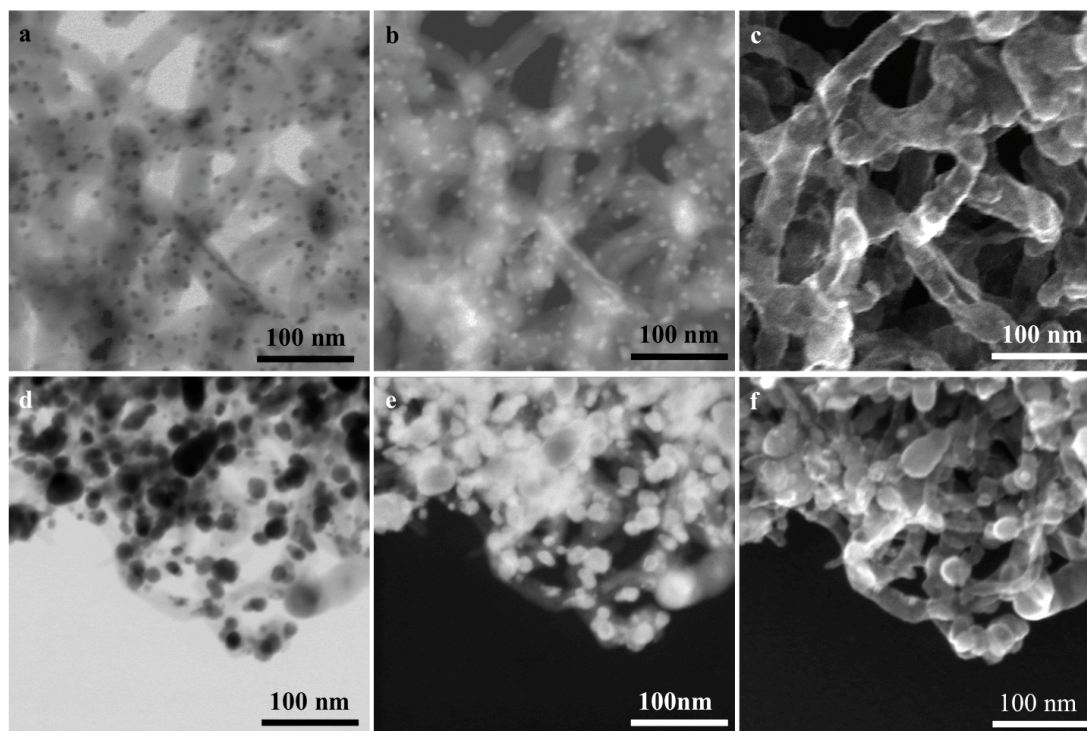


Figure 5.5 STEM images of  $\text{Co}_x\text{O}_y/\text{CNT}@C$ : (a) bright field, (b) dark field, (c) morphology and  $\text{Co}_x\text{O}_y/\text{CNT}$  (d) bright field, (e) dark field, (f) morphology.

X-ray diffraction patterns were collected to trace the evolution of the oxide nanoparticles upon annealing. In Figure 5.6 a, the peak at  $26.2^\circ$  corresponds to the (002) plane of CNTs, while clear peaks at  $31.2^\circ$ ,  $36.7^\circ$ ,  $44.7^\circ$ ,  $59.2^\circ$  and  $65.2^\circ$  for  $\text{Co}_3\text{O}_4/\text{CNT}$  occur, corresponding to (022), (113), (004), (115) and (044) planes of  $\text{Co}_3\text{O}_4$ , respectively. After annealing, new peaks at  $44.2^\circ$  and  $51.4^\circ$  appear, associated to (111) and (002) planes of Co metal, while all peaks characteristic for  $\text{Co}_3\text{O}_4$  decrease or even disappear. Further annealing conditions (at  $800^\circ\text{C}$ ), reduce the oxide to Co metal with all peaks in the XRD spectrum corresponding to the cubic structure of Co (Figure 5.6 b). This is consistent with previous observations:  $\text{Co}_3\text{O}_4$  releases O during heating under  $\text{N}_2$  flow, converting into CoO or even metallic Co<sup>152–154</sup>. Interestingly, element mapping of Co and O with Energy-Dispersive X-Ray spectroscopy (Figure 5.7) shows that  $\text{Co}_3\text{O}_4$  nanoparticles transformed into core-shell particles with a metallic core and an oxide shell.

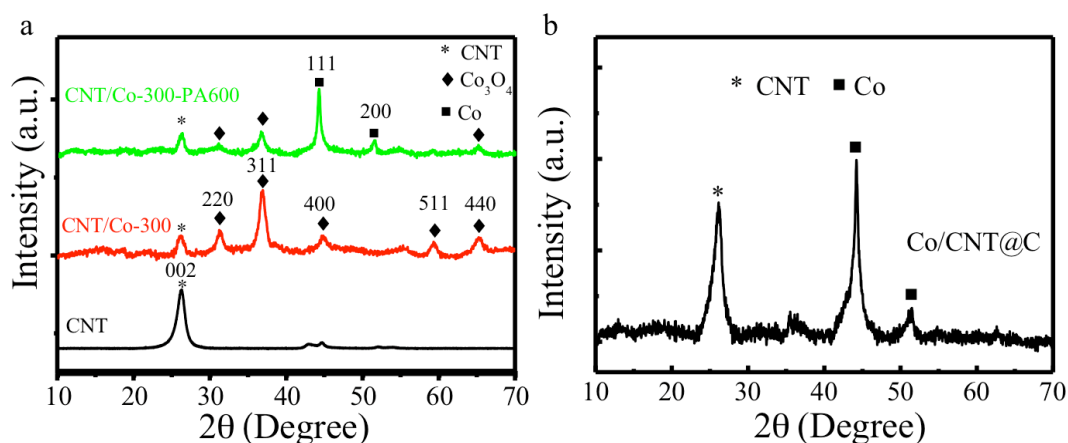


Figure 5.6. X-ray diffraction patterns of (a) (1) pristine CNTs, (2) CNT after  $\text{Co}_3\text{O}_4$  coating by ALD and (3) PDA coated  $\text{Co}_x\text{O}_y/\text{CNT}$  after annealing at 600 °C and (b) PDA coated  $\text{Co}_x\text{O}_y/\text{CNT}$  after annealing at 800 °C.

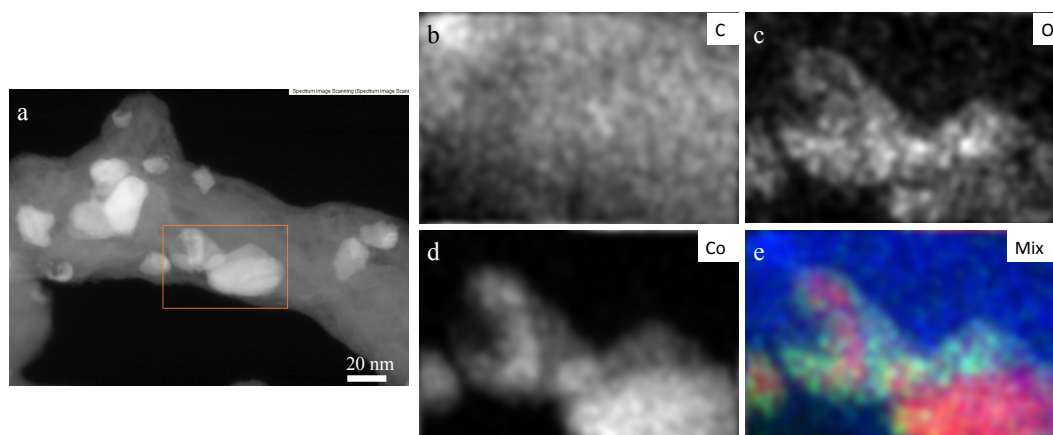


Figure 5.7. Element analysis of the fabricated  $\text{Co}_x\text{O}_y$  nanoparticles, (a) High-angle annular dark-field STEM image, (b)-(d) Elemental maps of the box area in (a) for (b) carbon (C), (c) oxygen (O), (d) cobalt (Co) and (e) mix of the elements: blue represents carbon, green represents oxygen and red represents cobalt.

High resolution TEM was applied to characterize the annealed sample ( $\text{Co}_x\text{O}_y/\text{CNT}@C$ ). Figure 5.8 shows that the oxide nanoparticles were still embedded in the carbon shell after annealing, but the lattice fringes indicate that the oxidation state of the nanoparticles has changed during the process. From HRTEM, in the outer shell the measured interplanar spacings of 0.24 nm and 0.20 nm may correspond to (113) and (004) planes of  $\text{Co}_3\text{O}_4$ ; alternatively, the 0.24 nm and 0.21 nm may correspond to (111) and (002) planes of cubic  $\text{CoO}$ ; while the spacings of 0.20 nm

and 0.17 nm in the inner core correspond to (111) and (002) planes of metallic Co. Note that according to the XRD spectrum of  $\text{Co}_x\text{O}_y/\text{CNT}@C$ , presence of some CoO phases, for example the (111) plane, may be possible, but with  $36.4^\circ$  it is too close to the (113) plane of  $\text{Co}_3\text{O}_4$  at  $36.7^\circ$  to be clearly distinguished.

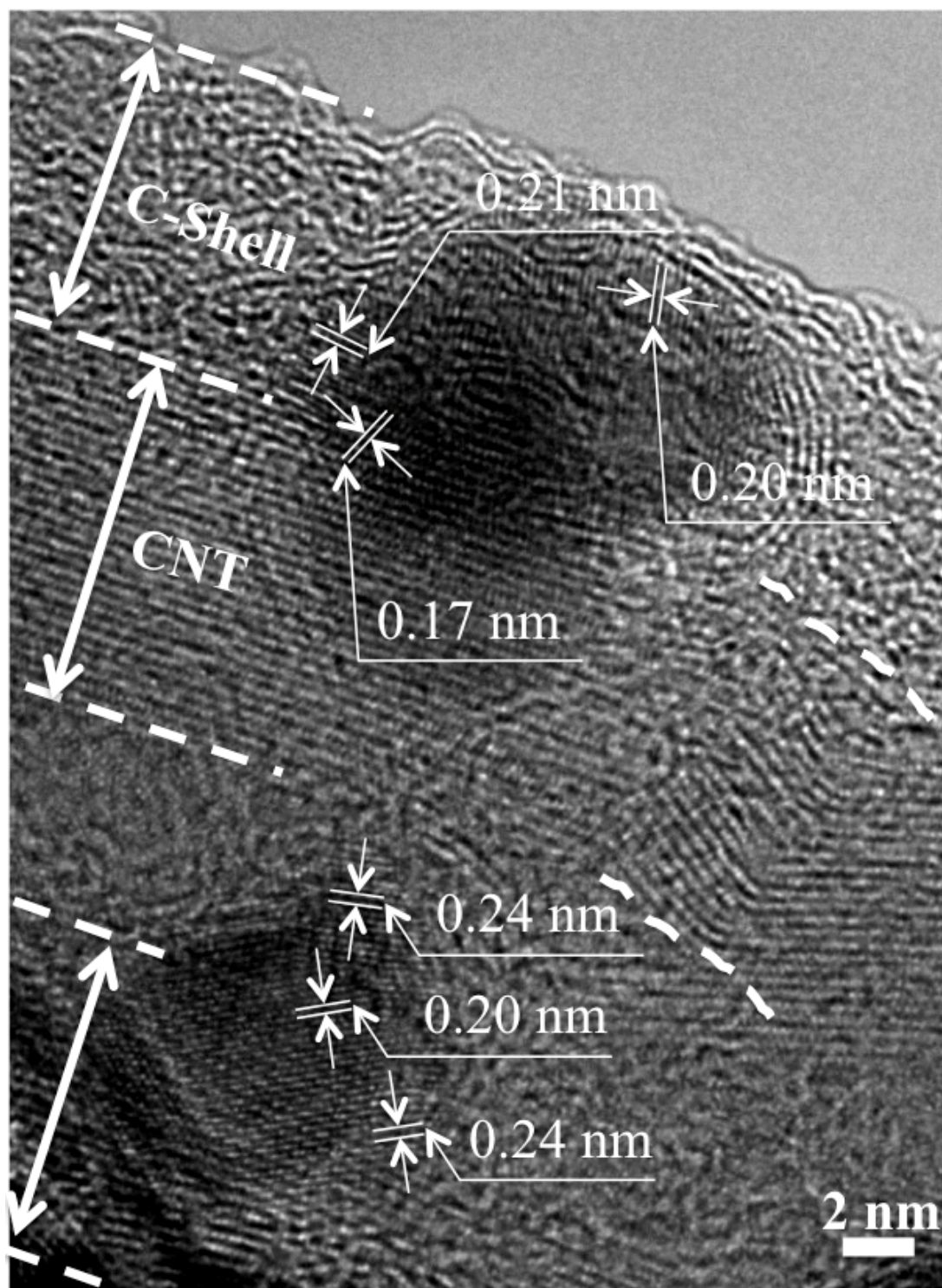


Figure 5.8 HRTEM image of  $\text{Co}_x\text{O}_y/\text{CNT}@C$ .

X-ray photoelectron spectroscopy (XPS) was used to analyze the elemental information of the synthesized materials. After the ALD process clear Co 2p core level peaks at around 779.7 eV (Co 2p<sub>3/2</sub>) and 794.7 eV (Co 2p<sub>1/2</sub>) appeared, corresponding to the energy position of Co<sub>3</sub>O<sub>4</sub> (Figure 5.9). For Co<sub>3</sub>O<sub>4</sub>/CNT@PDA, the intensity of the Co 2p peaks was nearly zero because the mean free path of the excited photoelectrons is shorter than the thickness of the PDA layer. This also suggests that all the nanoparticles and CNTs were completely embedded in the PDA layer. After annealing, both Co 2p<sub>3/2</sub> and Co 2p<sub>1/2</sub> peaks became visible again, owing to the shrinkage and transformation of the polymer film into a thin porous carbon shell enabling the excited photoelectrons to pass through. Moreover, the main spin orbit splitting components of Co 2p shifted towards higher binding energies and two shake-up satellite peaks became more pronounced, indicating that the oxidation phase of the nanoparticles has changed and a fraction of the material became CoO<sup>155–157</sup>.

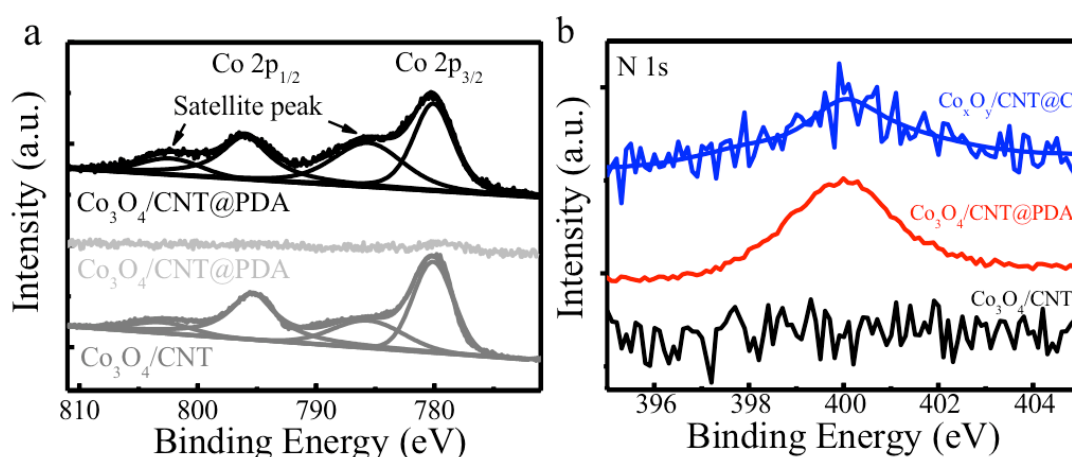


Figure 5.9. XPS spectra of Co<sub>3</sub>O<sub>4</sub>/CNTs, Co<sub>3</sub>O<sub>4</sub>/CNT@PDA and Co<sub>x</sub>O<sub>y</sub>/CNT@C (a) Co 2p and (b) N 1s.

To demonstrate the reduction of the nanoparticles during annealing, we performed in-situ experiments where samples were annealed and measured inside the XPS chamber, i.e. in ultra high vacuum conditions. As shown in Figure 5.10 a, Co 2p peaks were not observed until the sample was heated at 600 °C for 20 min. The shape and energy position of Co 2p core levels suggest that Co metal was already the dominant part at the surface of the nanoparticle. The spectrum of the sample without PDA coating showed the same tendency, but in this case we observed the intermediate CoO components after heating at 400 °C (Figure 5.11 a). These results

confirm that heating of  $\text{Co}_3\text{O}_4$  will release some oxygen from the oxide and convert it into  $\text{CoO}$ , and finally into  $\text{Co}$  metal, as also observed from XRD.

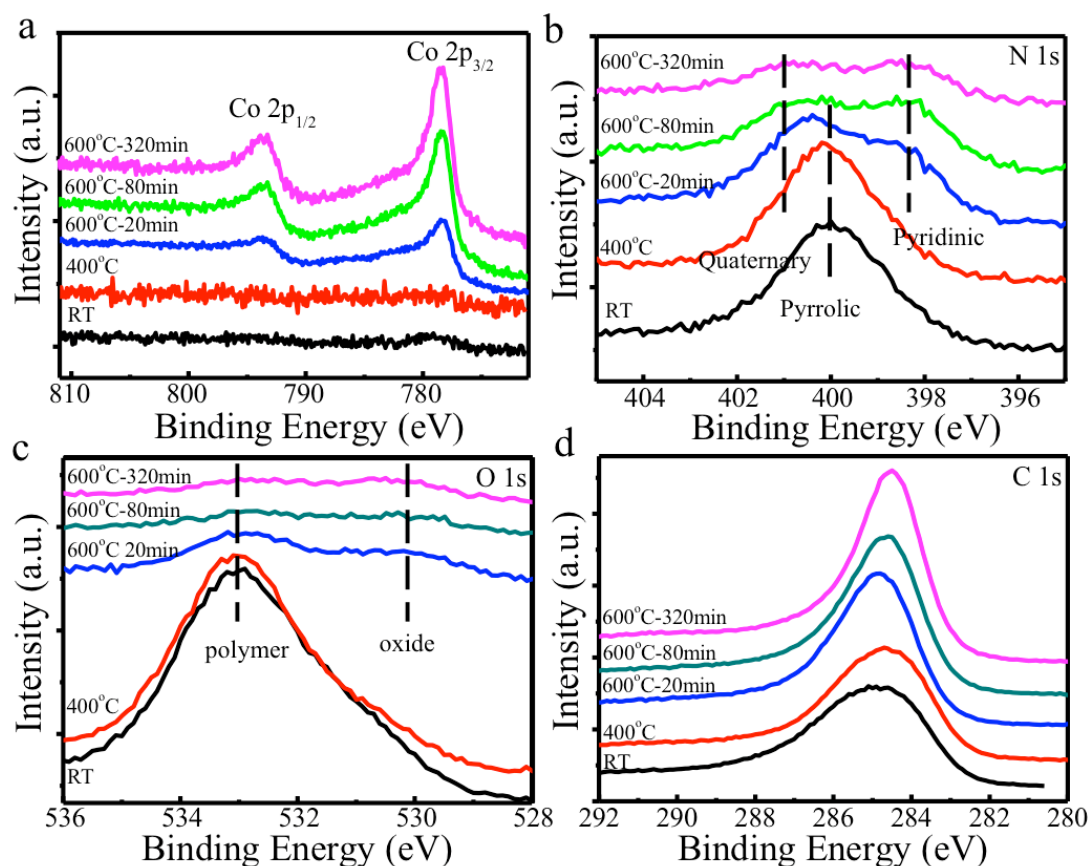


Figure 5.10. XPS spectra of in-situ annealed  $\text{Co}_3\text{O}_4/\text{CNTs}@PDA$  inside the XPS chamber upon different annealing stages: (a) Co 2p, (b) N 1s, (c) O 1s and (d) C 1s.

The evolution of the constituting elements of PDA N, O and C was also studied by in-situ XPS. Figure 5.10 b shows that the intensity of the N 1s peak kept decreasing during annealing. After annealing at 600 °C for 20 min the pyrrolic N started converting into pyridinic N and quaternary N. The O 1s peak initially showed high intensity at 533.2 eV corresponding to the O from PDA. During annealing the intensity decreased as the PDA kept releasing O and converting into carbon. Owing to the shrinkage of PDA, a new peak of O 1s at 530.4 eV occurred. This O stems from the cobalt oxide in the vicinity of the surface. Upon further annealing, the intensity of both O peaks decreased until they eventually vanished. The C 1s peak intensity steadily increased due to the formation of the carbon shell. Figures 5.11 b and c for

the sample without PDA coating show a similar decrease of the O 1s intensity as the  $\text{Co}_3\text{O}_4$  loses O during annealing. While for the C 1s peak in Figures 5.10 d and 5.11 c, the  $\text{Co}_3\text{O}_4/\text{CNT}@PDA$  sample shows some shifts as the PDA loses O and N which are initially bound to the C, the  $\text{Co}_3\text{O}_4/\text{CNT}$  doesn't show any changes in the position. Only a slight increase in the intensity is observed, which is due to more CNTs surface area being exposed after the nanoparticle agglomerations.

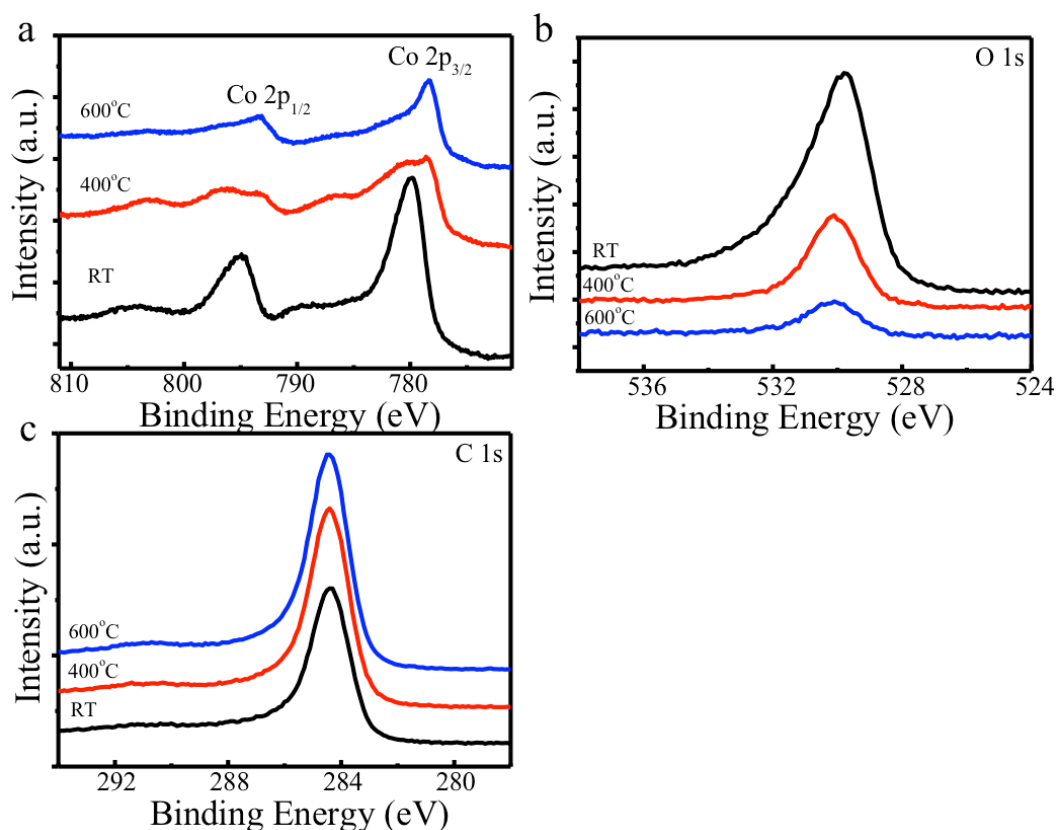


Figure 5.11. XPS spectra of in-situ annealed  $\text{Co}_3\text{O}_4/\text{CNTs}$  inside the XPS chamber upon different annealing stages: (a) Co 2p, (b) O 1s and (c) C 1s.

For characterizing the electro-catalytic ORR properties of the synthesized samples in  $\text{N}_2$ - or  $\text{O}_2$ -saturated 0.1 M KOH solution, cyclic voltammetry (CV) was applied. In Figures 5.12 a-c, all samples showed a quasi-rectangular double-layer capacity in  $\text{N}_2$ , and a well-defined ORR peak in presence of  $\text{O}_2$ . For  $\text{Co}_x\text{O}_y/\text{CNT}@C$ , the cathodic peak located at 0.77V was more positive than that of  $\text{Co}_x\text{O}_y/\text{CNT}$  (0.74V) and  $\text{CNT}@C$  (0.67 V), and also very close to the value of Pt/C (0.81 V). Besides, the peak current density also increased steadily, showing an improved catalytic activity of the fabricated samples.

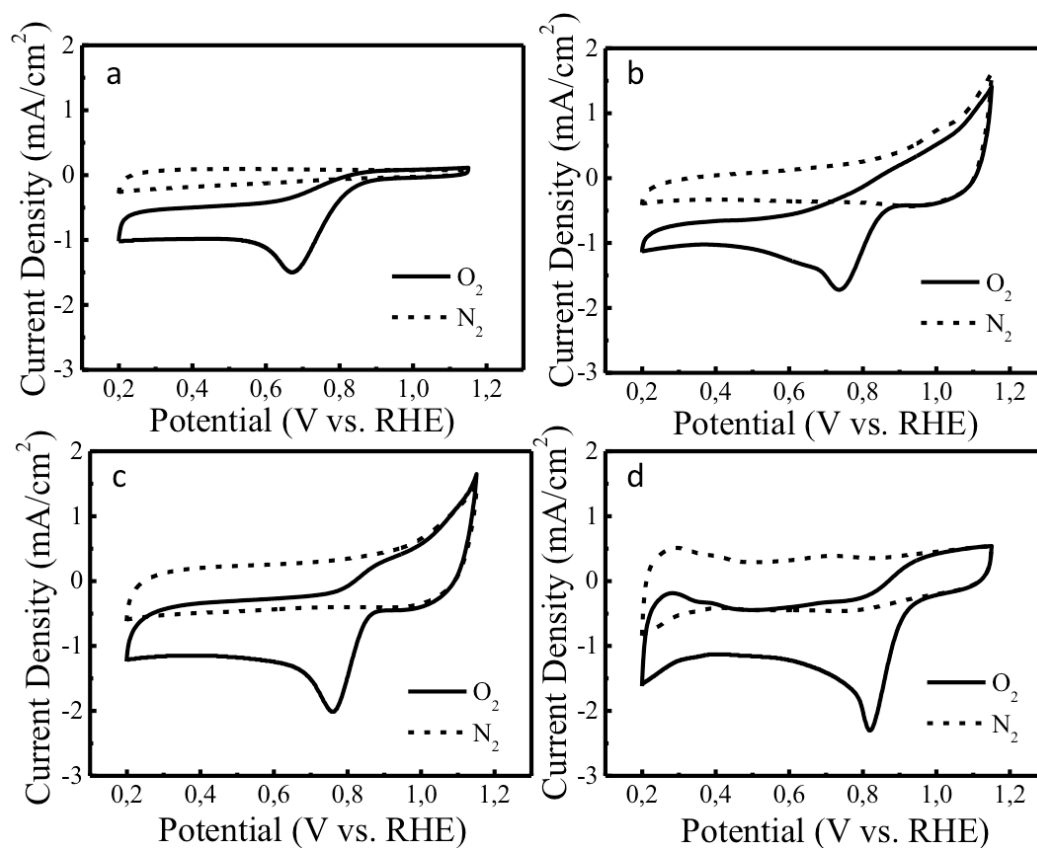


Figure 5.12. CV curves of (a) CNT@C, (b) Co<sub>x</sub>O<sub>y</sub>/CNT (c) Co<sub>x</sub>O<sub>y</sub>/CNT@C and (d) Pt/C samples on glassy carbon in O<sub>2</sub>-saturated (solid line) or N<sub>2</sub>-saturated (dashed line) 0.1 M KOH solution at a scanning rate of 50 mV/s.

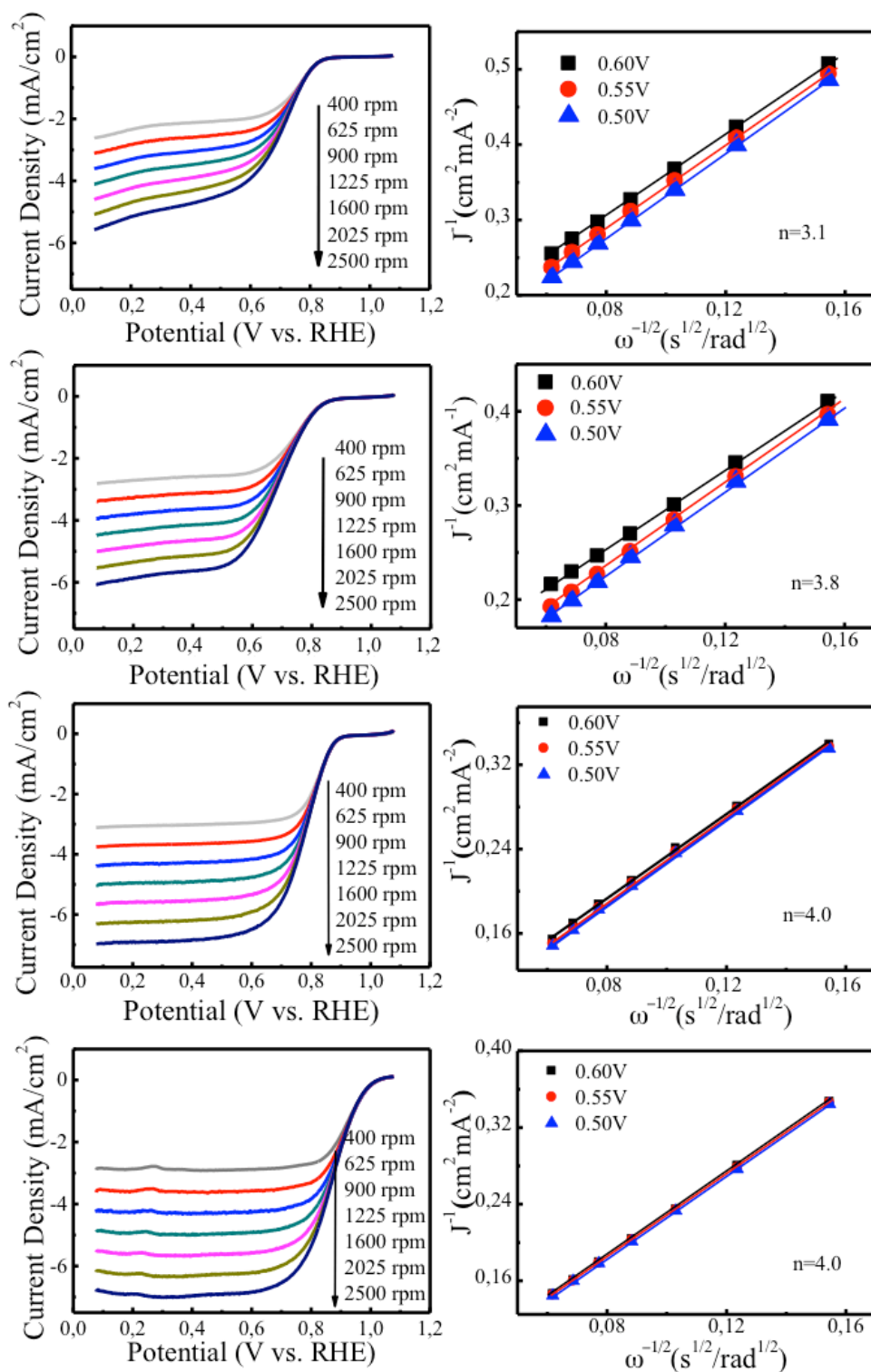


Figure 5.13. Rotating-disk voltammetric profiles of (a) CNT@C, (b)  $\text{Co}_x\text{O}_y/\text{CNT}$  (c)  $\text{Co}_x\text{O}_y/\text{CNT}@C$  and (d) Pt/C in  $\text{O}_2$ -saturated 0.1 M KOH with a sweep rate of 10 mV/s at various rotation rates ranging from 400 rpm to 2500 rpm. The figures in the right column show the corresponding Koutecky–Levich plots at different potentials of (e) CNT@C, (f)  $\text{Co}_x\text{O}_y/\text{CNT}$  (g)  $\text{Co}_x\text{O}_y/\text{CNT}@C$  and (h) Pt/C.

To study the ORR kinetics of the synthesized samples, Koutecky-Levich plots ( $J^{-1}$  vs.  $\omega^{-1/2}$ ) were derived from Rotation Disk Electrode (RDE) measurements at various potentials, as shown in Figure 5.13. The K-L plots show great linearity for all the samples, and the near parallelism of the fitting lines suggests two important points: i) clear first-order reaction kinetics with respect to the oxygen concentration and ii) similar electron transfer number for the ORR at various potentials. From the slopes we calculated the electron transfer numbers to be 3.1 and 3.8 for  $\text{Co}_x\text{O}_y/\text{CNT}$  and  $\text{CNT}@\text{C}$  (inset of Figure 5.13 e and f), and 4.0 for  $\text{Co}_x\text{O}_y/\text{CNT}@\text{C}$  (Figure 5.13 g). The latter value indicates an ideal reduction of  $\text{O}_2$  to  $\text{OH}^-$  instead of  $\text{HO}_2^-$ , which is also the case with the commercial Pt/C catalyst (Figure 5.13 h).

Figure 5.14 a shows that  $\text{Co}_x\text{O}_y/\text{CNT}@\text{C}$  has a more positive onset potential and higher cathodic current than  $\text{Co}_x\text{O}_y/\text{CNT}$  and  $\text{CNT}@\text{C}$ . For values below 0.6 V it is very similar to commercial Pt/C (20%). The Tafel slope of 58 mV/decade for  $\text{Co}_x\text{O}_y/\text{CNT}@\text{C}$  at a low over potential (Figure 3f) is much lower than that of  $\text{Co}_x\text{O}_y/\text{CNT}$  and  $\text{CNT}@\text{C}$ , further indicating excellent reactivity for ORR.

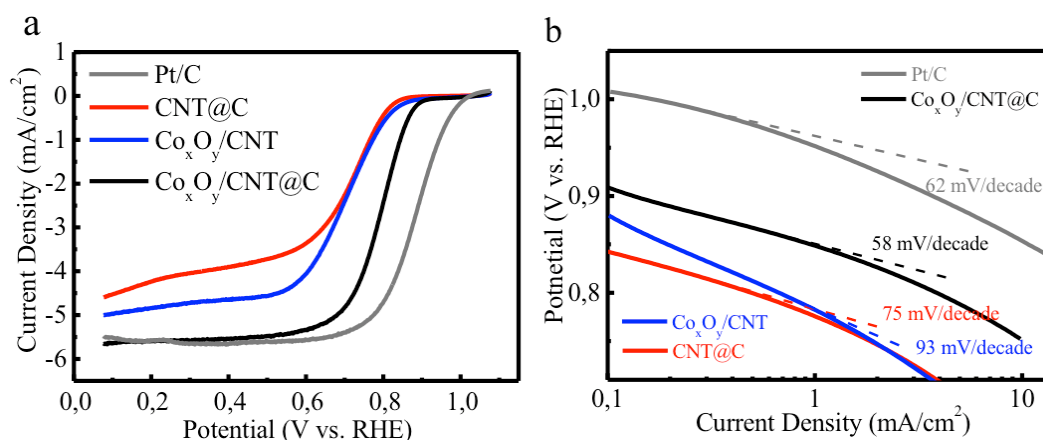


Figure 5.14. (a) Rotating-Disk Electrode LSV curves of  $\text{CNT}@\text{C}$ ,  $\text{Co}_x\text{O}_y/\text{CNT}$ ,  $\text{Co}_x\text{O}_y/\text{CNT}@\text{C}$  and Pt/C in  $\text{O}_2$ -saturated 0.1 M KOH with a sweep rate of 10 mV/s at 1600 rpm. (b) Tafel plots of  $\text{CNT}@\text{C}$ ,  $\text{Co}_x\text{O}_y/\text{CNT}$ ,  $\text{Co}_x\text{O}_y/\text{CNT}@\text{C}$  and Pt/C derived after the mass-transport correction of the corresponding RDE data.

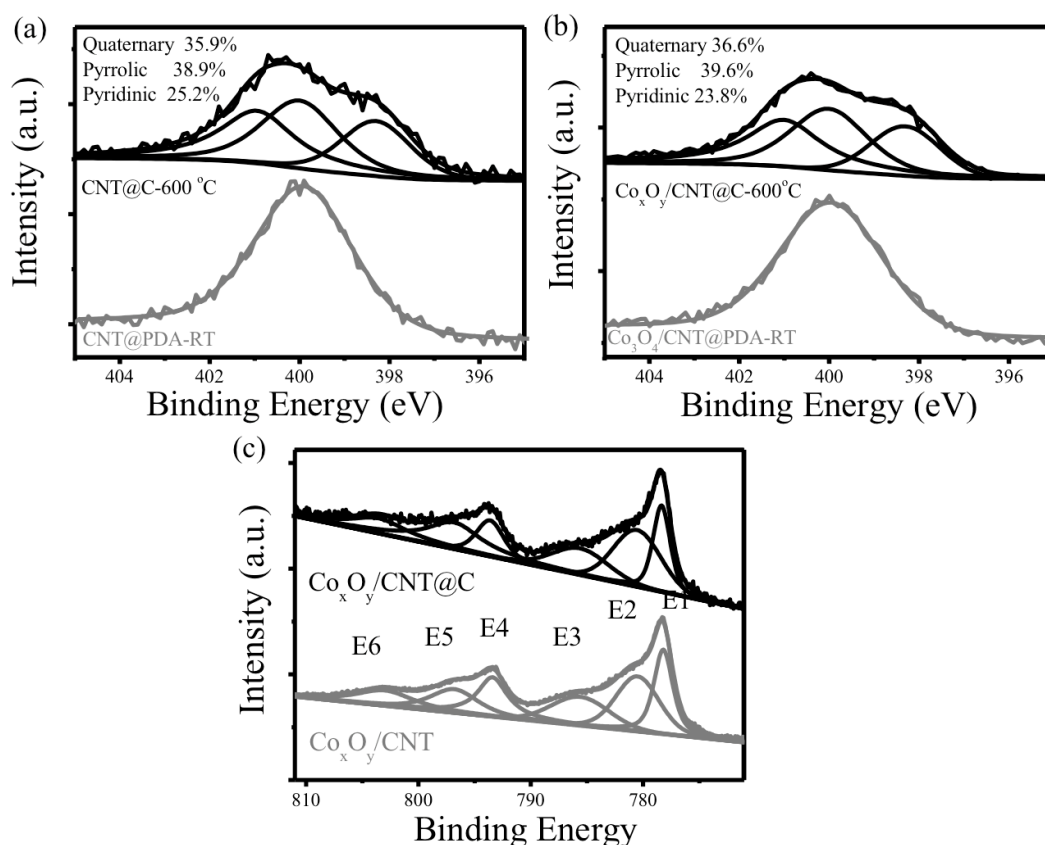


Figure 5.15. N 1s peak of (a) CNT@PDA (b) Co<sub>3</sub>O<sub>4</sub>/CNTs@PDA measured before and after annealing at 600 °C inside the XPS chamber. (c) Co 2p comparison of Co<sub>3</sub>O<sub>4</sub>/CNTs@PDA and CNT@PDA after annealing at 600 °C inside the XPS chamber. E1-E6 correspond to 2p<sub>3/2</sub> for Co metal, 2p<sub>3/2</sub> for Co-O, satellite of 2p<sub>3/2</sub> for Co-O, 2p<sub>1/2</sub> for Co metal, 2p<sub>1/2</sub> for Co-O and satellite of 2p<sub>1/2</sub> for Co-O, respectively.

The remaining question is related to the reason for the excellent reactivity of Co<sub>x</sub>O<sub>y</sub>/CNT@C. In some of the previously reported catalyst systems<sup>158–160</sup>, the formation of Co-N bonding was proposed to greatly contribute to the ORR catalytic reactivity. However when comparing the N 1s and Co 2p peaks of CNT@PDA and Co<sub>3</sub>O<sub>4</sub>/CNT@PDA during evolution (Figure 5.15), both samples behave similarly during various stages of annealing. This suggests that N and Co do not have serious impact on each other's evolution during annealing. No clear evidence for the existence of serious amounts of Co-N<sub>x</sub> can be seen. Therefore, the Co<sub>x</sub>O<sub>y</sub> nanoparticles are likely to still be the main active component for the ORR, even though embedded in the N-doped carbon shell<sup>161–163</sup>. Since the N-doped carbon shell is

obtained after the pyrolysis of the PDA, it will be thin and porous due to the loss of O and H, providing suitable pathways for molecular exchange.

The enhanced ORR activity may rely on two factors. Firstly, the N-doped carbon shell resulting from the PDA pyrolysis will on the one hand facilitate an easier electron transfer between the embedded  $\text{Co}_x\text{O}_y$  nanoparticles and the electrode during the catalytic process<sup>164,165</sup>; on the other hand it will to a small amount (Figure 5.13 a) also contribute to the overall reactivity as the carbon atoms in vicinity to pyridinic N were confirmed to be active sites for the ORR<sup>166</sup>. Secondly, the uniform distribution of the active  $\text{Co}_x\text{O}_y$  nanoparticles in both position and size assures the full utilization of the material for ORR, gaining more activity per mass. This uniformity is a direct result of atomic layer deposition, which deposits ideal  $\text{Co}_3\text{O}_4$  seeds, while the PDA hinders the  $\text{Co}_x\text{O}_y$  growth through Oswald ripening during the thermal annealing process (Figure 5.5). Comparing to previous work on similar material systems (Table 5.1), our composite shows the highest current density and lowest Tafel slope, indicating a successful approach towards improved ORR catalysts.

The number of applied ALD cycles and the annealing temperature may play a role for the performance of the catalyst, and therefore were also investigated. Upon comparing samples fabricated with 100, 300 and 500 ALD cycles, the 300-cycle sample showed the highest current intensity (Figure 5.16 a). The lower number of ALD cycles (100) obviously resulted in too low amounts of active  $\text{Co}_x\text{O}_y$ , while the density of deposited  $\text{Co}_3\text{O}_4$  was too high after 500 applied ALD cycles (Figure 5.4), resulting in larger nanoparticles after annealing, which decreases the reactivity. The annealing temperature had a similar effect on the size of the  $\text{Co}_x\text{O}_y$  nanoparticles. After annealing at 800 °C,  $\text{Co}_x\text{O}_y/\text{CNT}@C$  showed lower current densities in comparison to the samples annealed at 600 °C (Figure 5.17). The higher temperature enhanced the mobility of the nanoparticles and induced merging into larger particles as a result of Ostwald ripening (Figure 5.17 d). The density and size of the nanoparticles here greatly affect the ORR catalytic activity, which also indicates that the cobalt oxide nanoparticles are the main active component for ORR.

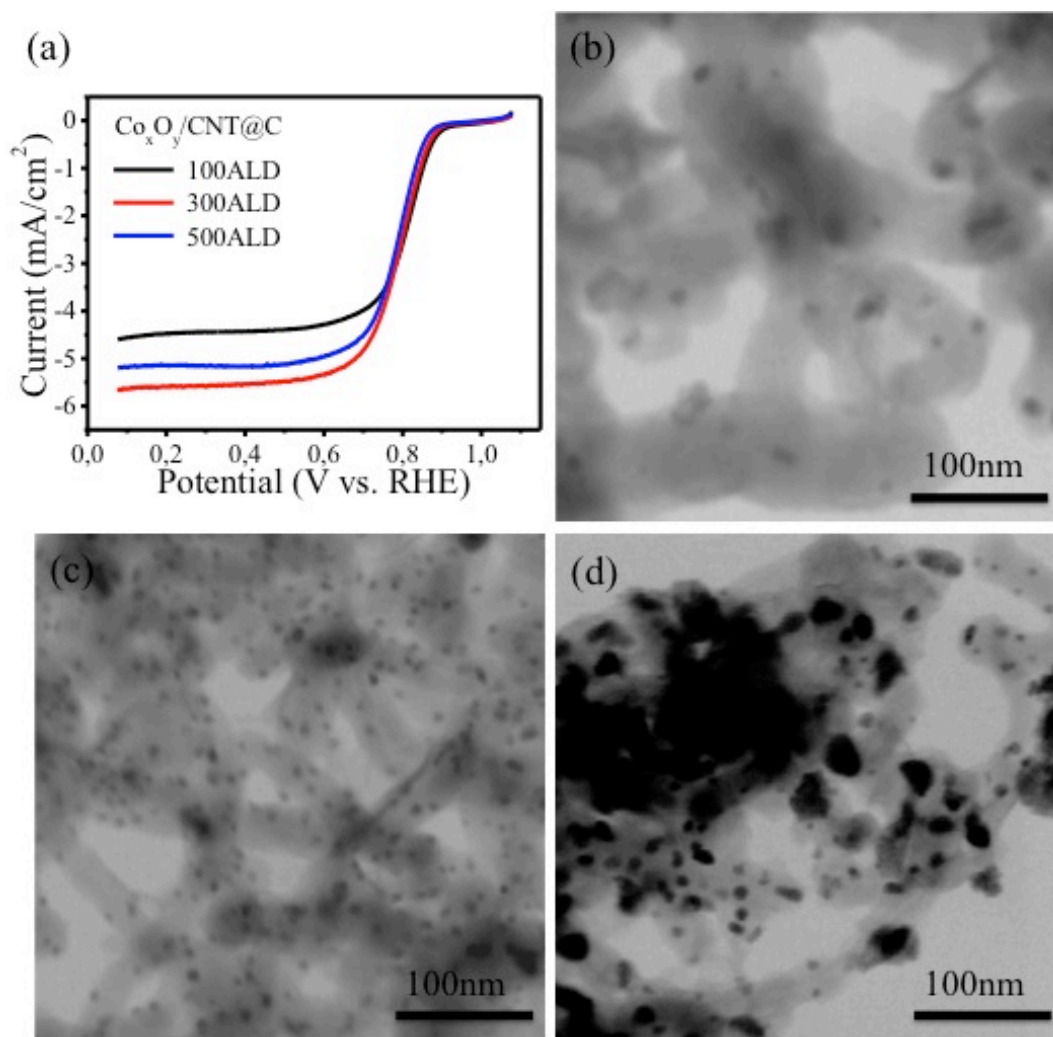


Figure 5.16. (a) Rotating-Disk Electrode LSV curves of  $\text{Co}_x\text{O}_y/\text{CNT}@C$  with various applied ALD cycles in  $\text{O}_2$ -saturated 0.1M KOH solution with a sweep rate of 10 mV/s at 1600 rpm. STEM images of  $\text{Co}_x\text{O}_y/\text{CNT}@C$  with various applied ALD cycles (b) 100 cycles, (c) 300 cycles, (d) 500 cycles.

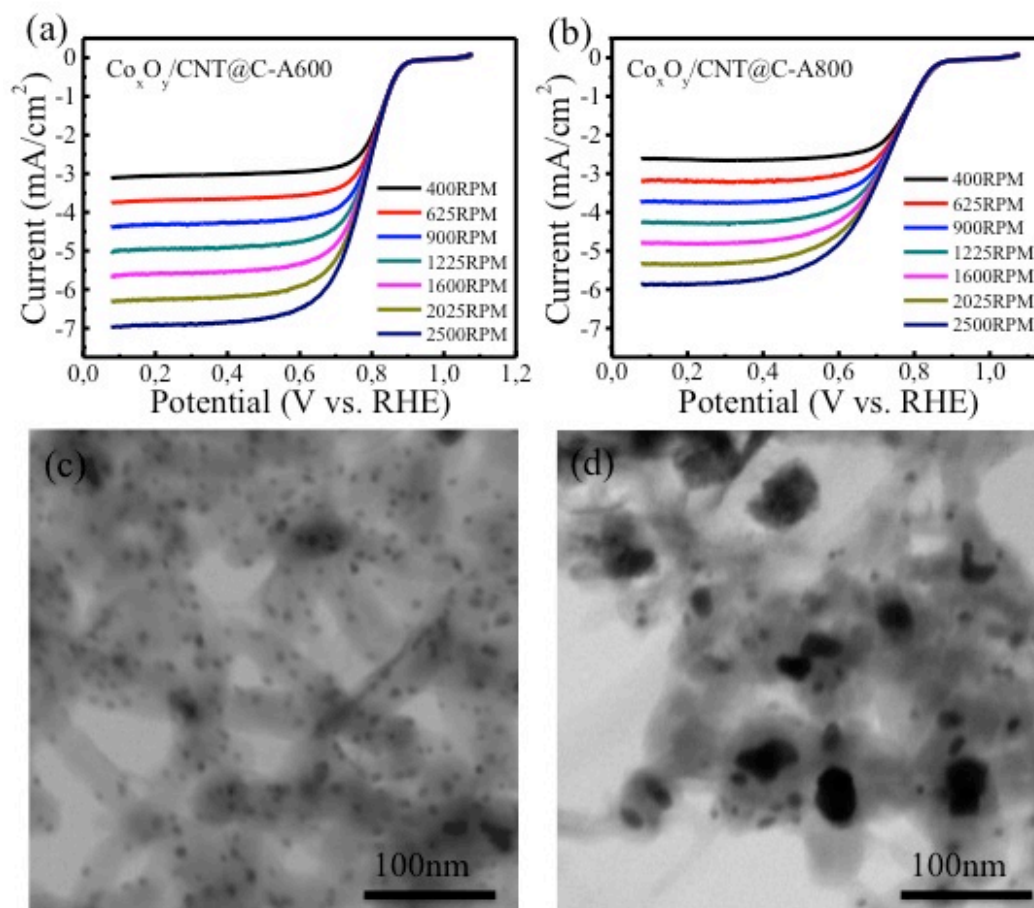


Figure 5.17. Rotating-Disk Electrode LSV curves of Co<sub>x</sub>O<sub>y</sub>/CNT@C annealed at various temperatures (a) 600 °C, (b) 800 °C in O<sub>2</sub>-saturated 0.1M KOH with a sweep rate of 10 mV/s at 1600 rpm. STEM images of Co<sub>x</sub>O<sub>y</sub>/CNT@C annealed at various temperatures (c) 600 °C, (d) 800 °C.

The stability/durability of the ORR catalyst is a further key issue besides the activity. It is commonly accepted that the instability of an ORR catalyst often originates from the agglomeration of the active nanoparticles (see commercial Pt/C before and after cycling in Figure 5.18 e and f), or leaching of active materials from the support (see Co<sub>x</sub>O<sub>y</sub>/CNT before and after cycling in Figure 5.18 c and d). However, thanks to the PDA coating and the resulting embedding of the particles, the nano-architecture of Co<sub>x</sub>O<sub>y</sub>/CNT@C, including the size and density of the Co<sub>x</sub>O<sub>y</sub> particles, was perfectly maintained even after 10.000 electrochemical testing cycles (Figure 5.18 a and b). Upon functional testing of the Co<sub>x</sub>O<sub>y</sub>/CNT@C sample, this is further reflected in the exceptional durability over extended CV cycling periods as well as the high stability, maintaining great performance at constant potential

conditions, as clearly observed in Figure 5.19. The tests were carried out in O<sub>2</sub>-saturated 0.1 M KOH for 10.000 cycles. The half wave potential for Co<sub>x</sub>O<sub>y</sub>/CNT@C negatively shifted by 10 mV after 5.000 cycles towards 21 mV after 10.000 cycles (Figure 5.19 a), which is considerably lower than the values obtained from the commercial Pt/C sample, namely 50 mV and 63 mV, respectively (Figure 5.19 b). Furthermore, the Co<sub>x</sub>O<sub>y</sub>/CNT@C catalyst lost only about 14% of its initial electrochemical surface area (ECSA) after 10.000 test cycles, while the ECSA of Pt/C decreased by 65% after the same number of cycles (Figure 5.19 c). The stability of the Co<sub>x</sub>O<sub>y</sub>/CNT@C catalyst was further characterized by chronoamperometry. Figure 5d shows that after 10.0000 s the current was still at 83% of the initial value, corresponding to a loss of only 17%. Note that the Pt/C reference sample showed a loss of 35% in identical conditions.

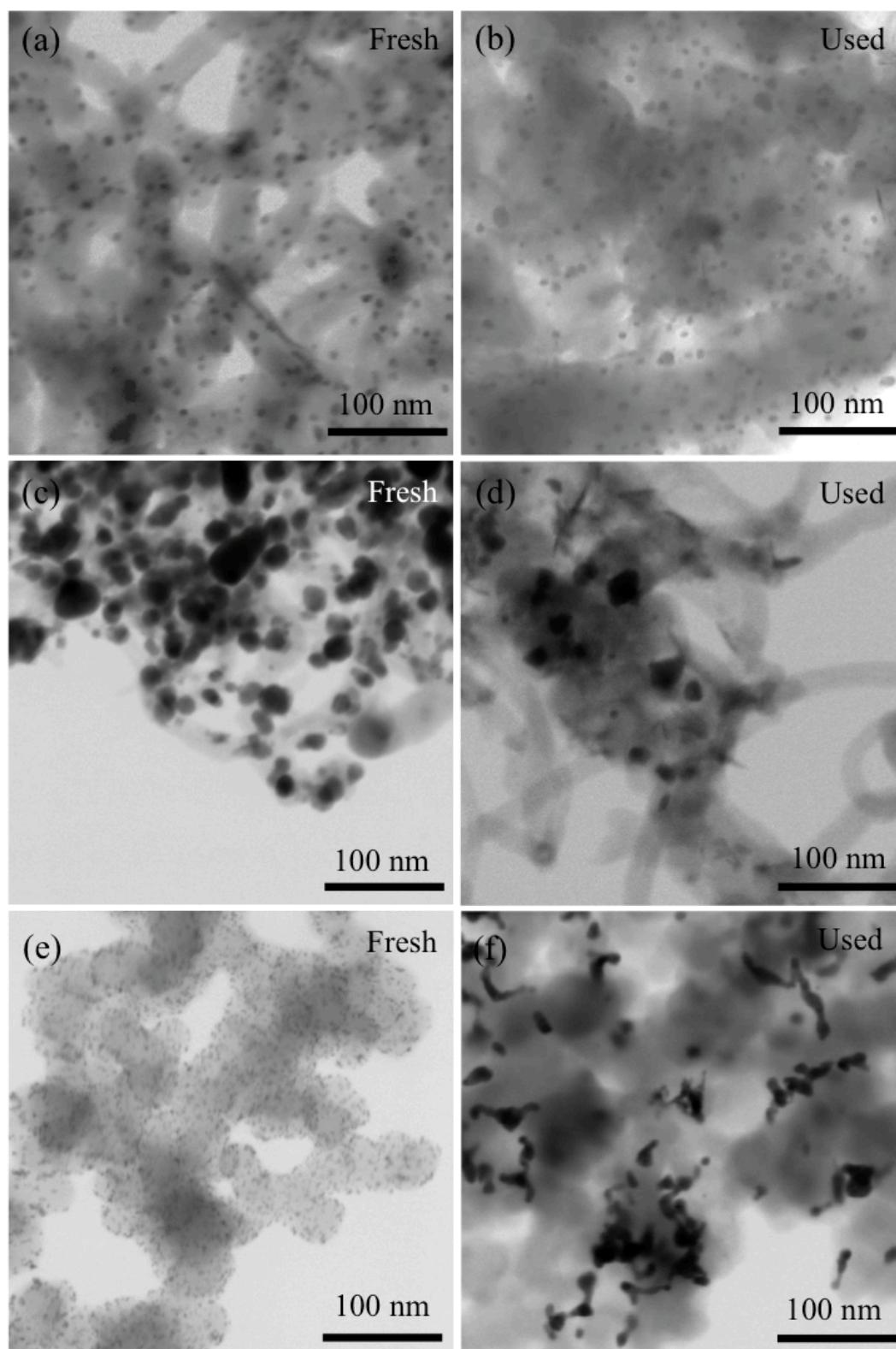


Figure 5.18. STEM images of  $\text{Co}_x\text{O}_y/\text{CNT}@C$  (a) as synthesized, (b) after 10.000 testing cycles, and  $\text{Co}_x\text{O}_y/\text{CNT}$  (c) as synthesized, (d) after 10.000 testing cycles;  $\text{Pt}/C$  (e) initial, (f) after 10.000 testing cycles.

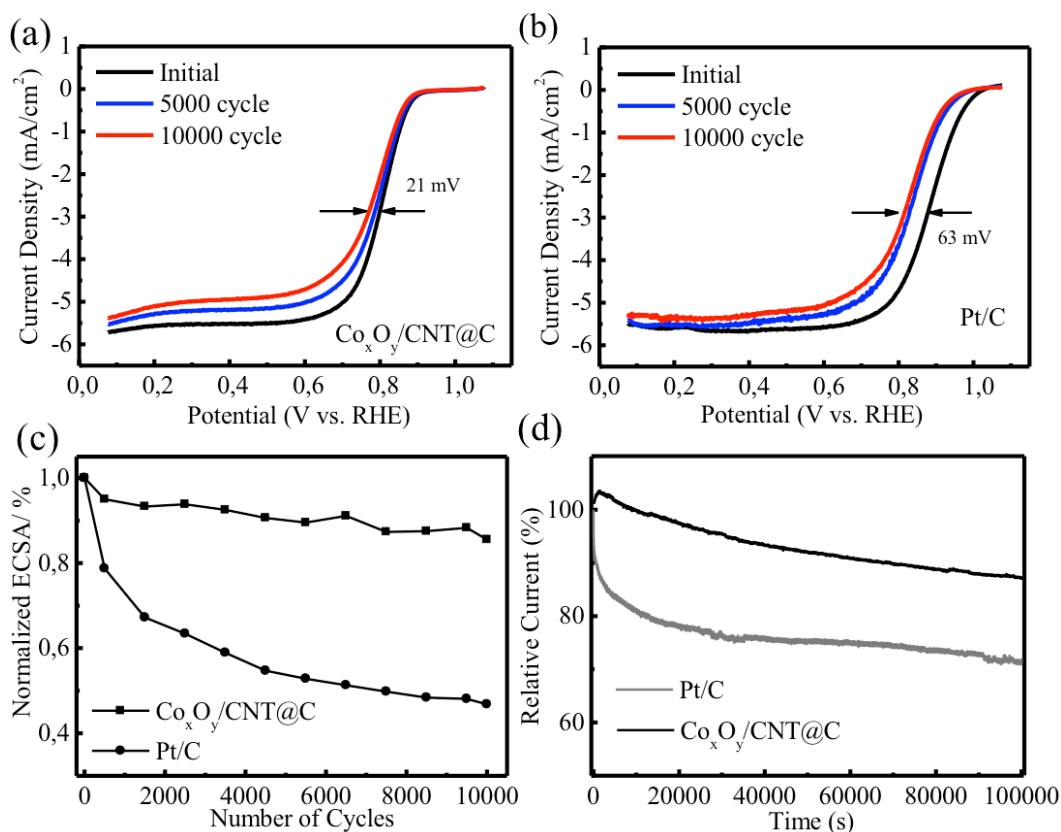


Figure 5.19. ORR curves of (a)  $\text{Co}_x\text{O}_y/\text{CNT}@C$  and (b) Pt/C samples in  $\text{O}_2$ -saturated 0.1 M KOH solution with a sweep rate of 10 mV/s at 1600 rpm. (c) Loss of electrochemical surface area (ECSA) of  $\text{Co}_x\text{O}_y/\text{CNT}@C$  and Pt/C catalysts as a function of cycling numbers of electrochemical tests. (d) Current-time chronoamperometric responses of  $\text{Co}_x\text{O}_y/\text{CNT}@C$  and Pt/C at 0.65 V (vs RHE.) in  $\text{O}_2$ -saturated 0.1 M KOH.

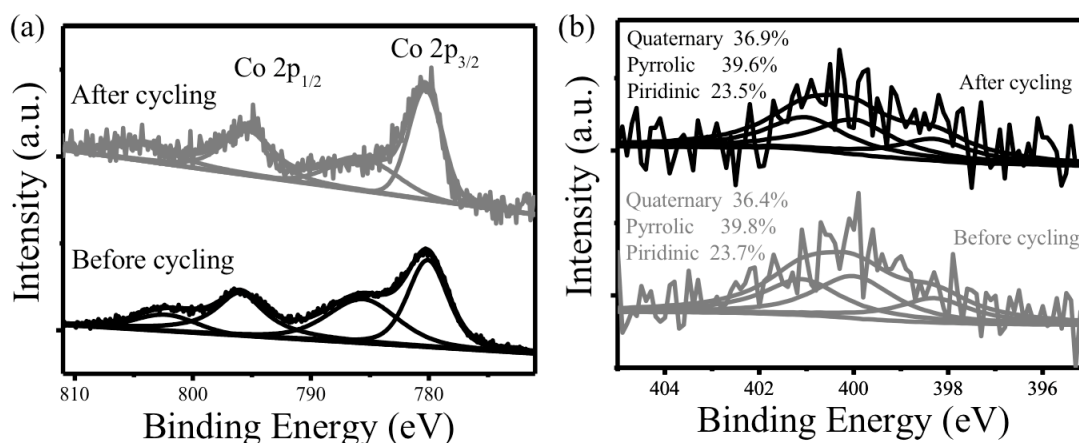


Figure 5.20. XPS spectra of  $\text{Co}_x\text{O}_y/\text{CNT}@C$  before and after 10,000 electrochemical testing cycles, (a) Co 2p and (b) N 1s.

We conclude that this outstanding stability/durability might be related to the embedding of the nanoparticles into the coating during the composite formation. The pyrolysis-derived carbon shell not only prevented the nanoparticles from detaching off of the CNT but also minimized the mobility of the nanoparticles as can be seen in Figures 5.16 a and b. While in Figure 5.18, the XPS spectra for both Co 2p and N 1s of the  $\text{Co}_x\text{O}_y/\text{CNT}@C$  sample show no obvious changes before and after the cycling tests. Therefore the architecture of the  $\text{Co}_x\text{O}_y/\text{CNT}@C$  is greatly preserved as well as the electronic states of the materials due to the embedding concept, which is resulting in an exceptional stability/durability. Comparing to further work with similar material systems (Table 5.1), the  $\text{Co}_x\text{O}_y/\text{CNT}@C$  materials system is among the most stable/durable for the longest testing durations, showing that the particle growth and the intended coating of N-doped carbon shell is a true benefit for maintaining the reactivity of the catalyst over long-term operation.

Table 5.1 Comparison of electrocatalytic activity and stability/durability of embedded cobalt oxide based catalysts for ORR in alkaline media.

| Catalyst                              | Co <sub>x</sub> O <sub>y</sub> /CNT@NC                      | Co@Co <sub>3</sub> O <sub>4</sub> /NC                | CoP-CMP                                | Co@Co-N-C                                 |                                    |
|---------------------------------------|---|--|--|---|------------------------------------|
| Loading density (mg/cm <sup>2</sup> ) | 0.2   | 0.21   | 0.6                                    | 0.6                                       |                                    |
| Reactivity                            | Half-wave potential vs. RHE from 1600 rpm LSV               | 0.80 V<br>70 mV negative than Pt/C                   | 10 mV negative than Pt/C               | 0.879 V<br>2 mV negative than Pt/C        | 0.83 V<br>70 mV negative than Pt/C |
|                                       | Cathodic current density at 0.5 V vs. RHE from 1600 rpm LSV | ~ 5.4 mA/cm <sup>2</sup>                             | < 5 mA/cm <sup>2</sup>                 | < 5 mA/cm <sup>2</sup>                    | < 5 mA/cm <sup>2</sup>             |
|                                       | Tafel slope in low over potential region                    | 58 mV/decade   | NA                                     | 59 mV/decade                              | NA                                 |
| Stability                             | ECSA retention over cycling test                            | 86% after 10.000 cycles                              | 96.7% after 1000 cycles                | NA  | NA                                 |
|                                       | Half-wave potential shift over cycling test                 | 10 mV after 5000 cycles,<br>21 mV after 10000 cycles | NA                                     | 17 mV after 2000 cycles                   | NA                                 |
|                                       | Chrono-amperometric test at 1600 RPM                        | 0.65 V vs RHE<br>17% loss after 10.0000s test        | NA                                     | -0.3V vs. RHE<br>10% loss after 20000s    | NA                                 |
| Reference                             | <b>This work</b>  | <b>Angew. Chem. Int. Ed.</b> 2016, 55, 4087-4091     | <b>Adv. Mater.</b> 2014, 26, 1450–1455 | <b>Chem. Commun.</b> 2015, 51, 8942--8945 |                                    |

| Catalyst                              | Co@Co <sub>3</sub> O <sub>4</sub> /BNC NTs                  | Co/CoO/CoFe <sub>2</sub> O <sub>4</sub> /G         | Co/N/C  | Co10-NMCV                                     |  |
|---------------------------------------|---|--|---|---|--|
| Loading density (mg/cm <sup>2</sup> ) | ~ 0.7   | 0.28   | 0.458   | 0.15  |  |
| Reactivity                            | Half-wave potential vs. RHE from 1600 rpm LSV               | 50 mV negative than Pt/C                           | NA  | 0.80 V<br>25 mV negative than Pt/C            | 20 mV negative than Pt/C                       |
|                                       | Cathodic current density at 0.5 V vs. RHE from 1600 rpm LSV | < 4 mA/cm <sup>2</sup>                             | < 5 mA/cm <sup>2</sup>                        | ~ 4.5 mA/cm <sup>2</sup>                      | ~ 4 mA/cm <sup>2</sup>                         |
|                                       | Tafel slope in low over potential region                    | NA   | 83 mV/decade                                  | NA  | 59.64 mV/decade                                |
| Stability                             | ECSA retention over cycling test                            | NA   | NA  | NA  | NA   |
|                                       | Half-wave potential shift over cycling test                 | NA   | NA  | NA  | E <sub>onset</sub> shift 24 mV for 6000 cycles |
|                                       | Chrono-amperometric test at 1600 RPM                        | -0.2 V vs. Ag/AgCl<br>20% loss after 20 000 s test | -0.40 V vs. Hg/HgO<br>19.4% loss over 20000 s | NA  | -0.35 V vs. Ag/AgCl ~ 15% after 20000s         |
| Reference                             | <b>Nanoscale.</b> 2015, 7,7056-64                           | <b>Nanoscale.</b> 2014, 6, 203-206                 | <b>Sci. Rep.</b> 2014, 4, 4386                | <b>J. Mater. Chem. A</b> 2014, 2, 11672–11682 |  |

## 5.4 Conclusions

In this chapter, we have demonstrated a very elegant method to fabricate highly dispersed  $\text{Co}_x\text{O}_y$  nanoparticles embedded in a carbon matrix, which as final composite acts as very efficient and cost effective non-noble metal catalyst for the ORR reaction. Nanoparticles of  $\text{Co}_x\text{O}_y$  are grown on defect sites of CNTs by ALD in a very controlled size distribution and a doped carbon shell is obtained after subsequent coating with PDA and its pyrolysis. This formed carbon film has proven to be an effective way to prevent agglomeration and leaching of the nanoparticles while at the same time having a positive impact on the reactivity of the composite for the ORR. Moreover, it is likely that such a conductive coating is supportive for the catalytic reaction through enhancing the electron transfer rate. Owing to this unique architecture, the synthesized samples show much higher stability and durability than the commonly applied commercial Pt/C catalyst, offering a great opportunity to substitute noble metal catalysts in emerging energy-related applications. This proposed design is not specific for the described problem, but can be easily extended to the synthesis of further catalysts and sensors or other functional materials.

---

## Chapter 6

# Interactions between ALD Precursor and Functional Groups

The previous chapter describes the functionality of defect sites of a substrate by ALD. Those defect sites were, however, linked to oxidized sites of graphene. In order to broaden the spectrum of possible functionalization strategies, substrates with further functional groups may be applicable. However, not much is known about the chemical interactions of typical ALD precursors with chemical functionalities beyond alcohols or carboxylic acids. This chapter reports the fundamental investigation of the interactions between ALD precursors and functional groups of various types. The reaction of TMA with functional groups like amine, nitro and hydroxyl, as well as the stability of the intermediate upon exposure to humidity are presented. This investigation aims at improving our understanding on the mechanisms of ALD and related infiltration processes at the molecular level, which will guide us towards better control of organic-inorganic hybrid materials growth by ALD (or MLD) or target tuning/modification of soft materials by infiltrations.

### 6.1 Introduction

Organic-inorganic hybrid materials are of great interest for material scientists, which combine advantages from both involved inorganic and organic components. Often they bring about new innovational aspects for practical use<sup>167</sup>. ALD processing allows two ways for producing such hybrid materials: MLD<sup>48-50</sup> and vapor phase infiltration<sup>168</sup>. In MLD, the process is similar to ALD, however at least one of the precursors is substituted with an organic molecule. Various hybrid materials including zircones<sup>55-59</sup>, alucones<sup>60-62</sup>, titanicones<sup>63-65</sup>, and many others<sup>169,170</sup> were grown by MLD. Those often exhibit interesting chemical or physical properties, which deviate from their corresponding oxides.

Vapor phase infiltration is another way to develop organic-inorganic hybrid materials using the ALD processing technology. In an infiltration process, typical ALD metal precursors are pulsed into the reactor and allowed to diffuse into the substrate (often natural or synthetic polymers) during an extended period of time. The precursor will penetrate the materials and interact with the functional groups in the subsurface area<sup>70,72-76</sup>. Vapor phase infiltration can be used for designing and synthesizing new metal-organic materials from technical polymers to individual molecules. A prominent example for the latter case is the metalation of porphyrins via infiltration of DEZ by Zhang et al<sup>70</sup>. On a large scale, the incorporated metal might have a high impact on the properties of the substrate. It has been shown that the strength and toughness of the dragline spider silk have been greatly enhanced after being processed by vapor phase infiltration<sup>72</sup>.

Both MLD and infiltration have been broadly studied and showed great advantages for the hybrid material synthesis or soft material modification. However, the mechanism underneath, which is, the interactions between the metal precursor and the organic functional groups in either MLD or infiltration, are still lacking detailed understanding. Therefore, we performed fundamental investigations on the interactions between the trimethylaluminum (TMA) precursor and some common organic functional groups (amine, nitro and hydroxyl group). Those functional groups are chosen for their different electronic character and should act as representatives for various classes of organic molecules or polymers. In a combined experimental and theoretical approach, we show that the TMA will firstly bind to specific sites of the functional groups, while an additional energy barrier needs to be overcome for strengthening the chemical bonding between TMA and those functional groups. Depending on the activation energy, the final state between TMA and the functional groups show either strong chemical bindings or weak and unstable interactions. These findings are a first step towards understanding and controlling the MLD and infiltration processes at the molecular level, and may help us to optimize hybrid material fabrication in future.

## 6.2 Experiments

4-Hydroquinone, 4-phenylenediamine, 4-dinitrobenzene, 4-nitrophenol, 4-aminophenol and 4-nitroaniline were purchased from Sigma-Aldrich. The chemicals were of analytic grade, and were used as received unless otherwise stated.

### Experiments with Savannah 100

The chemicals were dissolved in ethanol and drop casted onto cleaned glass slides. The glass slide was placed in the reactor of a Savannah 100 (Cambridge Nanotech) at around 80 °C. TMA was pulsed into the chamber and allowed to react with the sample. The pulse, exposure and purge times were 0.015 s, 90 s and 90 s, respectively.

### Semi-in situ ALD/XPS

In order to avoid contamination from air and humidity, dosing of TMA to the molecules was performed inside a load-lock connected with the XPS chamber. First, the chemicals were pressed into pellets and placed into the load-lock; then TMA was introduced to enable the reaction; subsequent purging with high purity nitrogen were performed and the samples were directly transferred into the ultra high vacuum (UHV) chamber for the XPS measurement. After the measurement, the samples were transferred back into the load-lock and exposed to air for testing the stability of the interaction between TMA and molecules, then purged and transferred back into the UHV chamber and measured again. Thus, each sample was measured three times, prior to TMA dosing, after TMA dosing and after exposure to air.

In the same set-up, a MLD type of material growth using TMA and 4-phenylenediamine on a rutile (110) TiO<sub>2</sub> substrate was also investigated. For this purpose, initially TMA was dosed to bind to the TiO<sub>2</sub> surface in the load-lock. After purging with N<sub>2</sub>, the TiO<sub>2</sub> sample was transferred into the UHV chamber and measured with XPS. In the next stage, the TiO<sub>2</sub> was transferred back into the load-lock and dosed with 4-phenylenediamine. After purging, the TiO<sub>2</sub> was transferred again into the UHV chamber and measured with XPS. The stability of the interaction between 4-phenylenediamine and TMA was finally tested by dosing H<sub>2</sub>O into the load-lock and measured in the UHV chamber again. The reverse dosing sequence

with first 4-phenylenediamine, second TMA and finally with H<sub>2</sub>O were also performed and measured. Therefore, each TiO<sub>2</sub> sample was measured four times with a clean TiO<sub>2</sub> surface, after 4-phenylenediamine (or TMA) dosing, after TMA (or 4-phenylenediamine) dosing and after water dosing.

The XPS experiments were performed using a Phoibos photoelectron spectrometer equipped with an Al K $\alpha$  X-ray source as the incident photon radiation. For the pellet samples, the C 1s spectra exhibit main features between 285.0-286.0 eV for different chemicals, which were used to calibrate the positions of all other peaks based on reported data<sup>171-173</sup>. For the surface samples, the Ti 2p peak was used for the binding energy calibration. The overall resolution of the instrument is approximately 0.9 eV. At this resolution, the line energy positions could be determined with an accuracy of  $\pm 0.2$  eV. The pressure in the analyzing chamber was  $< 1.0 \times 10^{-9}$  mbar for all measurements.

## UV-vis Spectroscopy

ALD infiltrated samples were dissolved in water or toluene and measured with a Nanodrop 2000 for obtaining the UV-Vis adsorption spectroscopy.

## Computational Simulation

All calculations were carried out with the Perdew–Burke–Ernzerhof (PBE) exchange-correlation functional<sup>174</sup> and the SV(P) (double zeta valence basis set with polarization at all non-Hydrogen atoms) basis set as implemented in TURBOMOLE<sup>175</sup> with the RI approximation for Coulomb integrals<sup>176</sup> accompanied by the corresponding auxiliary basis sets.<sup>177</sup> Geometries were freely optimized using redundant internal coordinates<sup>178</sup> until gradients were  $< 10^{-6}$  Hartree. Optimized structures were visualized with Materials Studio suite version 7.0.

This theoretical part of the work was performed by the group of Dr. Simon Elliott at the Tyndall National Institute in Cork, Ireland.

## 6.3 Results and Discussion

The interactions between TMA and various functional groups (amine, nitro and hydroxyl group) were studied by selecting a set of molecules that are composed

of a phenyl ring and various substituents. Six molecules with various combinations of the three functionalities, 4-hydroquinone, 4-phenylenediamine, 4-dinitrobenzene, 4-nitrophenol, 4-aminophenol and 4-nitroaniline, were used for the experiments. The molecules were pressed into a pellet, and dosed with TMA in a load-lock. This procedure allowed direct measurements of the chemical states by XPS without exposure to air. In this way, the interaction state between TMA and these functional groups are well preserved, and even metastable states could be identified.

## Interaction between TMA and $-\text{NH}_2$

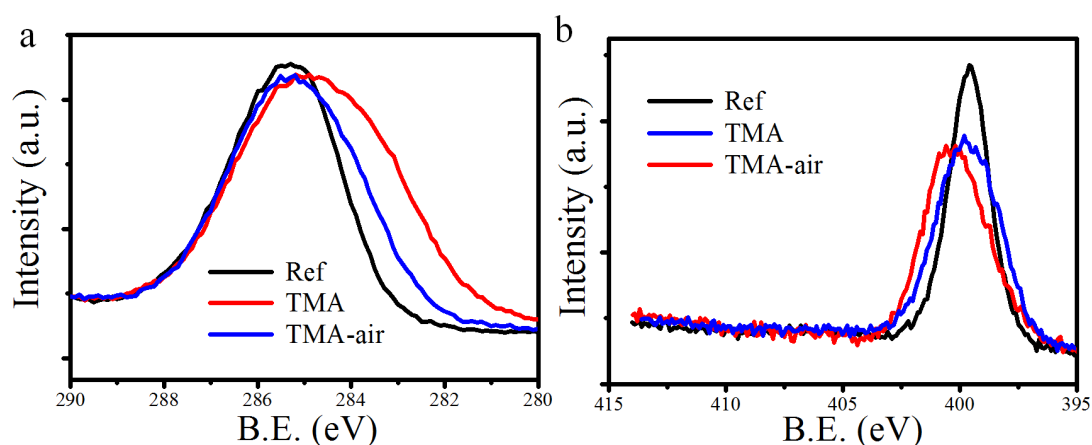


Figure 6.1. (a) C 1s and (b) N 1s XPS spectra of 4-phenylenediamine in the native, TMA dosed and air exposed states.

4-phenylenediamine (4-PD) was chosen for studying the interaction between  $-\text{NH}_2$  and TMA. Figure 6.1 shows the C 1s and N 1s spectra of 4-phenylenediamine in its native state, after TMA dosing and further exposure to air ( $\text{H}_2\text{O}$ ). In Figure 6.1 (a), the reference C 1s core level of 4-PD has a symmetric shape originating from the carbon atoms of the phenyl ring. Upon TMA dosing, the C 1s spectrum becomes asymmetric and broader, with a shoulder in the lower binding energy region. This matches well the signal of TMA as identified in former XPS measurements<sup>179–181</sup>. Obviously, TMA initially interacts with the 4-PD, but after exposure to air ( $\text{H}_2\text{O}$ ) the shoulder in the low binding energy region of the C 1s peak in Figure 6.1 (a) decreases. Exposure of the sample to air will cause TMA reacting with water similar to the TMA/ $\text{H}_2\text{O}$  ALD process for alumina growth. The spectrum also shows that the C 1s core level does not recover to its original state of the 4-PD. The reason for this is

most likely the ability of TMA to infiltrate the pellet sample, and reside in the bulk with some unreacted methyl groups owing to steric protection from the environment.

The N 1s core level shifts from its original state to a higher binding energy region after TMA dosing, indicating a higher oxidation state of the N in  $-\text{NH}_2$ . The core levels of Al 2s and Al 2p for the TMA dosed sample in Figure 6.2 located below 73.5 eV and 118.5 eV, respectively, are at lower binding energies compared with those for TMA<sup>179–181</sup>. These changes of the N and Al core levels suggest that there exists an electronic interaction between the N and Al atoms. After exposing the sample to air, however, the Al 2s and 2p core levels shift towards higher binding energies, suggesting the formation of an Al-O bond owing to the reaction between TMA and  $\text{H}_2\text{O}$  from air. This is consistent with the C 1s shift after the exposure to air in Figure 6.1 (a). In Figure 6.1 (b), the N 1s peak also recovers to the initial position of 4-PD but becomes somewhat broader, which is probably owing to the trapped TMA that is adsorbed to the  $-\text{NH}_2$ . Another possibility can be related to the intermolecular effect. It is reported that the intermolecular effect plays important role for the shape of the N 1s peak, where the shape varies for solid and gas phase samples<sup>182,183</sup>. The formation of  $\text{Al}_2\text{O}_3$  after exposure to air probably has similar effects for the N 1s peak here. In general, these changes show that the interaction between  $-\text{NH}_2$  and TMA is not stable upon contact with humidity from air.

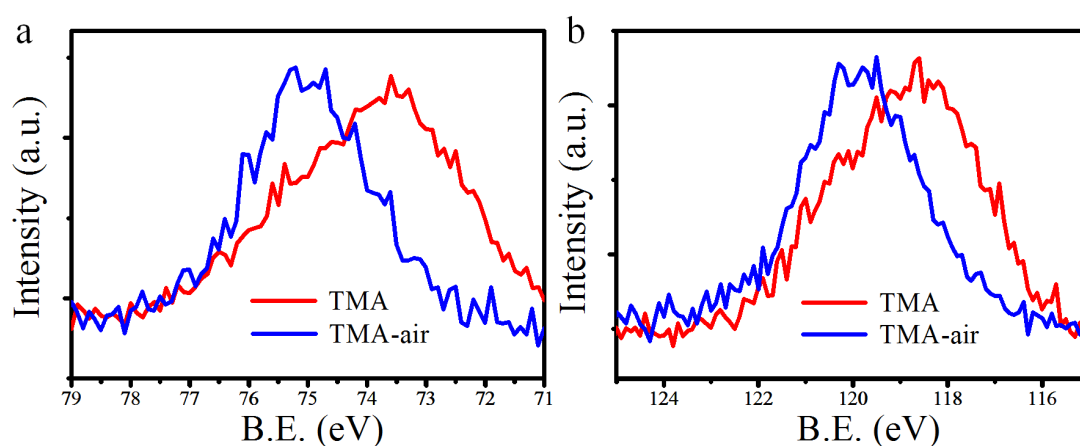


Figure 6.2. (a) Al 2p and (b) Al 2s XPS spectra of 4-phenylenediamine in TMA dosed and air exposed states.

## Interaction between TMA and –OH

4-hydroquinone (4-HQ) was chosen for studying the interaction between –OH and TMA. Figure 6.3 shows the C 1s, Al 2s and Al 2p spectra of 4-hydroquinone in its native, TMA dosed and finally air (H<sub>2</sub>O) exposed states. In Figure 6.3 (a), the reference C 1s core level of 4-HQ doesn't change seriously. Only a tiny shoulder in the lower binding energy region is visible for the TMA dosed sample. The Al core levels in Figure 6.3 b and c show the existence of Al. The positions of the Al 2p and 2s peaks suggest that most of the Al is bound to O. Obviously, the reactivity between TMA and –OH is so high that most of the –CH<sub>3</sub> groups in TMA react with the H from –OH, forming volatile CH<sub>4</sub>. After exposure to air, the C 1s peak shifts back to the initial state of 4-HQ (Figure 6.3 (a)). The Al 2s and 2p peaks show no differences before and after exposure to air, indicating that the Al is already bound to O quantitatively after TMA dosing.

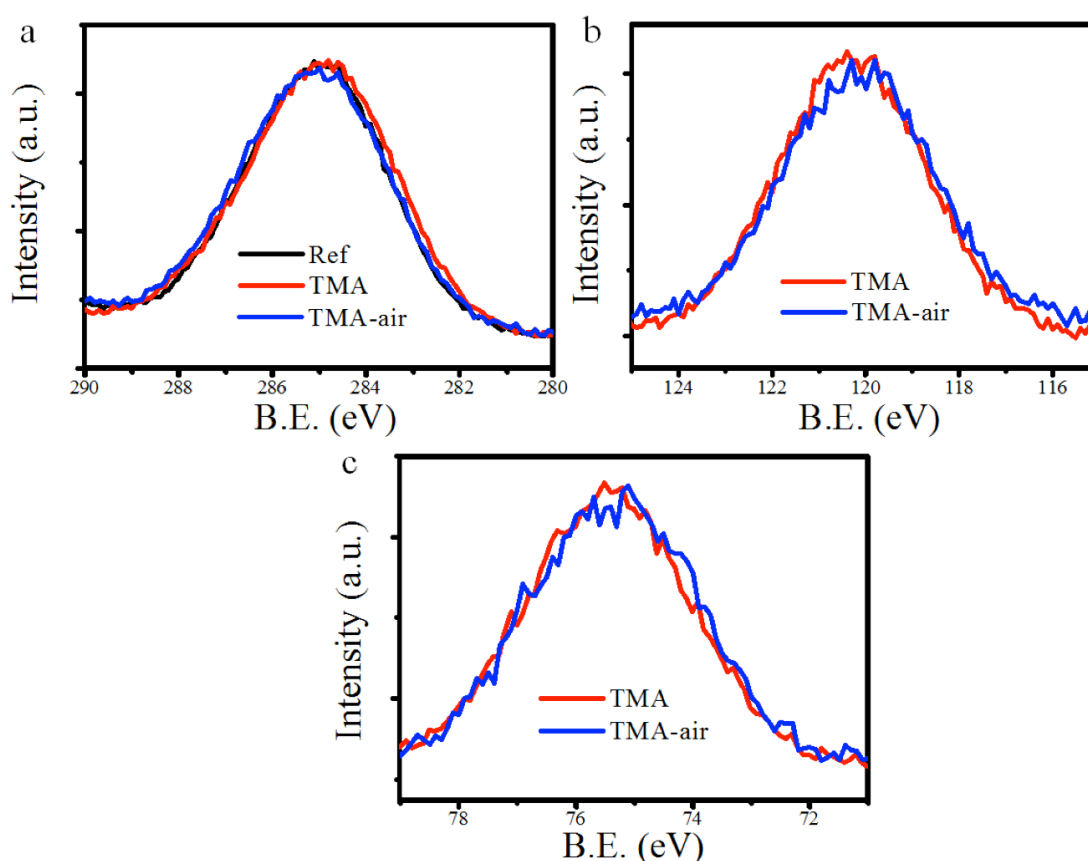


Figure 6.3. (a) C 1s, (b) Al 2p and (c) Al 2s XPS spectra of 4-hydroquinone in the native, TMA dosed and finally air exposed states.

## Interaction between TMA and $-\text{NO}_2$

4-dinitrobenzene (4-DN) was chosen for studying the interaction between  $-\text{NO}_2$  and TMA. Figure 6.4 shows the C 1s and N 1s spectra of 4-dinitrobenzene in its native, TMA dosed and finally air ( $\text{H}_2\text{O}$ ) exposed states. For the C 1s core level in Figure 6.4 a, the tendency is similar to those observed in Figures 6.1 (a) and 6.3 (a), in which a shoulder in the lower binding energy region corresponding to the  $-\text{CH}_3$  in TMA arises after TMA dosing, and it significantly decreases after exposure to air. However, the N 1s peak changes in both shape and intensity after TMA dosing. A new peak arises at binding energies around 400 eV. This has been observed in earlier research when measuring nitrobenzene on  $\text{SiO}_2$  surfaces by XPS. This peak results from the reduction of nitro groups induced by the X-ray irradiation<sup>184</sup>. A closer look to the original reference spectra of 4-dinitrobenzene shows a small peak arising at binding energies around 400 eV. Another peak located at around 406 eV corresponds to  $-\text{NO}_2$  and shifts to lower binding energies as can be seen in Figure 6.4 b. It is unlikely that this shift is also due to X-ray induced reduction, since the  $-\text{NO}_2$  peak recovers to the original position of 4-DN once the sample is exposed to air. The possible reason is that TMA reacts with the  $-\text{NO}_2$  groups after dosing. But this bond between TMA and  $-\text{NO}_2$  is unstable in presence of water. The Al-C reacts to Al-O as indicated by the Al 2s and 2p core levels in Figure 6.5 as a result of TMA reacting with water during air exposure. This reaction breaks the former interaction of TMA and the  $-\text{NO}_2$ , and shifts the  $-\text{NO}_2$  peak back to its original position which can be seen in Figure 6.4 (b).

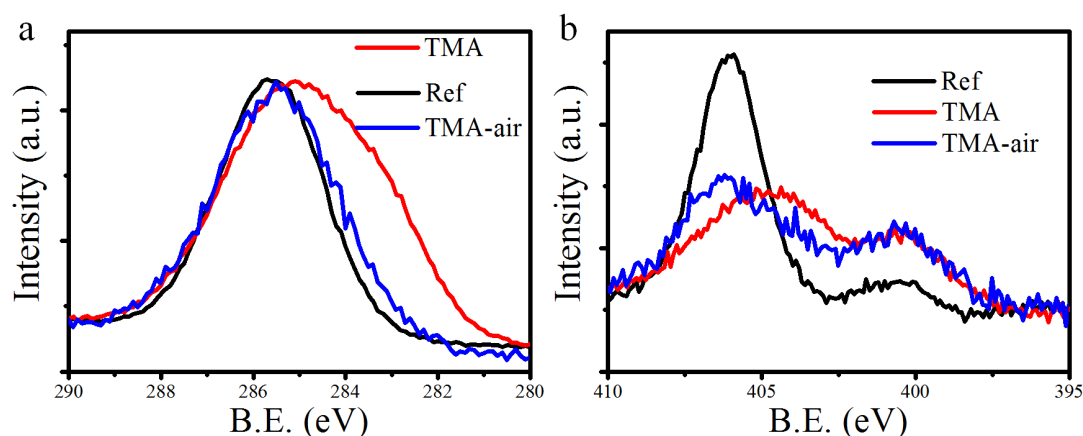


Figure 6.4. (a) C 1s and (b) N 1s XPS spectra of 4-dinitrobenzene in the native, TMA dosed and finally air exposed states.

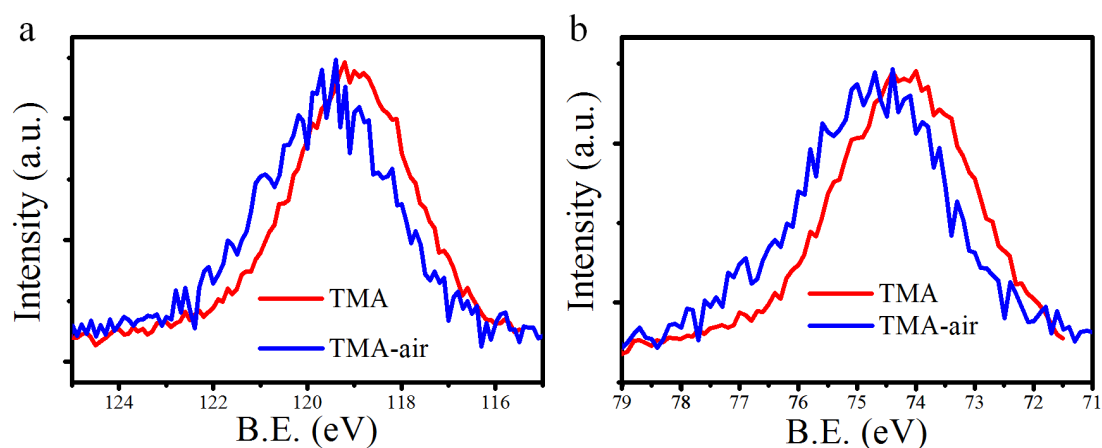


Figure 6.5. (a) Al 2p and (b) Al 2s XPS spectra of 4-dinitrobenzene in TMA dosed and air exposed states.

### Interaction of TMA with both $-\text{NH}_2$ and $-\text{OH}$

4-aminophenol (4-AP) was chosen for studying the preferential interaction of TMA with in presence of  $-\text{NH}_2$  and  $-\text{OH}$  groups. Figure 6.6 shows the C 1s and N 1s spectra of 4-aminophenol in its native, TMA dosed and finally air ( $\text{H}_2\text{O}$ ) exposed states. For the C 1s core level in Figure 6.6 (a), the shoulder at lower binding energies corresponds to C from TMA. It arises after TMA dosing, and significantly decreases after exposure to air. In contrast to the obvious shift towards higher binding energies for N 1s of 4-phenylenediamine in Figure 6.1 b, here only a very small shoulder is observed in the higher binding energies after TMA dosing as shown in Figure 6.6 b. The positions of the Al 2s and 2p peaks in Figure 6.7 for the TMA dosed sample, also confirm the presence of Al-C bonds from TMA<sup>179–181</sup>. It is expected that TMA will easily interact with the  $-\text{OH}$  as shown in the case of the 4-hydroquinone in Figure 6.3. However, TMA also interacts with  $-\text{NH}_2$  although in a lower amount. The N 1s peak almost recovers to the initial state of 4-AP, and the Al 2s and 2p peaks shift to a higher bonding energy region thanks to the formation of the Al-O after exposure to air.

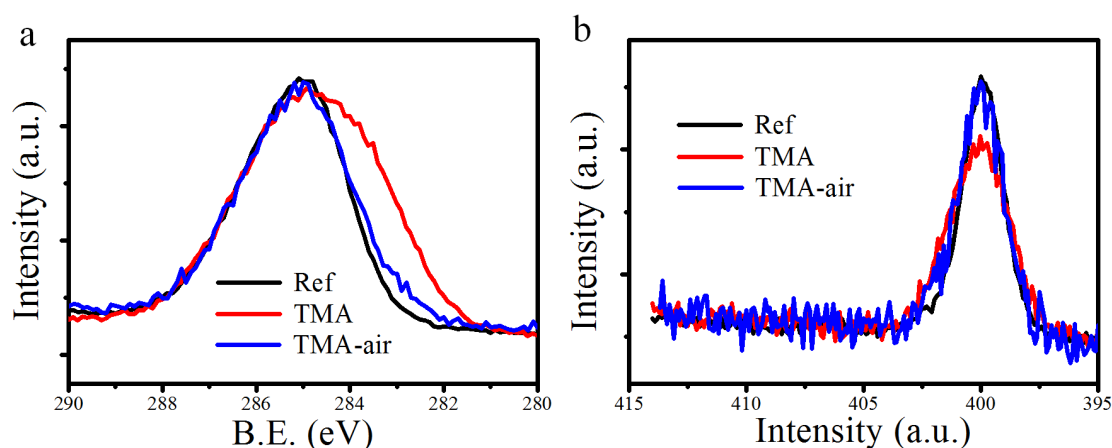


Figure 6.6. (a) C 1s and (b) N 1s XPS spectra of 4-aminophenol in the native, TMA dosed and finally air exposed states.

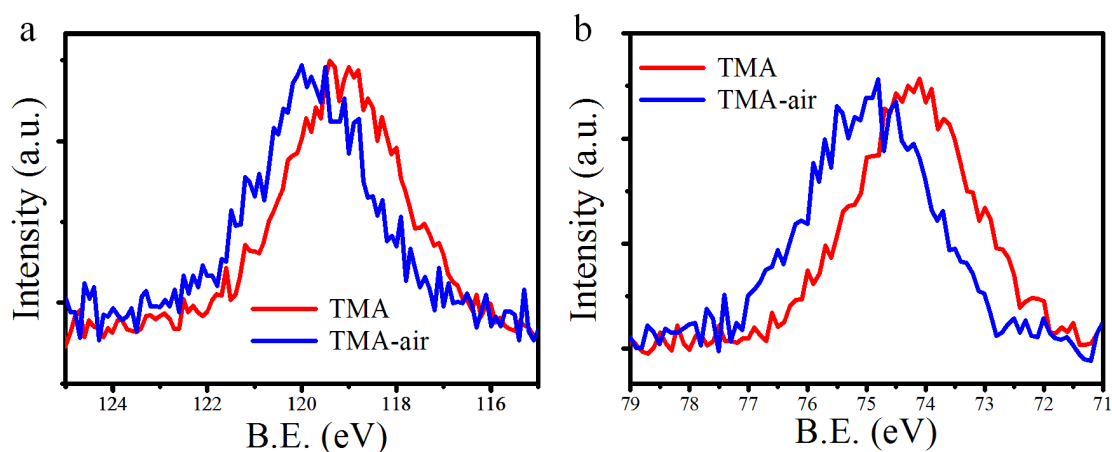


Figure 6.7. (a) Al 2p and (b) Al 2s XPS spectra of 4-aminophenol in TMA dosed and finally air exposed states.

## Interaction of TMA with both $-\text{NO}_2$ and $-\text{OH}$

4-nitrophenol (4-AP) was chosen for studying the interaction of TMA in presence of both  $-\text{NO}_2$  and  $-\text{OH}$  groups. Figure 6.8 (a) shows the C 1s peak changes after the TMA dosing and further after exposure to air. It can be seen that the TMA clearly interacts with the 4-nitrophenol due to the arising shoulder at lower binding energies corresponding to the methyl in TMA. After exposure to air, most of the  $-\text{CH}_3$  reacts with water and desorbs. In the case of the N 1s core level in Figure 6.8 (b), the newly arising peak around 400 eV corresponds to amines, which has already been observed in the case of 4-dinitrobenzene. The peak corresponding to the nitro group at around 406 eV doesn't change seriously in comparison to the obvious shift observed

for 4-DN in Figure 6.4 b. Also here the probable reason is the preference of TMA to react with  $-\text{OH}$ , which lowers the amount of TMA available for  $-\text{NO}_2$ . For the Al core levels in Figure 6.9, the Al 2s and 2p show changes from Al-C to Al-O owing to the  $\text{Al}_2\text{O}_3$  formation after exposure to air.

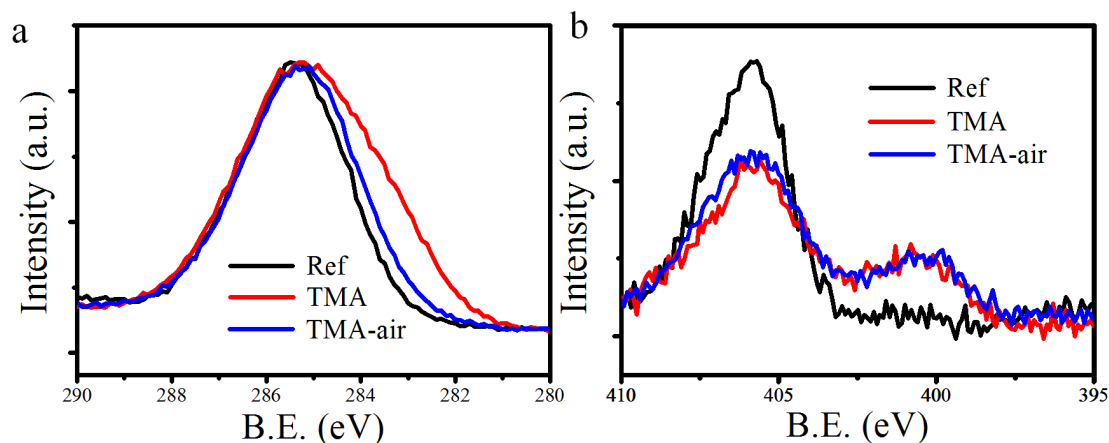


Figure 6.8. (a) C 1s and (b) N 1s XPS spectra of 4-nitrophenol in the native, TMA dosed and finally air exposed states.

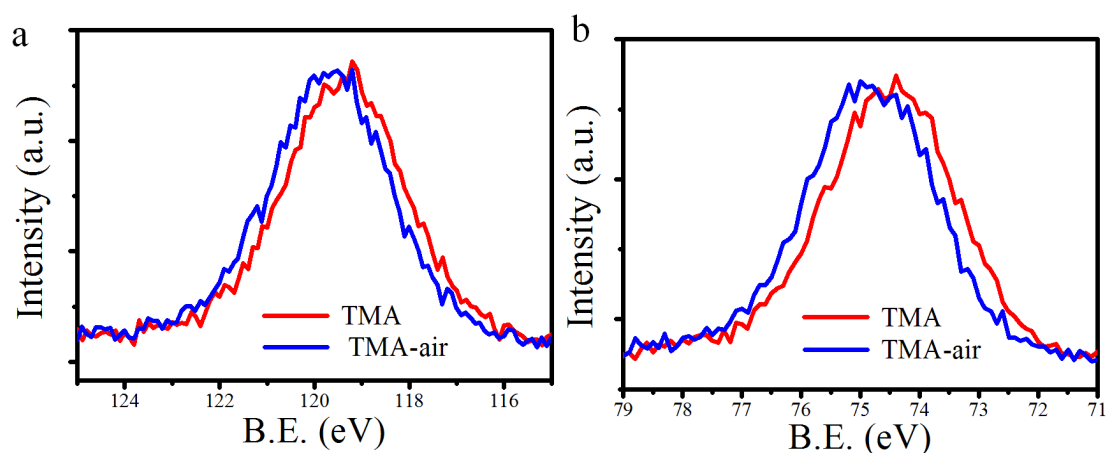


Figure 6.9. (a) Al 2p and (b) Al 2s XPS spectra of 4-nitrophenol in TMA dosed and air exposed states.

## Interaction of TMA with both $-\text{NO}_2$ and $-\text{NH}_2$

P-nitroaniline (4-NA) was chosen as the molecule for studying the interaction of TMA in presence of both  $-\text{NO}_2$  and  $-\text{NH}_2$  groups. For the C 1s peak in Figure 6.10 (a), a large shoulder appears in the lower binding energy region showing the presence of the methyl groups after TMA dosing. It disappears again after exposure to air

resulting from the reaction between the methyl groups from TMA and water from air. In Figure 6.10 (b), the N 1s peaks change significantly after TMA dosing. In the higher binding energy region (around 406 eV), which corresponds to  $-\text{NO}_2$ , on the one hand the peak intensity decreases greatly due to the reduction induced by X-ray irradiation as also observed for nitro group containing molecules 4-DN and 4-NP; on the other hand the peak position shifts towards lower binding energies similar to the case of 4-DN owing to the interaction between the nitro groups and TMA. In the lower binding energy region (around 400 eV), which corresponds to  $-\text{NH}_2$ , the N 1s peak increases in intensity due to the formation of amines after reduction of the nitro groups, but it also shifts towards higher binding energies probably due to the interaction between  $-\text{NH}_2$  and TMA. It appears that TMA interacts with both the nitro and the amine groups.

After exposure to air, the  $-\text{NO}_2$  peak recovers to the initial position observed for 4-NA in Figure 6.10 (b). The  $-\text{NH}_2$  peak at around 400 eV shifts towards lower binding energies but doesn't recover to the initial position of the  $-\text{NH}_2$  peak in 4-NA. The formation of amines after reduction of the nitro groups by X-ray irradiation causes the  $-\text{NH}_2$  peak to broaden and increase in intensity with respect to that of 4-NA<sup>184</sup>. Figure 6.11 shows the changes of the Al core levels after exposure to air, both Al 2s and 2p peaks indicate the change from Al-C to Al-O.

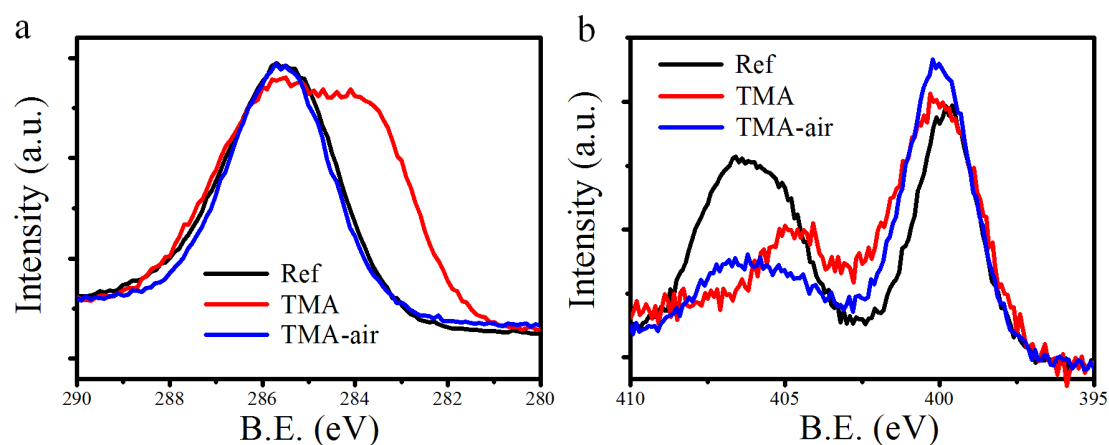


Figure 6.10. (a) C 1s and (b) N 1s XPS spectra of 4-nitroaniline in the native, TMA dosed and finally air exposed states.

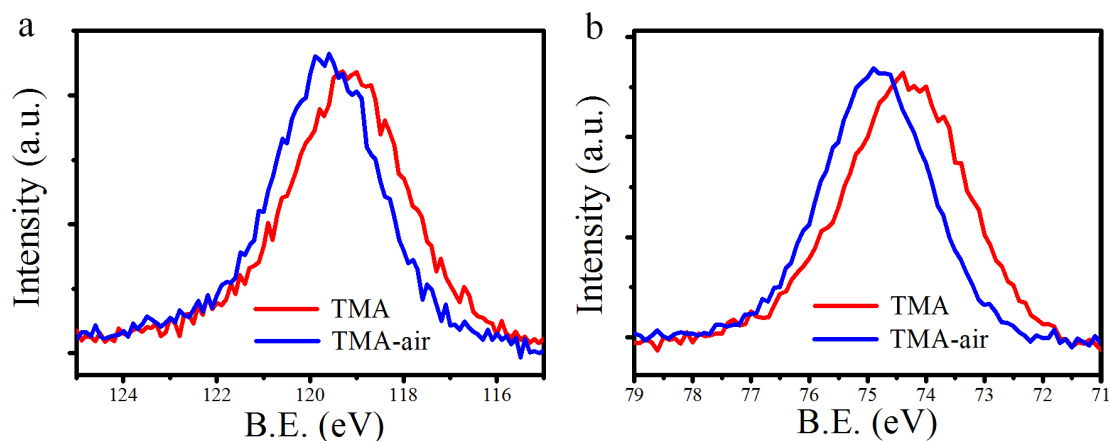


Figure 6.11. (a) Al 2p and (b) Al 2s XPS spectra of 4-nitroaniline in TMA dosed and air exposed state.

It is worth to mention an interesting phenomenon observed here, namely that the color of 4-nitroaniline changed from its original yellow to pure red after the TMA dosing experiment performed in the Savannah 100 reactor (Cambridge Nanotech). This is a clear evidence of an interaction of TMA with 4-NA. Thanks to the interaction between TMA and the 4-nitroaniline, the electronic state of the 4-nitroaniline has been disturbed, which possibly redistributes the electron density in the intermediate compound. This intermediate has an absorption in the light blue range and results a red appearance, different to 4-nitroaniline that is yellow and absorbs in the UV range. Detailed work still needs to be carried out to reveal the electronic states of the intermediate compound. However, the interaction between TMA and 4-nitroaniline is not stable upon exposure to water as observed in the semi-in-situ XPS measurements. The red sample immediately turns back to yellow within less than 3 seconds after exposure to air. For the other investigated molecules no such color changes were observed.

In conclusion, clear evidences for interactions between TMA with all the three functional groups  $-OH$ ,  $-NH_2$  and  $-NO_2$  are found. Their reactivity and stability can be very different. TMA strongly interacts with  $-OH$  groups, and this interaction is very stable even upon exposure to air or humidity. For the  $-NO_2$  or  $-NH_2$ , however, the interactions with TMA are less stable upon exposure to air. When  $-OH$  is present, an interaction between TMA and  $-NO_2$  or  $-NH_2$  still occurs, but in less quantity due to the competition of  $-OH$  for the TMA.

## Interaction of TMA and 4-PD on TiO<sub>2</sub> surface

The interactions of TMA (or phenylenediamine) with p-phenylenediamine (or TMA) on a clean rutile (110) TiO<sub>2</sub> surfaces have also been investigated, in analogy to a MLD process.

### Reaction of 4-phenylenediamine with a TMA terminated TiO<sub>2</sub> surface

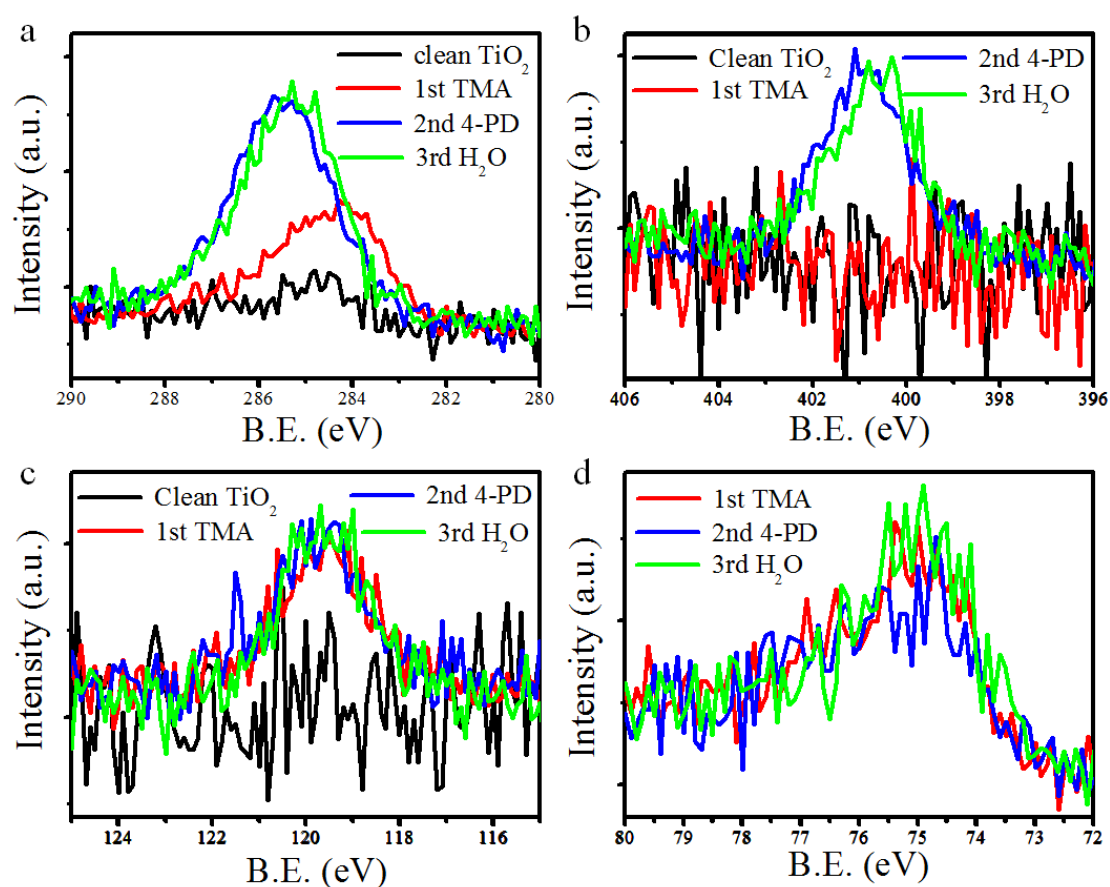


Figure 6.12. (a) C 1s, (b) Al 2p, (c) Al 2s and (d) Al 2p XPS spectra of TiO<sub>2</sub>, after 4-phenylenediamine dosing, after further TMA dosing and finally exposure to H<sub>2</sub>O.

TMA was first dosed to the TiO<sub>2</sub> surface, and subsequently 4-phenylenediamine was introduced to interact with the TMA on the solid surface. As shown in Figure 6.12, the TiO<sub>2</sub> substrate was free of carbon, nitrogen and aluminum

impurities. After TMA dosing, the C 1s, Al 2s and 2p peaks start to appear in the spectra. Upon later dosing of 4-phenylenediamine, the position of the C 1s peak in Figure 6.12 (a) changes, which is the contribution of the phenyl ring in 4-phenylenediamine. The N 1s peak from  $-\text{NH}_2$  also appears. Upon exposure to  $\text{H}_2\text{O}$ , the N 1s slightly shifts towards lower binding energies. As observed in Figure 6.1 (b), due to the interaction with TMA the N 1s peak position of  $-\text{NH}_2$  is at higher binding energies than that of the original 4-phenylenediamine. Dosing of water breaks the interaction between  $-\text{NH}_2$  and TMA, thus the N 1s peak shifts back to the original position of  $-\text{NH}_2$  in 4-phenylenediamine towards the lower binding energy region. This is the exact opposite shift compared to the case of dosing TMA to 4-phenylenediamine for the pellet samples in Figure 6.1 (b).

### Reaction of TMA with a 4-phenylenediamine terminated $\text{TiO}_2$ surface

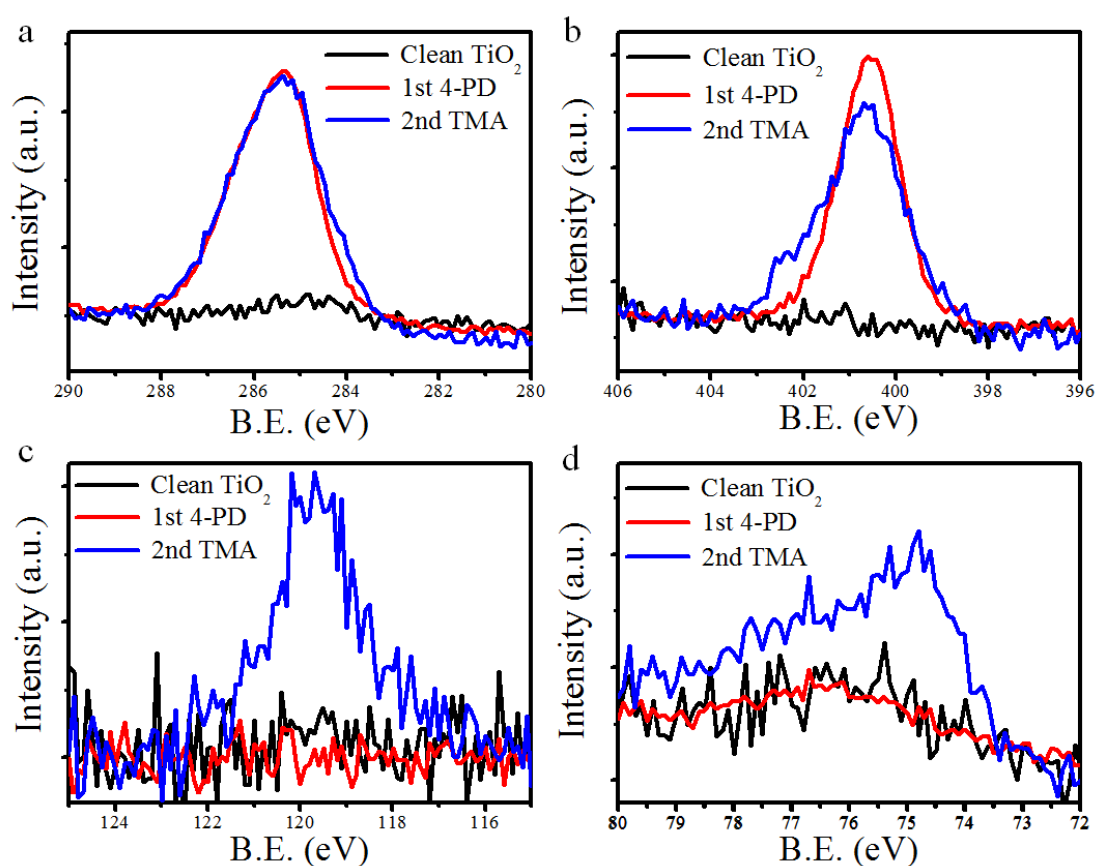


Figure 6.13. XPS spectra of Clean  $\text{TiO}_2$ , 4-phenylenediamine dosed and later TMA dosed sample with (a) C 1s, (b) N 1s, (c) Al 2s and (d) Al 2p.

In this section, we describe the experiments of first dosing 4-phenylenediamine and then TMA to the TiO<sub>2</sub> surface. After dosing 4-phenylenediamine, the C 1s and N 1s peak arises originating from the phenyl rings and amine groups of the molecules. Later dosing of TMA induces the rise of Al 2s and 2p core level peaks in Figure 6.13 (c) and (d), and changes in C 1s and N 1s peaks in Figure 6.13 (a) and (b). In Figure 6.13 (a), a small shoulder at the lower binding energy region arises, which corresponds to the methyl groups in TMA. In Figure 6.13 (b), the shoulder at higher binding energies for the N 1s also appears. This is consistent with an interaction between TMA and 4-phenylenediamine in the case of the pellet samples in Figure 6.1 (b).

The results of these two experiments performed on the TiO<sub>2</sub> substrate are consistent with those performed on the pellet sample, which were exposed to the TMA. Individual experiments still need to be performed with other molecules, but the interaction between functional groups and precursors can be similar for both MLD growth and infiltration processes.

## Theoretical calculations

Theoretical calculations were also performed for a better understanding of the interactions between TMA and –OH, –NH<sub>2</sub> or –NO<sub>2</sub> groups. For this purpose, three molecules containing only one functional group including 4-hydroquinone, 4-phenylenediamine and 4-dinitrobenzen were chosen for the calculation. The calculation is based on density functional theory (DFT) using the Material Studio software. Details of the calculations can be found in the experimental section.

### Interaction between TMA and 4-hydroquinone

Within TMA, the Al is sp<sub>2</sub> hybridized involving one 3s and two 3p orbitals, and bound to three methyl groups<sup>185,186</sup>. The remaining empty p orbital of the Al atom makes TMA electron deficient and therefore a strong Lewis acid. The O in –OH of 4-hydroquinone has a lone electron pair. Once TMA and 4-hydroquinone are approaching each other, the O atom strongly attracts TMA similar to the intensely studied reaction between TMA and water<sup>185,186</sup>. Therefore, the interaction of TMA with 4-hydroquinone starts first by adsorption of TMA to the O site (E<sub>2</sub> state in Figure 6.14). In the next stage, one methyl group from the adsorbed TMA reacts with the H

atom from the  $\text{-OH}$  group to form  $\text{CH}_4$  that subsequently desorbs. For this step an energy barrier of 32.5 kJ/mol needs to be overcome. After the reaction, the formed  $\text{CH}_4$  desorbs and TMA is chemically bound to the 4-hydroquinone.

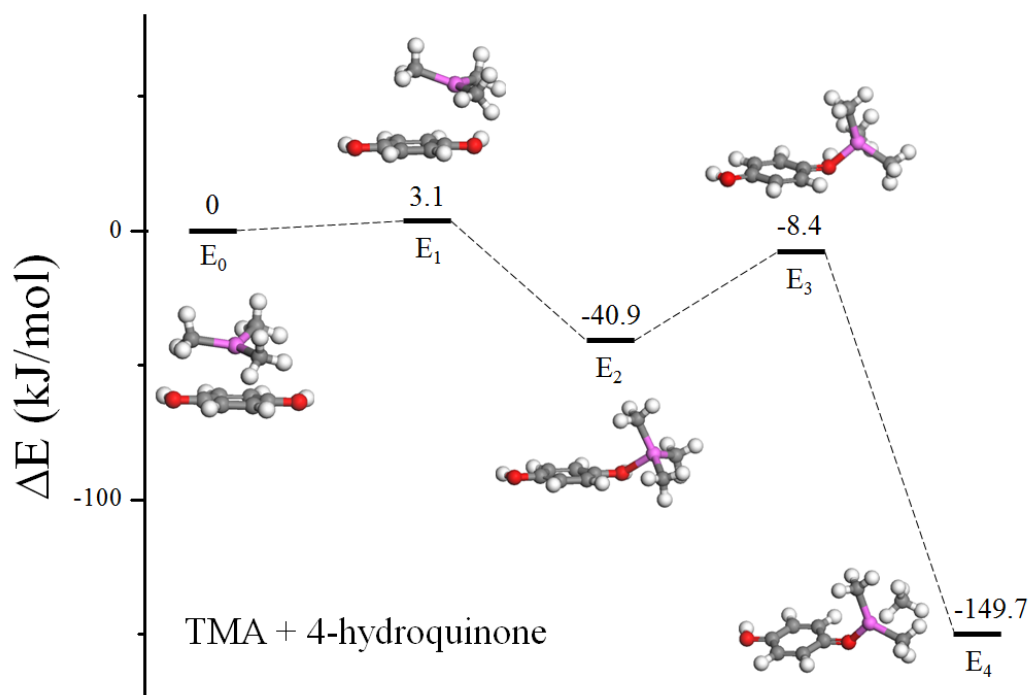


Figure 6.14. Potential path and predicted energy profile for the interaction between TMA and 4-hydroquinone.

### Interaction between TMA and 4-phenylenediamine

The calculation of the energy profile for the reaction between TMA and 4-phenylenediamine is also performed, and shown in Figure 6.15. Similar to the case of  $\text{-OH}$ , the N of  $\text{-NH}_2$  also contains a lone electron pair, which attracts TMA upon approaching. The interaction starts by adsorption of TMA to the N atom ( $E_2$  state in Figure 6.15). After the adsorption, additional energy is needed for activating the reaction between the methyl group in TMA and one of the H in  $\text{-NH}_2$ . If the reaction is complete, the byproduct of  $\text{CH}_4$  will desorb and TMA is chemically bound to the 4-phenylenediamine.

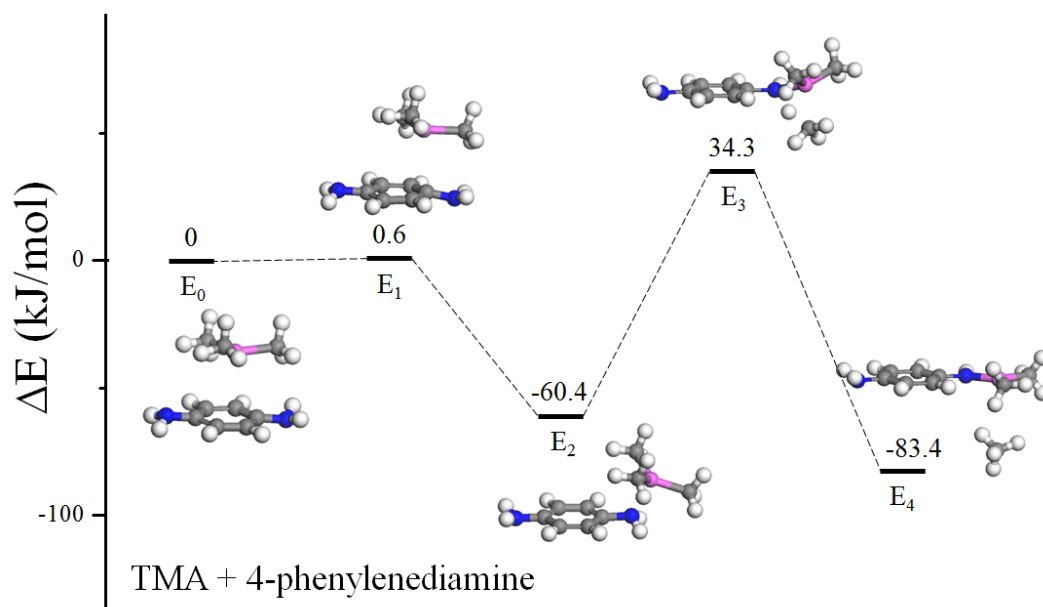


Figure 6.15. Potential path and predicted energy profile for the interaction between TMA and 4-phenylenediamine.

#### Interaction between TMA and 4-dinitrobenzene

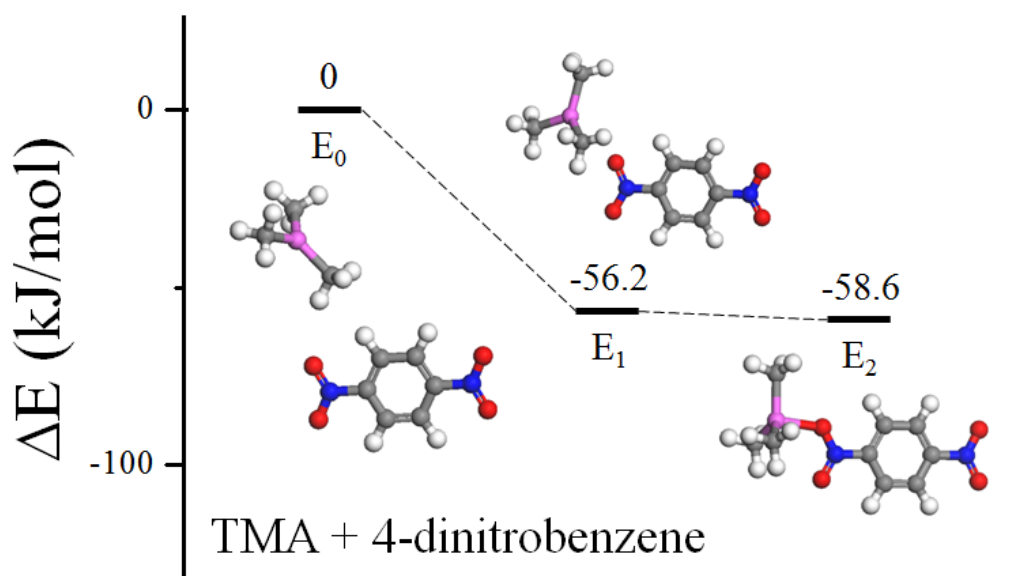


Figure 6.16. Potential path and predicted energy profile for the interaction between TMA and 4-dinitrobenzene.

The interaction between TMA and 4-dinitrobenzene was calculated and the predicted energy profile is shown in Figure 6.16. The nitro group has its own resonance with one electron initially from the N being delocalized within the  $-\text{NO}_2$

group. This makes the N electron deficient and one of the O atoms electron-rich. The interaction between TMA and 4-dinitrobenzene also starts from an adsorption of TMA to the lone electron pair of the O ( $E_2$  state in Figure 6.16). However different to the previous cases for the  $-OH$  and  $-NH_2$  groups, there is no H present in 4-nitrobenzen for reacting with the methyl group of TMA. Therefore, the adsorption ( $E_2$ ) is the final state of the interaction between  $-NO_2$  and TMA.

The calculations show that the interaction always starts by an adsorption of TMA to specific sites. According to the calculated adsorption energies in Table 6.1, these are all exothermic processes and likely to occur. Specifically, the adsorption of TMA to 4-phenylenediamine has the highest energy gain of  $-60.39$  kJ/mol, and TMA with 4-hydroquinone the lowest energy gain. Therefore, TMA will be attracted by the three functional groups in the order of  $-NH_2 > -NO_2 > -OH$ . The adsorption is due to the electronic interactions where the empty p orbital of the Al atom in TMA is pointing towards the lone pair of the electron rich atoms in the functional groups as shown in Figure 6.17.

Table 6.1. Calculated adsorption energy, energy barrier and total energy gain for the potential reaction path of TMA with 4-hydroquinone, 4-phenylenediamine and 4-dinitrobenzene.

| Functional Groups (molecules) | Adsorption: $E_2-E_0$ (kJ/mol) | Energy Barrier: $E_3-E_2$ (kJ/mol) | Total Gain: $E_4-E_0$ (kJ/mol) |
|-------------------------------|--------------------------------|------------------------------------|--------------------------------|
| OH (4-hydroquinone)           | -40.86                         | 73.34                              | -108.86                        |
| $NH_2$ (4-phenylenediamine)   | -60.39                         | 155.06                             | -22.96                         |
| $NO_2$ (4-dinitrobenzene)     | -58.57                         | /                                  | /                              |

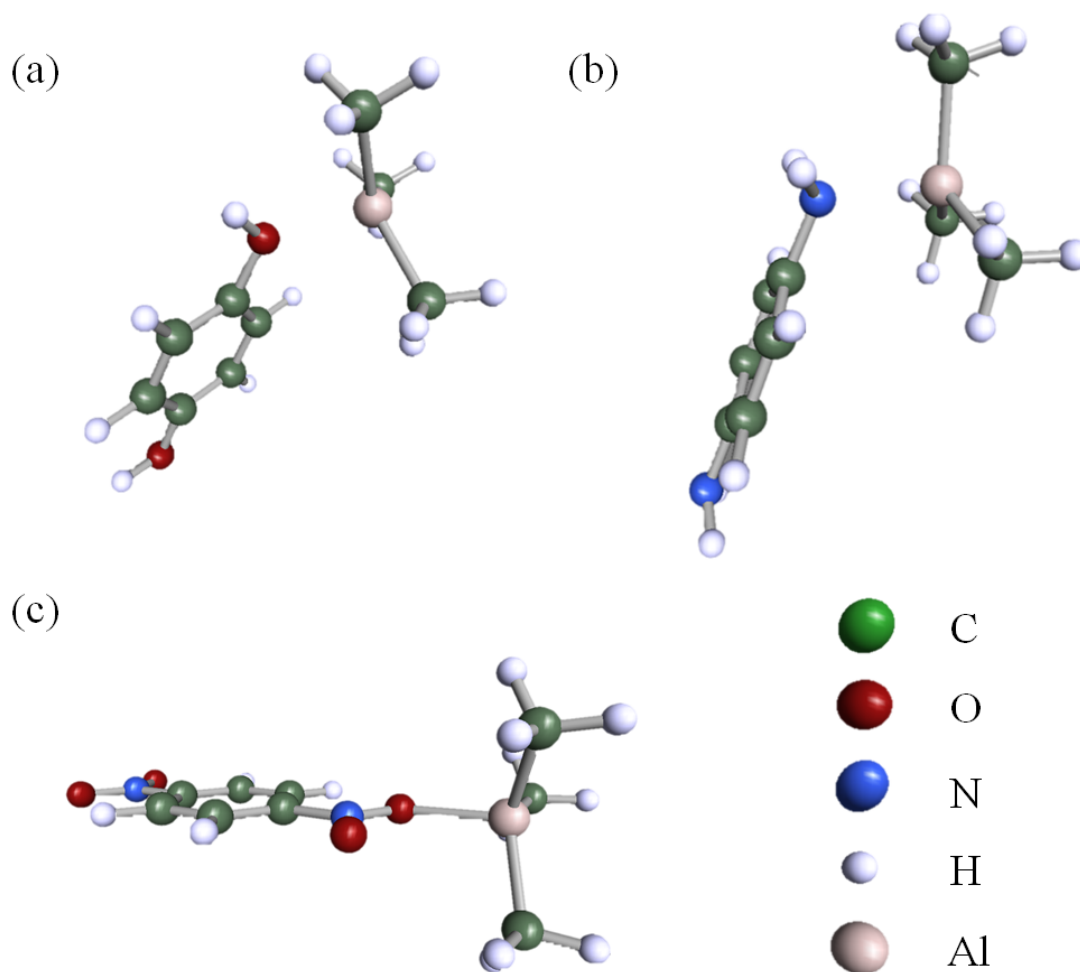


Figure 6.17. Calculated structures of TMA adsorbed to different molecules, (a) 4-hydroquinone, (a) 4-phenylenediamine and (c) 4-dinitrobenzene. As can be seen in the Figures, the empty p orbital of Al in TMA, which is perpendicular to the plane of the three  $sp_2$  hybridized  $AlC_3$  orbitals, is pointing towards the lone pair of the O in  $-OH$ , the N in  $-NH_2$  and the O in  $-NO_2$ , respectively.

After the adsorption, an energy barrier needs to be overcome for activating the reaction between the methyl group from TMA and the H from the functional groups. Except for  $-NO_2$ , which doesn't contain H atoms, the binding will be the final state. For functional groups containing H atoms ( $-NH_2$  and  $-OH$ ), the final state depends on the activation energy barrier. In Table 6.1, the calculated activation energy barrier for the  $-NH_2$  group is 155.06 kJ/mol, much higher than the 73.34 kJ/mol for the  $-OH$  group. Thus, it is expected that the reactivity of  $-OH$  with TMA is stronger than that of  $NH_2$  with TMA. This is partly verified by the fact that aluminum oxide is much easier to grow<sup>187</sup> than aluminum nitride by ALD. Typically the nitride process needs

to be performed at much higher temperatures with  $\text{NH}_3$  or needs to be assisted with nitrogen plasma<sup>188–190</sup>.

## Correlation between experimental results and Theoretical calculations

The calculations predict that all the investigated functional groups will attract TMA at different electron rich sites. However, the final chemical bonding of TMA to these functional groups depends on the activation energy barrier for the reaction between methyl from TMA and H from the functional groups.

In the case of 4-hydroquinone (Figure 6.3), after TMA dosing the Al-O bond is already the dominant component in the Al 2s and 2p peaks, and only a very small amount of methyl groups is remaining. This indicates that reaction is nearly quantitative and finished.

For 4-phenylethylenediamine (Figure 6.1 and Figure 6.2), the TMA pulls electrons from N upon approaching (Figure 6.17 (b)). This makes the Al being more reduced, and the N being more oxidized, which causes the shift of the  $-\text{NH}_2$  peak to higher binding energies. It appears that this is the final state of the interaction between TMA and  $-\text{NH}_2$ . If the activation energy barrier is overcome, the methyl group from TMA will react with the H from  $-\text{NH}_2$ . An Al-N bond will form, which will cause N to become more reduced and accordingly shifts the peak of the  $-\text{NH}_2$  to lower binding energies. However, the N 1s peak of the  $-\text{NH}_2$  shifts not only towards high binding energies, but it is also reversible so that it recovers upon exposure to air indicating an unstable adsorption of TMA to the amines.

For the  $-\text{NO}_2$ , the witnessed shift of the N 1s peak after TMA dosing and its recovery upon exposure to air in Figure 6.4 (b), also suggest an unstable bond of TMA with  $-\text{NO}_2$ . The shift of the N 1s peak after TMA dosing is due to the interaction between TMA and one of the O from  $-\text{NO}_2$  as shown in Figure 6.17 (c). Due to the resonance, the  $-\text{NO}_2$  peak is often broad and contains two shakeup peaks<sup>191–194</sup>. After the TMA dosing, the shake-up peak intensity is suppressed indicating a disturbance of the resonance, or steric hindrance by the adsorbed TMA. This is similar to the case of the 2,3,5,6 tetramethyl-p-nitroaniline, where it has been reported that the methyl group in 2,3,5,6 tetramethyl-p-nitroaniline sterically inhibits the resonance of the nitro group. The  $-\text{NO}_2$  peak of 2,3,5,6 tetramethyl-p-nitroaniline

in XPS is much narrowed compared to that of 4-nitroaniline<sup>195,196</sup>. Upon exposure to air, water will react with TMA and break this interaction, recovering the resonance and consequently the shakeup features for the nitro groups.

Based on the experimental and calculation results, we conclude that the interaction between TMA and –OH will easily occur and TMA will chemisorb to –OH even at very low temperatures; for –NH<sub>2</sub>, TMA will only adsorb to the N site, as shown in Figure 6.17 (b), at normal conditions due to the high activation energy barrier for the final reaction; for –NO<sub>2</sub>, –TMA will only adsorb to the O site. For both –NH<sub>2</sub> and –NO<sub>2</sub>, the intermediates from the interaction with TMA are not stable upon exposure to air as TMA will instantly desorb and react with water.

This conclusion is in agreement with earlier research on the ALD processes. The process using TMA and 4-hydroquinone was successfully applied and studied at low temperatures 180-220 °C<sup>197-199</sup>. However, there is only one publication describing the process between TMA and 4-phenylenediamine, which works at 400 °C. Yet the grown film is still unstable upon humidity<sup>200</sup>. The strong adsorption of TMA to the –NO<sub>2</sub> group has already been used for enabling a nucleation of alumina on inert substrates. By first dosing NO<sub>2</sub> gas onto carbon nanotubes or graphene, or grafting of carbon nanotubes with 4-nitroaniline, subsequent growth of Al<sub>2</sub>O<sub>3</sub> was successfully performed<sup>201-204</sup>. It is expected that other precursors like diethyl zinc (DEZ) or titanium isopropoxide, etc. will also show similar reaction paths. But detailed investigations on the individual cases still need to be carried out.

## 6.4 Conclusions

In this chapter, we studied the interaction between different organic functional groups and TMA, where six molecules with various combinations of functional groups including –OH, –NH<sub>2</sub> and –NO<sub>2</sub>, are chosen for the investigation. The experimental results and theoretical calculations show that: the TMA precursor will initially adsorb to the electron rich site of the molecules, specifically the empty p orbital of the Al atom in TMA will be attracted by the lone pairs of the electron rich atoms; additional energy is needed for the activation of the reaction between the methyl groups from TMA and the H from the organic functional groups; finally, if the activation energy barrier is overcome, CH<sub>4</sub> will form and desorb, and Al will remain chemically bound to the molecule. The formation of chemisorbed TMA in MLD or

infiltration processes greatly depends on the activation energy barrier for a reaction with different functional groups. It is observed that: for  $-OH$ , TMA will chemisorb to  $-OH$  and form stable Al-O bonds; for  $-NH_2$ , TMA only adsorbs to the N site at normal conditions, and Al-N forms only when additional energy is provided; for  $-NO_2$ , TMA only adsorbs to the O site. This understanding of the interaction between TMA and various functional groups might also prove similar to other precursors or functional groups. Thus, the result here will be helpful for the future design of processes for organic-inorganic hybrid materials by MLD or modifying soft materials by vapor phase infiltrations.



---

# Chapter 7

## Conclusions and Future Perspectives

This thesis presents strategies for ALD based functionalization of nanomaterials, and can be divided into three parts: i) synthesis of various nanomaterials through ALD; ii) ALD enabled functionalization of carbon based materials including graphene and carbon nanotubes; iii) fundamental studies of interactions between ALD precursors and organic functional groups.

In the first part, we started by using different templates for the synthesis of ZnO based nanomaterials through ALD. ZnO nanostructures in various dimensions ranging from 0D to 2D are shown. This synthetic route by ALD is shown as a generally applicable method, and the nanomaterials can be extended from ZnO to various metal oxides, or beyond oxides.

In the second part, we show two examples of using ALD to grow metal oxide nanoparticles on carbon materials, graphene and carbon nanotubes. In the first example, ALD was applied to deposit RuO<sub>2</sub> nanoparticles for managing the chemical defects on graphene. For its high conductivity and surface area, graphene has great potential for electrochemical applications like supercapacitors, but the defects have a negative effect on the capacitive performances. We show that the defects can be controllably replaced RuO<sub>2</sub> nanoparticles. After the functionalization, the specific capacitance and stability of the fabricated supercapacitors are greatly enhanced. The second example uses carbon nanotubes. ALD was applied to deposit Co<sub>3</sub>O<sub>4</sub> nanoparticles on defect sites of carbon nanotubes. The resulting Co<sub>3</sub>O<sub>4</sub>/CNT composite showed excellent reactivity for the oxygen reduction reaction (ORR). However, the mobility of the nanoparticles limited the stability of the system. By adding a nitrogen doped carbon shell, the nanoparticles became immobilized. In this way, not only the reactivity was maintained, but also the stability was greatly enhanced. These two examples show that ALD has great advantages over other methodologies, specifically for an accurate control of the size and density of the grown nanoparticles, and their uniform distribution in position and size.

Lastly, to extend the strategy of nanoparticle growth to further functionalities beyond alcohols or carboxylic acids and inspired by the earlier work of the group on vapor phase infiltrations process of spider silk<sup>72</sup>, egg collagen<sup>74</sup> and porphyrins<sup>70</sup>, the interactions between the ALD precursor TMA and functional groups were studied. It was found that the TMA precursor will firstly adsorb to the electron rich site of a functional group, and additional energy is needed for activating the reaction between the methyl groups in TMA and the H in the functional groups; once this energy barrier is overcome, CH<sub>4</sub> will form and desorb and TMA will be chemically bound to the molecules or the surfaces. The formation of chemisorbed TMA in MLD or in an infiltration process greatly depends on the activation energy barriers: TMA will easily bind to O in –OH containing molecules or surfaces; while it will only adsorb onto the N site of –NH<sub>2</sub> containing molecules or surfaces at normal conditions; it will also easily adsorb to the O site of –NO<sub>2</sub> containing molecules or surfaces. This understanding of interactions between precursors and functional groups will certainly be helpful for the future design of the process of organic-inorganic hybrid materials grown by MLD or soft materials' modification by infiltration.

All the research performed in this thesis is related to the ALD technology practically and fundamentally. It is our purpose to convey the idea that ALD is a powerful technology for thin film deposition, but also for nanomaterials functionalization. Future work may be more focused on exploring the potential applications of the synthesized materials or structures, for example the various ZnO or other metal oxides based nanostructures shown in chapter 2. The nanoparticles deposited by ALD may also have further potential application fields such as catalysis or sensing. Interestingly, the earlier work on ALD infiltration of natural or synthesized polymers is still not investigated deeply and the knowledge about the process is only vague. The fundamental research on the reaction pathways between various ALD precursors and different functional groups, or the applied research on pursuing interesting properties through infiltration should be intensified.

---

# Bibliography

- (1) Nel, A.; Xia, T.; Mädler, L.; Li N. Toxic Potential of Materials at the Nanolevel. *Science* **2006**, *311*, 622–628.
- (2) Buzea, C.; Pacheco, I. I.; Robbie, K. Nanomaterials and Nanoparticles: Sources and Toxicity. *Biointerphases* **2007**, *2*, MR17–MR71.
- (3) Cao, G.; Wang, Y. *Nanostructures and Nanomaterials: Synthesis, Properties, and Applications*. World Scientific Series in Nanoscience and Nanotechnology, 2011.
- (4) Bogue, R. Nanomaterials for New and Emerging Physical Sensing Applications: A Review of Recent Developments. *Sens. Rev.* **2015**, *35*, 321–328.
- (5) Kumar, A.; Yadav, N.; Bhatt, M.; Mishra, N. K.; Chaudhary, P.; Singh, R. Sol-Gel Derived Nanomaterials and It's Applications: A Review. *Res. J. Chem. Sci.* **2015**, *5*, 98–105.
- (6) Sharma, N.; Ojha, H.; Bharadwaj, A.; Pathak, D. P.; Sharma, R. K. Preparation and Catalytic Applications of Nanomaterials: A Review. *RSC Adv.* **2015**, *5*, 53381–53403.
- (7) Holzinger, M.; Le Goff, A.; Cosnier, S. Nanomaterials for Biosensing Applications: A Review. *Front. Chem.* **2014**, *2*, 63 (1-10).
- (8) Pinna, N.; Knez, M. *Atomic Layer Deposition of Nanostructured Materials*; Wiley-VCH: Weinheim, Germany, 2011.
- (9) Suntola, T.; Antson, J. Method for Producing Compound Thin Films. U.S. Patent No. 4058430, 1977.
- (10) Shevjakov, A. M.; Kuznetsova, G. N.; Aleskovskii, V. B. In Chemistry of High-Temperature Materials, Proceedings of the Second USSR Conference on High-Temperature Chemistry of Oxides. Russia, 1965, 149–155.
- (11) Lindfors, S. G.; Pakkala, A. J.; Suntola, T. S. Method for Performing Growth of Compound Thin Films. U.S. Patent No. 4413022, 1983.
- (12) Kim, H. Atomic Layer Deposition of Metal and Nitride Thin Films: Current Research Efforts and Applications for Semiconductor Device Processing. *J. Vac. Sci. Technol. B Microelectron. Nanom. Struct.* **2003**, *21*, 2231-2261.
- (13) Lee, B.; Mordi, G.; Kim, M. J.; Chabal, Y. J.; Vogel, E. M.; Wallace, R. M.; Cho, K. J.; Colombo, L.; Kim, J. Characteristics of High-k Al<sub>2</sub>O<sub>3</sub> Dielectric

- Using Ozone-Based Atomic Layer Deposition for Dual-Gated Graphene Devices. *Appl. Phys. Lett.* **2010**, *97*, 043107.
- (14) Alaboson, J. M. P.; Wang, Q. H.; Emery, J. D.; Lipson, A. L.; Bedzyk, M. J.; Elam, J. W.; Pellin, M. J.; Hersam, M. C. Seeding Atomic Layer Deposition of High-k Dielectrics on Epitaxial Graphene with Organic Self-Assembled Monolayers. *ACS Nano* **2011**, *5*, 5223–5232.
- (15) Kim, H.; Lee, H.-B.-R.; Maeng, W.-J. Applications of Atomic Layer Deposition to Nanofabrication and Emerging Nanodevices. *Thin Solid Films* **2009**, *517*, 2563–2580.
- (16) Kuesters, K. H.; Beug, M. F.; Schroeder, U.; Nagel, N.; Bewersdorff, U.; Dallmann, G.; Jakschik, S.; Knoefler, R.; Kudelka, S.; Ludwig, C.; Manger, D.; Mueller, W.; Tilke, A. New Materials in Memory Development Sub 50 nm: Trends in Flash and DRAM. *Adv. Eng. Mater.* **2009**, *11*, 241–248.
- (17) Niinistö, J.; Kukli, K.; Heikkilä, M.; Ritala, M.; Leskelä, M. Atomic Layer Deposition of High-k Oxides of the Group 4 Metals for Memory Applications. *Adv. Eng. Mater.* **2009**, *11*, 223–234.
- (18) Kawahara, T.; Yamamuka, M.; Yuuki, A.; Ono, K. (Ba, Sr)TiO<sub>3</sub> Films Prepared by Liquid Source Chemical Vapor Deposition on Ru Electrodes. *Jpn. J. Appl. Phys.* **1996**, *35*, 4880–4885.
- (19) Tsai, M. S.; Sun, S. C.; Tseng, T. Effect of Bottom Electrode Materials on the Electrical and Reliability Characteristics of (Ba, Sr)TiO<sub>3</sub> Capacitors. *IEEE Trans. Electron Devices* **1999**, *46*, 1829–1838.
- (20) Saarenpää, H.; Niemi, T.; Tukiainen, A.; Lemmetyinen, H.; Tkachenko, N. Aluminum Doped Zinc Oxide Films Grown by Atomic Layer Deposition for Organic Photovoltaic Devices. *Sol. Energy Mater. Sol. Cells* **2010**, *94*, 1379–1383.
- (21) Van Delft, J. A.; Garcia-Alonso, D.; Kessels, W. M. M. Atomic Layer Deposition for Photovoltaics: Applications and Prospects for Solar Cell Manufacturing. *Semicond. Sci. Technol.* **2012**, *27*, 074002.
- (22) Mayer, M. T.; Lin, Y.; Yuan, G.; Wang, D. Forming Heterojunctions at the Nanoscale for Improved Photoelectrochemical Water Splitting by Semiconductor Materials: Case Studies on Hematite. *Acc. Chem. Res.* **2013**, *46*, 1558–1566.
- (23) Chen, Y. W.; Prange, J. D.; Dühnen, S.; Park, Y.; Gunji, M.; Chidsey, C. E. D.; McIntyre, P. C. Atomic Layer-Deposited Tunnel Oxide Stabilizes Silicon Photoanodes for Water Oxidation. *Nat. Mater.* **2011**, *10*, 539–544.
- (24) Lin, Y.; Zhou, S.; Sheehan, W.; Wang, D. Nanonet-Based Hematite Heteronanostructures for Efficient Solar Water Splitting. *J. Am. Chem. Soc.* **2011**, *133*, 2398–2401.

- (25) Lee, S.; Park, S.; Han, G. S.; Kim, D. H.; Noh, J. H.; Cho, I. S.; Jung, H. S.; Hong, K. S. Transparent-Conducting-Oxide Nanowire Arrays for Efficient Photoelectrochemical Energy Conversion. *Nanoscale* **2014**, *6*, 8649–8655.
- (26) Mayer, M. T.; Du, C.; Wang, D. Hematite/Si Nanowire Dual-Absorber System for Photoelectrochemical Water Splitting at Low Applied Potentials. *J. Am. Chem. Soc.* **2012**, *134*, 12406–12409.
- (27) Sci, C.; Formal, F. Le; Nicolas, T.; Cornuz, M.; Moehl, T.; Gr, M.; Sivula, K. Passivating Surface States on Water Splitting Hematite Photoanodes with. *Chem. Sci.* **2011**, *2*, 737–743.
- (28) Li, C.; Wang, T.; Luo, Z.; Zhang, D.; Gong, J. Transparent ALD-Grown Ta<sub>2</sub>O<sub>5</sub> Protective Layer for Highly Stable ZnO Photoelectrode in Solar Water Splitting. *Chem. Commun.* **2015**, *51*, 7290–7293.
- (29) Dingemans, G.; Kessels, W. M. M. Status and Prospects of Al<sub>2</sub>O<sub>3</sub>-Based Surface Passivation Schemes for Silicon Solar Cells. *J. Vac. Sci. Technol. A* **2012**, *30*, 040802.
- (30) Chang, C.-Y.; Tsai, F.-Y. Efficient and Air-Stable Plastics-Based Polymer Solar Cells Enabled by Atomic Layer Deposition. *J. Mater. Chem.* **2011**, *21*, 5710.
- (31) Potscavage, W. J.; Yoo, S.; Domercq, B.; Kippelen, B. Encapsulation of pentacene/C<sub>60</sub> Organic Solar Cells with Al<sub>2</sub>O<sub>3</sub> Deposited by Atomic Layer Deposition. *Appl. Phys. Lett.* **2007**, *90*, 253511.
- (32) Sarkar, S.; Culp, J. H.; Whyland, J. T.; Garvan, M.; Misra, V. Encapsulation of Organic Solar Cells with Ultrathin Barrier Layers Deposited by Ozone-Based Atomic Layer Deposition. *Org. Electron.* **2010**, *11*, 1896–1900.
- (33) Chang, C.-Y.; Chou, C.-T.; Lee, Y.-J.; Chen, M.-J.; Tsai, F.-Y. Thin-Film Encapsulation of Polymer-Based Bulk-Heterojunction Photovoltaic Cells by Atomic Layer Deposition. *Org. Electron.* **2009**, *10*, 1300–1306.
- (34) Lu, J.; Elam, J. W.; Stair, P. C. Synthesis and Stabilization of Supported Metal Catalysts by Atomic Layer Deposition. *Acc. Chem. Res.* **2013**, *46*, 1806–1815.
- (35) Wegener, S. L.; Marks, T. J.; Stair, P. C. Design Strategies for the Molecular Level Synthesis of Supported Catalysts. *Acc. Chem. Res.* **2012**, *45*, 206–214.
- (36) Knez, M.; Kadri, A.; Wege, C.; Gösele, U.; Jeske, H.; K. Nielsch. Atomic Layer Deposition on Biological Macromolecules: Metal Oxide Coating of Tobacco Mosaic Virus and Ferritin. *Nano Lett.* **2006**, *6*, 1172–1177.
- (37) Bachmann, J.; Jing, J.; Knez, M.; Barth, S.; Shen, H.; Mathur, S.; Planck, M.; Physics, M.; Weinberg, A. Ordered Iron Oxide Nanotube Arrays of Controlled Geometry and Tunable Magnetism by Atomic Layer Deposition. *J. Am. Chem. Soc.* **2007**, *129*, 9554–9555.

- (38) Sander, M. S.; Côté, M. J.; Gu, W.; Kile, B. M.; Tripp, C. P. Template-Assisted Fabrication of Dense, Aligned Arrays of Titania Nanotubes with Well-Controlled Dimensions on Substrates. *Adv. Mater.* **2004**, *16*, 2052–2057.
- (39) Kolle, M.; Salgard-Cunha, P. M.; Scherer, M. R. J.; Huang, F.; Vukusic, P.; Mahajan, S.; Baumberg, J. J.; Steiner, U. Mimicking the Colourful Wing Scale Structure of the Papilio Blumei Butterfly. *Nat. Nanotechnol.* **2010**, *5*, 511–515.
- (40) Ahn, C.; Park, J.; Kim, D.; Jeon, S. Monolithic 3D Titania with Ultrathin Nanoshell Structures for Enhanced Photocatalytic Activity and Recyclability. *Nanoscale* **2013**, *5*, 10384–10389.
- (41) Malm, J.; Sahramo, E.; Karppinen, M.; Ras, R. H. A. Photo-Controlled Wettability Switching by Conformal Coating of Nanoscale Topographies with Ultrathin Oxide Films. *Chem. Mater.* **2010**, *22*, 3349–3352.
- (42) Werner, J. G.; Scherer, M. R. J.; Steiner, U.; Wiesner, U. Gyroidal Mesoporous Multifunctional Nanocomposites via Atomic Layer Deposition. *Nanoscale* **2014**, *6*, 8736–8742.
- (43) Wise, A. M.; Ban, C.; Weker, J. N.; Misra, S.; Cavanagh, A. S.; Wu, Z.; Li, Z.; Whittingham, M. S.; Xu, K.; George, S. M.; Toney, M. F. Effect of Al<sub>2</sub>O<sub>3</sub> Coating on Stabilizing LiNi<sub>0.4</sub>Mn<sub>0.4</sub>Co<sub>0.2</sub>O<sub>2</sub> Cathodes. *Chem. Mater.* **2015**, *27*, 6146–6154.
- (44) Hakim, L. F.; King, D. M.; Zhou, Y.; Gump, C. J.; George, S. M.; Weimer, A. W. Nanoparticle Coating for Advanced Optical, Mechanical and Rheological Properties. *Adv. Funct. Mater.* **2007**, *17*, 3175–3181.
- (45) Han, X.; Liu, Y.; Jia, Z.; Chen, Y.; Wan, J.; Weadock, N. Atomic-Layer-Deposition Oxide Nanoglue for Sodium Ion Batteries. *Nano Lett.* **2014**, *14*, 139–147.
- (46) Li, Y.; Sun, Y.; Xu, G.; Lu, Y.; Zhang, S.; Xue, L.; Jur, J. S.; Zhang, X. Tuning Electrochemical Performance of Si-Based Anodes for Lithium-Ion Batteries by Employing Atomic Layer Deposition Alumina Coating. *J. Mater. Chem. A* **2014**, *2*, 11417.
- (47) Li, X.; Liu, J.; Meng, X.; Tang, Y.; Banis, M. N.; Yang, J.; Hu, Y.; Li, R.; Cai, M.; Sun, X. Significant Impact on Cathode Performance of Lithium-Ion Batteries by Precisely Controlled Metal Oxide Nanocoatings via Atomic Layer Deposition. *J. Power Sources* **2014**, *247*, 57–69.
- (48) George, S. M. Atomic Layer Deposition: An Overview. *Chem. Rev.* **2010**, *110*, 111–131.
- (49) Sundberg, P.; Karppinen, M. Organic and Inorganic-Organic Thin Film Structures by Molecular Layer Deposition: A Review. *Beilstein J. Nanotechnol.* **2014**, *5*, 1104–1136.

- (50) Lee, B. H.; Yoon, B.; Abdulagatov, A. I.; Hall, R. a.; George, S. M. Growth and Properties of Hybrid Organic-Inorganic Metalcone Films Using Molecular Layer Deposition Techniques. *Adv. Funct. Mater.* **2013**, *23*, 532–546.
- (51) Du, Y.; George, S. M. Molecular Layer Deposition of Nylon 66 Films Examined Using in Situ FTIR Spectroscopy. *J. Phys. Chem. C* **2007**, *111*, 8509–8517.
- (52) Fu, Y.; Li, B.; Jiang, Y.; Dunphy, D. R.; Tsai, A.; Tam, S.; Fan, H.; Zhang, H.; Rogers, D.; Rempe, S.; Atanassov, P. C.; Joseph, L.; Brinker, C. J. Atomic Layer Deposition of L-Alanine Polypeptide. *J. Am. Chem. Soc.* **2014**, *136*, 15821–15824.
- (53) Adamczyk, N. M.; Dameron, A. A.; George, S. M. Molecular Layer Deposition of Poly(p-phenylene terephthalamide ) Films Using Terephthaloyl Chloride and p-phenylenediamine. *Langmuir* **2008**, *24*, 2081–2089.
- (54) Yoshimura, T.; Tatsuura, S.; Sotoyama, W. Polymer Films Formed with Monolayer Growth Steps by Molecular Layer Deposition. *Appl. Phys. Lett.* **1991**, *59*, 482.
- (55) Cho, S.; Han, G.; Kim, K.; Sung, M. M. High-Performance Two-Dimensional Polydiacetylene with a Hybrid Inorganic-Organic Structure. *Angew. Chem. Int. Ed.* **2011**, *50*, 2742–2746.
- (56) Liu, J.; Yoon, B.; Kuhlmann, E.; Tian, M.; Zhu, J.; George, S. M.; Lee, Y.; Yang, R. Ultralow Thermal Conductivity of Atomic/Molecular Layer-Deposited Hybrid Organic-Inorganic Zincone Thin Films. *Nano Lett.* **2013**, *13*, 5594–5599.
- (57) Yoon, B.; Lee, B. H.; George, S. M. Highly Conductive and Transparent Hybrid Organic-Inorganic Zincone Thin Films Using Atomic and Molecular Layer Deposition. *J. Phys. Chem. C* **2012**, *116*, 24784–24791.
- (58) Peng, Q.; Gong, B.; Vangundy, R. M.; Parsons, G. N. “Zincone” Zinc Oxide-Organic Hybrid Polymer Thin Films Formed by Molecular Layer Deposition. *Chem. Mater.* **2009**, *21*, 820–830.
- (59) Sood, A.; Sundberg, P.; Karppinen, M. ALD/MLD of Novel Layer-Engineered Zn-Based Inorganic-Organic Hybrid Thin Films Using Heterobifunctional 4-Aminophenol as an Organic Precursor. *Dalton Trans.* **2013**, *42*, 3869–3875.
- (60) Yoon, B.; Seghete, D.; Cavanagh, A. S.; George, S. M. Molecular Layer Deposition of Hybrid Organic–Inorganic Alucone Polymer Films Using a Three-Step ABC Reaction Sequence. *Chem. Mater.* **2009**, *21*, 5365–5374.
- (61) Jen, S.; George, S. M. Alucone Interlayers to Minimize Stress Caused by Thermal Expansion Mismatch between Al<sub>2</sub>O<sub>3</sub> Films and Te Fl on Substrates. *ACS Appl. Mater. Interfaces* **2013**, *5*, 1165–1173.

- (62) Lee, B. H.; Yoon, B.; Anderson, V. R.; George, S. M. Alucone Alloys with Tunable Properties Using Alucone Molecular Layer Deposition and Al<sub>2</sub>O<sub>3</sub> Atomic Layer Deposition. *J. Phys. Chem. C* **2012**, *116*, 3250–3257.
- (63) Sood, A.; Sundberg, P.; Malm, J.; Karppinen, M. Layer-by-Layer Deposition of Ti–4,4'-Oxydianiline Hybrid Thin Films. *Appl. Surf. Sci.* **2011**, *257*, 6435–6439.
- (64) Ishchuk, S.; Taffa, D. H.; Hazut, O.; Kaynan, N.; Yerushalmi, R. Transformation of Organic-Inorganic Hybrid Films Obtained by Molecular Layer Deposition to Photocatalytic Layers with Enhanced Activity. *ACS Nano* **2012**, 7263–7269.
- (65) Sarkar, D.; Taffa, D. H.; Ishchuk, S.; Hazut, O.; Cohen, H.; Toker, G.; Asscher, M.; Yerushalmi, R. Tailor-Made Oxide Architectures Attained by Molecularly Permeable Metal-Oxide Organic Hybrid Thin Films. *Chem. Commun.* **2014**, *50*, 9176–9178.
- (66) Lee, B. H.; Yoon, B.; Anderson, V. R.; George, S. M. Alucone Alloys with Tunable Properties Using Alucone Molecular Layer Deposition and Al<sub>2</sub>O<sub>3</sub> Atomic Layer Deposition. *J. Phys. Chem. C* **2012**, *116*, 3250–3257.
- (67) Abdulagatov, A. I.; Hall, R. A.; Sutherland, J. L.; Lee, B. H.; Cavanagh, A. S.; George, S. M. Molecular Layer Deposition of Titanicone Films Using TiCl<sub>4</sub> and Ethylene Glycol or Glycerol: Growth and Properties. *Chem. Mater.* **2012**, *24*, 2854–2864.
- (68) Sundberg, P.; Karppinen, M. Organic-Inorganic Thin Films from TiCl<sub>4</sub> and 4-Aminophenol Precursors: A Model Case of ALD/MLD Hybrid-Material Growth? *Eur. J. Inorg. Chem.* **2014**, *2014*, 968–974.
- (69) Chen, C.; Li, P.; Wang, G.; Yu, Y.; Duan, F.; Chen, C.; Song, W.; Qin, Y.; Knez, M. Nanoporous Nitrogen-Doped Titanium Dioxide with Excellent Photocatalytic Activity under Visible Light Irradiation Produced by Molecular Layer Deposition. *Angew. Chem. Int. Ed.* **2013**, *52*, 9196–9200.
- (70) Zhang, L.; Patil, A. J.; Li, L.; Schierhorn, A.; Mann, S.; Gösele, U.; Knez, M. Chemical Infiltration during Atomic Layer Deposition: Metallization of Porphyrins as Model Substrates. *Angew. Chem. Int. Ed.* **2009**, *48*, 4982–4985.
- (71) Gong, B.; Peng, Q.; Jur, J. S.; Devine, C. K.; Lee, K.; Parsons, G. N. Sequential Vapor Infiltration of Metal Oxides into Sacrificial Polyester Fibers: Shape Replication and Controlled Porosity of Microporous/Mesoporous Oxide Monoliths. **2011**, *23*, 3476–3485.
- (72) Lee, S.-M.; Pippel, E.; Gösele, U.; Dresbach, C.; Qin, Y.; Chandran, C. V.; Bräuniger, T.; Hause, G.; Knez, M. Greatly Increased Toughness of Infiltrated Spider Silk. *Science* **2009**, *324*, 488–492.

- 
- (73) Lee, S.-M.; Pippel, E.; Knez, M. Metal Infiltration into Biomaterials by ALD and CVD: A Comparative Study. *Chemphyschem* **2011**, *12*, 791–798.
- (74) Lee, S.-M.; Pippel, E.; Moutanabbir, O.; Gunkel, I.; Thurn-Albrecht, T.; Knez, M. Improved Mechanical Stability of Dried Collagen Membrane after Metal Infiltration. *ACS Appl. Mater. Interfaces* **2010**, *2*, 2436–2441.
- (75) Gregorczyk, K. E.; Pickup, D. F.; Sanz, M. G.; Irakulis, I. A.; Rogero, C.; Knez, M. Tuning the Tensile Strength of Cellulose through Vapor-Phase Metalation. *Chem. Mater.* **2015**, *27*, 181–188.
- (76) Lee, S.-M.; Ischenko, V.; Pippel, E.; Masic, A.; Moutanabbir, O.; Fratzl, P.; Knez, M. An Alternative Route Towards Metal-Polymer Hybrid Materials Prepared by Vapor-Phase Processing. *Adv. Funct. Mater.* **2011**, *21*, 3047–3055.
- (77) Terasaki, I.; Iwakawa, M.; Nakano, T.; Tsukudaa, A.; Kobayashi, W. Novel Thermoelectric Properties of Complex Transition-Metal Oxides. *Dalt. Trans.* **2010**, *39*, 1005–1011.
- (78) Yuan, C.; Wu, H. Bin; Xie, Y.; Lou, X. W. D. Mixed Transition-Metal Oxides: Design, Synthesis, and Energy-Related Applications. *Angew. Chem. Int. Ed.* **2014**, *53*, 1488–1504.
- (79) Meyer, J.; Hamwi, S.; Kröger, M.; Kowalsky, W.; Riedl, T.; Kahn, A. Transition Metal Oxides for Organic Electronics: Energetics, Device Physics and Applications. *Adv. Mater.* **2012**, *24*, 5408–5427.
- (80) Cheong, S.-W. Orbital Reconstruction and Covalent Bonding at an Oxide Interface. *Science* **2007**, *318*, 927–928.
- (81) Hussain, M. Synthesis, Characterization and Applications of Metal Oxide, Linköping University, 2014.
- (82) Hofstetter, D.; Morkoc, H. ZnO Devices and Applications: A Review of Current Status and Future Prospects. *Proc. I.E.E.E.* **2010**, *98*, 1255–1268.
- (83) Sang, L.; Liao, M.; Sumiya, M. A Comprehensive Review of Semiconductor Ultraviolet Photodetectors: from Thin Film to One-Dimensional Nanostructures. *Sensors* **2013**, *13*, 10482–10518.
- (84) Pearton, S.; Ren, F. Advances in ZnO-Based Materials for Light Emitting Diodes. *Curr. Opin. Chem. Eng.* **2014**, *3*, 51–55.
- (85) Wang, Z. L.; Song, J. Piezoelectric Nanogenerators Based on Zinc Oxide Nanowire Arrays. *Science* **2006**, *312*, 242–245.
- (86) Wang, Z. L.; Wu, W. Nanotechnology-Enabled Energy Harvesting for Self-Powered Micro-/nanosystems. *Angew. Chem. Int. Ed.* **2012**, *51*, 11700–11721.

- (87) Kumar, B.; Kim, S.-W. Energy Harvesting Based on Semiconducting Piezoelectric ZnO Nanostructures. *Nano Energy* **2012**, *1*, 342–355.
- (88) Weiss, N. O.; Zhou, H.; Liao, L.; Liu, Y.; Jiang, S.; Huang, Y.; Duan, X. Graphene: An Emerging Electronic Material. *Adv. Mater.* **2012**, *24*, 5782–5825.
- (89) Choi, H.-J.; Jung, S.-M.; Seo, J.-M.; Chang, D. W.; Dai, L.; Baek, J.-B. Graphene for Energy Conversion and Storage in Fuel Cells and Supercapacitors. *Nano Energy* **2012**, *1*, 534–551.
- (90) Tan, Y. Bin; Lee, J.-M. Graphene for Supercapacitor Applications. *J. Mater. Chem. A* **2013**, *1*, 14814–14843.
- (91) Zhang, L. L.; Zhou, R.; Zhao, X. S. Graphene-Based Materials as Supercapacitor Electrodes. *J. Mater. Chem.* **2010**, *20*, 5983–5992.
- (92) Kim, S. J.; Choi, K.; Lee, B.; Kim, Y.; Hong, B. H. Materials for Flexible, Stretchable Electronics: Graphene and 2D Materials. *Annu. Rev. Mater. Res.* **2014**, *45*, 16.1–16.22.
- (93) Xie, G.; Zhang, K.; Guo, B.; Liu, Q.; Fang, L.; Gong, J. R. Graphene-Based Materials for Hydrogen Generation from Light-Driven Water Splitting. *Adv. Mater.* **2013**, *25*, 3820–3839.
- (94) Zhang, Y. I.; Zhang, L.; Zhou, C. Review of Chemical Vapor Deposition of Graphene and Related Applications. *Acc. Chem. Res.* **2013**, *46*, 2329–2339.
- (95) Zhu, Y.; Murali, S.; Cai, W.; Li, X.; Suk, J. W.; Potts, J. R.; Ruoff, R. S. Graphene and Graphene Oxide: Synthesis, Properties, and Applications. *Adv. Mater.* **2010**, *22*, 3906–3924.
- (96) Beidaghi, M.; Gogotsi, Y. Capacitive Energy Storage in Micro-Scale Devices: Recent Advances in Design and Fabrication of Micro-Supercapacitors. *Energy Environ. Sci.* **2014**, *7*, 867–884.
- (97) Zhang, Q.; Uchaker, E.; Candelaria, S. L.; Cao, G. Nanomaterials for Energy Conversion and Storage. *Chem. Soc. Rev.* **2013**, *42*, 3127–3171.
- (98) Zhi, M.; Xiang, C.; Li, J.; Li, M.; Wu, N. Nanostructured Carbon-Metal Oxide Composite Electrodes for Supercapacitors: A Review. *Nanoscale* **2013**, *5*, 72–88.
- (99) Simon, P.; Gogotsi, Y. Materials for Electrochemical Capacitors. *Nat. Mater.* **2008**, *7*, 845–854.
- (100) Wang, S.; Dryfe, R. a. W. Graphene Oxide-Assisted Deposition of Carbon Nanotubes on Carbon Cloth as Advanced Binder-Free Electrodes for Flexible Supercapacitors. *J. Mater. Chem. A* **2013**, *1*, 5279–5283.

- (101) Wang, Y.; Shi, Z.; Huang, Y.; Ma, Y.; Wang, C.; Chen, M.; Chen, Y. Supercapacitor Devices Based on Graphene Materials. *J. Phys. Chem. C* **2009**, *113*, 13103–13107.
- (102) Liu, C.; Yu, Z.; Neff, D.; Zhamu, A.; Jang, B. Z. Graphene-Based Supercapacitor with an Ultrahigh Energy Density. *Nano Lett.* **2010**, *10*, 4863–4868.
- (103) Yu, G.; Hu, L.; Liu, N.; Wang, H.; Vosgueritchian, M.; Yang, Y.; Cui, Y.; Bao, Z. Enhancing the Supercapacitor Performance of graphene/MnO<sub>2</sub> Nanostructured Electrodes by Conductive Wrapping. *Nano Lett.* **2011**, *11*, 4438–4442.
- (104) Mitra, S.; Lokesh, K. S.; Sampath, S. Exfoliated Graphite–ruthenium Oxide Composite Electrodes for Electrochemical Supercapacitors. *J. Power Sources* **2008**, *185*, 1544–1549.
- (105) Wu, Z.-S.; Wang, D.-W.; Ren, W.; Zhao, J.; Zhou, G.; Li, F.; Cheng, H.-M. Anchoring Hydrous RuO<sub>2</sub> on Graphene Sheets for High-Performance Electrochemical Capacitors. *Adv. Funct. Mater.* **2010**, *20*, 3595–3602.
- (106) Zhang, C.; Zhou, H.; Yu, X.; Shan, D.; Ye, T.; Huang, Z.; Kuang, Y. Synthesis of RuO<sub>2</sub> Decorated Quasi Graphene Nanosheets and Their Application in Supercapacitors. *RSC Adv.* **2014**, *4*, 11197–11205.
- (107) Knez, M.; Nielsch, K.; Niinistö, L. Synthesis and Surface Engineering of Complex Nanostructures by Atomic Layer Deposition. *Adv. Mater.* **2007**, *19*, 3425–3438.
- (108) Conway, B. E. *Electrochemical Supercapacitor: Scientific Fundamentals and Technological Applications*; Kluwer Academic/Plenum Publishers, New York, 1999.
- (109) Kim, W.; Park, S.; Kim, D. Y.; Kim, H. Atomic Layer Deposition of Ruthenium and Ruthenium-Oxide Thin Films by Using a Ru(EtCp)<sub>2</sub> Precursor and Oxygen Gas. *J. Korean Phys. Soc.* **2009**, *55*, 32–37.
- (110) Yim, S.-S.; Lee, D.-J.; Kim, K.-S.; Kim, S.-H.; Yoon, T.-S.; Kim, K.-B. Nucleation Kinetics of Ru on Silicon Oxide and Silicon Nitride Surfaces Deposited by Atomic Layer Deposition. *J. Appl. Phys.* **2008**, *103*, 113509.
- (111) Kwon, O.-K.; Kim, J.-H.; Park, H.-S.; Kang, S.-W. Atomic Layer Deposition of Ruthenium Thin Films for Copper Glue Layer. *J. Electrochem. Soc.* **2004**, *151*, G109–G112.
- (112) Park, S.-J.; Kim, W.-H.; Lee, H.-B.-R.; Maeng, W. J.; Kim, H. Thermal and Plasma Enhanced Atomic Layer Deposition Ruthenium and Electrical Characterization as a Metal Electrode. *Microelectron. Eng.* **2008**, *85*, 39–44.

- (113) Hong, T. E.; Choi, S.-H.; Yeo, S.; Park, J.-Y.; Kim, S.-H.; Cheon, T.; Kim, H.; Kim, M.-K. Atomic Layer Deposition of Ru Thin Films Using a Ru(0) Metallorganic Precursor and O<sub>2</sub>. *ECS J. Solid State Sci. Technol.* **2012**, *2*, P47–P53.
- (114) Tong, X.; Qin, Y.; Guo, X.; Moutanabbir, O.; Ao, X.; Pippel, E.; Zhang, L.; Knez, M. Enhanced Catalytic Activity for Methanol Electro-Oxidation of Uniformly Dispersed Nickel Oxide Nanoparticles-Carbon Nanotube Hybrid Materials. *Small* **2012**, *8*, 3390–3395.
- (115) Puurunen, R. L.; Vandervorst, W. Island Growth as a Growth Mode in Atomic Layer Deposition: A Phenomenological Model. *J. Appl. Phys.* **2004**, *96*, 7686–7695.
- (116) Chen, Y. M.; Korotcov, A.; Hsu, H. P.; Huang, Y. S.; Tsai, D. S. Raman Scattering Characterization of Well-Aligned RuO<sub>2</sub> Nanocrystals Grown on Sapphire Substrates. *New J. Phys.* **2007**, *9*, 130–130.
- (117) Ryan, J. V.; Berry, A. D.; Anderson, M. L.; Long, J. W.; Stroud, R. M.; Cepak, V. M.; Browning, V. M.; Rolison, D. R.; Merzbacher, C. I. Electronic Connection to the Interior of A Mesoporous Insulator with Nanowires of Crystalline RuO<sub>2</sub>. *Nature* **2000**, *406*, 169–172.
- (118) Hudec, B.; Hušeková, K.; Rosová, A.; Šoltýs, J.; Rammula, R.; Kasikov, A.; Uustare, T.; Mičušík, M.; Omastová, M.; Aarik, J.; Fröhlich, K. Impact of Plasma Treatment on Electrical Properties of TiO<sub>2</sub>/RuO<sub>2</sub> Based DRAM Capacitor. *J. Phys. D. Appl. Phys.* **2013**, *46*, 385304.
- (119) Wang, W.; Guo, S.; Lee, I.; Ahmed, K.; Zhong, J.; Favors, Z.; Zaera, F.; Ozkan, M.; Ozkan, C. S. Hydrous Ruthenium Oxide Nanoparticles Anchored to Graphene and Carbon Nanotube Hybrid Foam for Supercapacitors. *Sci. Rep.* **2014**, *4*, 4452–4460.
- (120) Bagri, A.; Mattevi, C.; Acik, M.; Chabal, Y. J.; Chhowalla, M.; Shenoy, V. B. Structural Evolution during the Reduction of Chemically Derived Graphene Oxide. *Nat. Chem.* **2010**, *2*, 581–587.
- (121) Zhang, J.; Liu, X.; Blume, R.; Zhang, A.; Schlögl, R.; Su, D. S. Surface-Modified Carbon Nanotubes Catalyze Oxidative Dehydrogenation of n-Butane. *Science* **2007**, *322*, 73–77.
- (122) Tang, L.; Li, X.; Ji, R.; Teng, K. S.; Tai, G.; Ye, J.; Wei, C.; Lau, S. P. Bottom-up Synthesis of Large-Scale Graphene Oxide Nanosheets. *J. Mater. Chem.* **2012**, *22*, 5676–5683.
- (123) Kim, K.; Lee, H.-B.-R.; Johnson, R. W.; Tanskanen, J. T.; Liu, N.; Kim, M.-G.; Pang, C.; Ahn, C.; Bent, S. F.; Bao, Z. Selective Metal Deposition at Graphene Line Defects by Atomic Layer Deposition. *Nat. Commun.* **2014**, *5*, 4781.

- (124) Han, J. T.; Jeong, B. H.; Seo, S. H.; Roh, K. C.; Kim, S.; Choi, S.; Woo, J. S.; Kim, H. Y.; Jang, J. I.; Shin, D.-C.; *et al.* Dispersant-Free Conducting Pastes for Flexible and Printed Nanocarbon Electrodes. *Nat. Commun.* **2013**, *4*, 2491–2498.
- (125) Hu, C.-C.; Chen, W.-C. Effects of Substrates on the Capacitive Performance of  $\text{RuO}_x \cdot n\text{H}_2\text{O}$  and Activated carbon– $\text{RuO}_x$  Electrodes for Supercapacitors. *Electrochim. Acta* **2004**, *49*, 3469–3477.
- (126) Chen, L. Y.; Hou, Y.; Kang, J. L.; Hirata, A.; Fujita, T.; Chen, M. W. Toward the Theoretical Capacitance of  $\text{RuO}_2$  Reinforced by Highly Conductive Nanoporous Gold. *Adv. Energy Mater.* **2013**, *3*, 851–856.
- (127) Soin, N.; Roy, S. S.; Mitra, S. K.; Thundat, T.; McLaughlin, J. A. Nanocrystalline Ruthenium Oxide Dispersed Few Layered Graphene (FLG) Nanoflakes as Supercapacitor Electrodes. *J. Mater. Chem.* **2012**, *22*, 14944–14950.
- (128) Lang, X.; Hirata, A.; Fujita, T.; Chen, M. Nanoporous Metal/oxide Hybrid Electrodes for Electrochemical Supercapacitors. *Nat. Nanotechnol.* **2011**, *6*, 232–236.
- (129) Hu, C.-C.; Chen, W.-C.; Chang, K.-H. How to Achieve Maximum Utilization of Hydrous Ruthenium Oxide for Supercapacitors. *J. Electrochem. Soc.* **2004**, *151*, A281–A290.
- (130) Rabis, A.; Rodriguez, P.; Schmidt, T. J. Electrocatalysis for Polymer Electrolyte Fuel Cells: Recent Achievements and Future Challenges. *ACS Catal.* **2012**, *2*, 864–890.
- (131) Zhang, S.; Shao, Y.; Yin, G.; Lin, Y. Recent Progress in Nanostructured Electrocatalysts for PEM Fuel Cells. *J. Mater. Chem. A* **2013**, *1*, 4631–4641.
- (132) Katsounaros, I.; Cherevko, S.; Zeradjanin, A. R.; Mayrhofer, K. J. J. Oxygen Electrochemistry as a Cornerstone for Sustainable Energy Conversion. *Angew. Chem. Int. Ed.* **2014**, *53*, 102–121.
- (133) Stephens, I. E. L.; Bondarenko, A. S.; Grønbjerg, U.; Rossmeisl, J.; Chorkendorff, I. Understanding the Electrocatalysis of Oxygen Reduction on Platinum and Its Alloys. *Energy Environ. Sci.* **2012**, *5*, 6744–6762.
- (134) Guo, S.; Zhang, S.; Sun, S. Tuning Nanoparticle Catalysis for the Oxygen Reduction Reaction. *Angew. Chem. Int. Ed.* **2013**, *52*, 8526–8544.
- (135) Wu, J.; Yang, H. Platinum-Based Oxygen Reduction Electrocatalysts. *Acc. Chem. Res.* **2013**, *46*, 1848–1857.
- (136) Wei, J.; Hu, Y.; Liang, Y.; Kong, B.; Zhang, J.; Song, J.; Bao, Q.; Simon, G. P.; Jiang, S. P.; Wang, H. Nitrogen-Doped Nanoporous Carbon/Graphene

- Nano-Sandwiches: Synthesis and Application for Efficient Oxygen Reduction. *Adv. Funct. Mater.* **2015**, *25*, 5768–5777.
- (137) Yasuda, S.; Furuya, A.; Uchibori, Y.; Kim, J.; Murakoshi, K. Iron-Nitrogen-Doped Vertically Aligned Carbon Nanotube Electrocatalyst for the Oxygen Reduction Reaction. *Adv. Funct. Mater.* **2016**, *26*, 738–744.
- (138) Wang, D.-W.; Su, D. Heterogeneous Nanocarbon Materials for Oxygen Reduction Reaction. *Energy Environ. Sci.* **2014**, *7*, 576–591.
- (139) Zhou, X.; Qiao, J.; Yang, L.; Zhang, J. A Review of Graphene-Based Nanostructural Materials for Both Catalyst Supports and Metal-Free Catalysts in PEM Fuel Cell Oxygen Reduction Reactions. *Adv. Energy Mater.* **2014**, *4*, 1301523.
- (140) Wu, Z.; Yang, S.; Sun, Y.; Parvez, K.; Feng, X.; Müllen, K. 3D Nitrogen-Doped Graphene Aerogel-Supported Fe<sub>3</sub>O<sub>4</sub> Nanoparticles as Efficient Electrocatalysts for the Oxygen Reduction Reaction. *J. Am. Chem. Soc.* **2012**, *134*, 9082–9085.
- (141) Liang, Y.; Li, Y.; Wang, H.; Zhou, J.; Wang, J.; Regier, T.; Dai, H. Co<sub>3</sub>O<sub>4</sub> Nanocrystals on Graphene as a Synergistic Catalyst for Oxygen Reduction Reaction. *Nat. Mater.* **2011**, *10*, 780–786.
- (142) Liang, Y.; Wang, H.; Diao, P.; Chang, W.; Hong, G.; Li, Y.; Gong, M.; Xie, L.; Zhou, J.; Wang, J.; Regier, T. Z.; Wei, F.; Dai, H. Oxygen Reduction Electrocatalyst Based on Strongly Coupled Cobalt Oxide Nanocrystals and Carbon Nanotubes. *J. Am. Chem. Soc.* **2012**, *134*, 15849–15857.
- (143) Duan, J.; Chen, S.; Dai, S.; Qiao, S. Z. Shape Control of Mn<sub>3</sub>O<sub>4</sub> Nanoparticles on Nitrogen-Doped Graphene for Enhanced Oxygen Reduction Activity. *Adv. Funct. Mater.* **2014**, *24*, 2072–2078.
- (144) Zhang, T.; Cheng, F.; Du, J.; Hu, Y.; Chen, J. Efficiently Enhancing Oxygen Reduction Electrocatalytic Activity of MnO<sub>2</sub> Using Facile Hydrogenation. *Adv. Energy Mater.* **2015**, *5*, 1400654.
- (145) Sun, M.; Dong, Y.; Zhang, G.; Qu, J.; Li, J. A-Fe<sub>2</sub>O<sub>3</sub> Spherical Nanocrystals Supported on CNTs as Efficient Non-Noble Electrocatalysts for the Oxygen Reduction Reaction. *J. Mater. Chem. A* **2014**, *2*, 13635–13640.
- (146) Zhang, G.; Xia, B. Y.; Wang, X.; David Lou, X. W. Strongly Coupled NiCo<sub>2</sub>O<sub>4</sub>-rGO Hybrid Nanosheets as a Methanol-Tolerant Electrocatalyst for the Oxygen Reduction Reaction. *Adv. Mater.* **2014**, *26*, 2408–2412.
- (147) Banham, D.; Ye, S.; Pei, K.; Ozaki, J.; Kishimoto, T.; Imashiro, Y. A Review of the Stability and Durability of Non-Precious Metal Catalysts for the Oxygen Reduction Reaction in Proton Exchange Membrane Fuel Cells. *J. Power Sources* **2015**, *285*, 334–348.

- (148) Yang, F.; Zhang, L.; Zuzuarregui, A.; Gregorczyk, K.; Li, L.; Beltrán, M.; Tollan, C.; Brede, J.; Rogero, C.; Chuvilin, A.; Knez, M. Functionalization of Defect Sites in Graphene with RuO<sub>2</sub> for High Capacitive Performance. *ACS Appl. Mater. Interfaces* **2015**, *7*, 20513–20519.
- (149) Lee, H.; Dellatore, S. M.; Miller, W. M.; Messersmith, P. B. Mussel-Inspired Surface Chemistry for Multifunctional Coatings. *Science* **2007**, *318*, 426–430.
- (150) Fei, B.; Qian, B.; Yang, Z.; Wang, R.; Liu, W. C.; Mak, C. L.; Xin, J. H. Coating Carbon Nanotubes by Spontaneous Oxidative Polymerization of Dopamine. *Carbon* **2008**, *46*, 1795–1797.
- (151) Liu, Y.; Ai, K.; Lu, L. Polydopamine and Its Derivative Materials: Synthesis and Promising Applications in Energy, Environmental, and Biomedical Fields. *Chem. Rev.* **2014**, *114*, 5057–5115.
- (152) Malecki, A.; Doumerc, J. P. Kinetics of Thermal Decomposition of Co<sub>3</sub>O<sub>4</sub> Powder and Single Crystals. *J. Solid State Chem.* **1985**, *57*, 49–57.
- (153) Malecki, A.; Doumerc, J. P. Kinetics of Thermal Decomposition of Co<sub>3</sub>O<sub>4</sub> the Kinetic Model. *J. Therm. Anal.* **1990**, *36*, 215–222.
- (154) Toniolo, J. C.; Takimi, A. S.; Bergmann, C. P. Nanostructured Cobalt Oxides (Co<sub>3</sub>O<sub>4</sub> and CoO) and Metallic Co Powders Synthesized by the Solution Combustion Method. *Mater. Res. Bull.* **2010**, *45*, 672–676.
- (155) Petitto, S. C.; Marsh, E. M.; Carson, G. A.; Langell, M. A. Cobalt Oxide Surface Chemistry: The Interaction of CoO(100), Co<sub>3</sub>O<sub>4</sub>(110) and Co<sub>3</sub>O<sub>4</sub>(111) with Oxygen and Water. *J. Mol. Catal. A Chem.* **2008**, *281*, 49–58.
- (156) Cui, J.; Zhang, X.; Tong, L.; Luo, J.; Wang, Y.; Zhang, Y.; Xie, K.; Wu, Y. Facile Synthesis of Mesoporous Co<sub>3</sub>O<sub>4</sub>/CeO<sub>2</sub> Hybrid Nanowire Arrays for High Performance Supercapacitors. *J. Mater. Chem. A* **2015**, *3*, 10426–10431.
- (157) Qiao, L.; Xiao, H. Y.; Meyer, H. M.; Sun, J. N.; Rouleau, C. M.; Paretzky, A. A.; Geohagan, D. B.; Ivanov, I. N.; Yoon, M.; Weber, W. J.; Biegalski, M. D. Nature of the Band Gap and Origin of the Electro-/photo-Activity of Co<sub>3</sub>O<sub>4</sub>. *J. Mater. Chem. C* **2013**, *1*, 4628–4633.
- (158) Wu, G.; More, K. L.; Johnston, C. M.; Zelenay, P. High-Performance Electrocatalysts for Oxygen Reduction Derived from Polyaniline, Iron, and Cobalt. *Science* **2011**, *332*, 443–447.
- (159) Bashyam, R.; Zelenay, P. A Class of Non-Precious Metal Composite Catalysts for Fuel Cells. *Nature* **2006**, *443*, 63–66.
- (160) Chao, S.; Cui, Q.; Bai, Z.; Yan, H.; Wang, K.; Yang, L. Varying N Content and N/C Ratio of the Nitrogen Precursor to Synthesize Highly Active Co-N<sub>x</sub>/C Non-Precious Metal Catalyst. *Int. J. Hydrogen Energy* **2014**, *39*, 14768–14776.

- (161) Xiao, M.; Zhu, J.; Feng, L.; Liu, C.; Xing, W. Meso/macroporous Nitrogen-Doped Carbon Architectures with Iron Carbide Encapsulated in Graphitic Layers as an Efficient and Robust Catalyst for the Oxygen Reduction Reaction in Both Acidic and Alkaline Solutions. *Adv. Mater.* **2015**, *27*, 2521–2527.
- (162) Chang, Y.; Hong, F.; He, C.; Zhang, Q.; Liu, J. Nitrogen and Sulfur Dual-Doped Non-Noble Catalyst Using Fluidic Acrylonitrile Telomer as Precursor for Efficient Oxygen Reduction. *Adv. Mater.* **2013**, *25*, 4794–4799.
- (163) Wang, L.; Yin, J.; Zhao, L.; Tian, C.; Yu, P.; Wang, J.; Fu, H. Ion-Exchanged Route Synthesis of Fe<sub>2</sub>N-N-Doped Graphitic Nanocarbons Composite as Advanced Oxygen Reduction Electrocatalyst. *Chem. Commun.* **2013**, *49*, 3022–3024.
- (164) Aijaz, A.; Masa, J.; Rösler, C.; Xia, W.; Weide, P.; Botz, A. J. R.; Fischer, R. A.; Schuhmann, W.; Muhler, M. Co@Co<sub>3</sub>O<sub>4</sub> Encapsulated in Carbon Nanotube-Grafted Nitrogen-Doped Carbon Polyhedra as an Advanced Bifunctional Oxygen Electrode. *Angew. Chem. Int. Ed.* **2016**, *55*, 4087–4091.
- (165) Masa, J.; Xia, W.; Sinev, I.; Zhao, A.; Sun, Z.; Grütze, S.; Weide, P.; Muhler, M.; Schuhmann, W. Mn<sub>x</sub>O<sub>y</sub>/NC and Co<sub>x</sub>O<sub>y</sub>/NC Nanoparticles Embedded in a Nitrogen-Doped Carbon Matrix for High-Performance Bifunctional Oxygen Electrodes. *Angew. Chem. Int. Ed.* **2014**, *53*, 8508–8512.
- (166) Guo, D.; Shibuya, R.; Akiba, C.; Saji, S.; Kondo, T.; Nakamura, J. Active Sites of Nitrogen-Doped Carbon Materials for Oxygen Reduction Reaction Clarified Using Model Catalysts. *Science* **2016**, *351*, 361–366.
- (167) Sanchez, C.; Julián, B.; Belleville, P.; Popall, M. Applications of Hybrid Organic-inorganic Nanocomposites. *J. Mater. Chem.* **2005**, *15*, 3559–3592.
- (168) Gregorczyk, K.; Knez, M. Hybrid Nanomaterials through Molecular and Atomic Layer Deposition: Top Down, Bottom Up, and in-between Approaches to New Materials. *Prog. Mater. Sci.* **2016**, *75*, 1–37.
- (169) Lee, B. H.; Anderson, V. R.; George, S. M. Molecular Layer Deposition of Zirconium and ZrO<sub>2</sub>/Zirconium Alloy Films: Growth and Properties. *Chem. Vap. Depos.* **2013**, *19*, 204–212.
- (170) Lee, B. H.; Anderson, V. R.; George, S. M. Growth and Properties of Hafnium and HfO<sub>2</sub>/Hafnium Nanolaminate and Alloy Films Using Molecular Layer Deposition Techniques. *ACS Appl. Mater. Interfaces* **2014**, *6*, 16880–16887.
- (171) Tian, F.; Cui, Y.; Teplyakov, A. V. Nitroxidation of H-Terminated Si (111) Surfaces with Nitrobenzene and Nitrosobenzene. *J. Phys. Chem. C* **2014**, *118*, 502–512.
- (172) Kobayashi, T.; Nagakura, S. Photoelectron Spectra of Anilines. *Chem. Lett.* **1972**, *1*, 1013–1017.

- (173) Leftwich, T. R.; Teplyakov, A. V. Calibration of Computationally Predicted N 1s Binding Energies by Comparison with X-Ray Photoelectron Spectroscopy Measurements. *J. Electron Spectros. Relat. Phenomena* **2009**, *175*, 31–40.
- (174) Sholl, D.; Steckel, J. A. *Density Functional Theory: A Practical Introduction*; JohnWiley & Sons, Inc.: New Jersey, 2002.
- (175) Furche, F.; Ahlrichs, R.; Hättig, C.; Klopper, W.; Sierka, M.; Weigend, F. Turbomole. *Wiley Interdiscip. Rev. Comput. Mol. Sci.* **2014**, *4*, 91–100.
- (176) Ahlrichs, R. Efficient Evaluation of Three-Center Two-Electron Integrals over Gaussian Functions. *Phys. Chem. Chem. Phys.* **2004**, *6*, 5119–5121.
- (177) Weigend, F. Accurate Coulomb-Fitting Basis Sets for H to Rn. *Phys. Chem. Chem. Phys.* **2006**, *8*, 1057-1065.
- (178) Peng, C.; Ayala, P. Y.; Schlegel, H. B.; Frisch, M. J. Using Redundant Internal Coordinates to Optimize Equilibrium Geometries and Transition States. *J. Comput. Chem.* **1996**, *17*, 49–56.
- (179) Akhter, S.; Zhou, X.-L.; White, J. M. XPS Study of Polymer/organometallic Interaction: Trimethyl Aluminum on Polyvinyl Alcohol Polymer. *Appl. Surf. Sci.* **1989**, *37*, 201–216.
- (180) Strongin, D. R.; Moore, J. F.; Ruckman, M. W. Synchrotron Radiation Assisted Deposition of Aluminum Oxide from Condensed Layers of Trimethylaluminum and Water at 78 K. *Appl. Phys. Lett.* **1992**, *61*, 729–731.
- (181) Detwiler, M. D.; Gharachorlou, A.; Mayr, L.; Gu, X.-K.; Liu, B.; Greeley, J.; Delgass, W. N.; Ribeiro, F. H.; Zemlyanov, D. Y. Reaction of Trimethylaluminum with Water on Pt (111) and Pd (111) from  $10^{-5}$  to  $10^{-1}$  Millibar. *J. Phys. Chem. C* **2015**, *119*, 2399-2411.
- (182) Ågren, H.; Roos, B. O.; Bagus, P. S.; Gelius, U.; Malmquist, P.; Svensson, S.; Maripuu, R.; Siegbahn, K. Multiple Excitations and Charge Transfer in the ESCA N1s (NO<sub>2</sub>) Spectrum of Paranitroaniline. A Theoretical and Experimental Study. *J. Chem. Phys.* **1982**, *77*, 3893–3901.
- (183) Banna, M. S. The Gas Phase X-Ray Photoelectron Spectrum of Para-Nitroaniline. *Chem. Phys.* **1980**, *45*, 383–385.
- (184) Roodenko, K.; Gensch, M.; Rappich, J.; Hinrichs, K.; Esser, N.; Hunger, R.; Elektronen-synchrotron, D.; Berlin, H. Time-Resolved Synchrotron XPS Monitoring of Irradiation-Induced Nitrobenzene Reduction for Chemical Lithography. *J. Phys. Chem. B* **2007**, *111*, 7541–7549.
- (185) Widjaja, Y.; Musgrave, C. B. Quantum Chemical Study of the Mechanism of Aluminum Oxide Atomic Layer Deposition. *Appl. Phys. Lett.* **2002**, *80*, 3304–3306.

- (186) Nguyen, H. M. T.; Tang, H.-Y.; Huang, W.-F.; Lin, M. C. Mechanisms for Reactions of Trimethylaluminum with Molecular Oxygen and Water. *Comput. Theor. Chem.* **2014**, *1035*, 39–43.
- (187) Puurunen, R. L. Surface Chemistry of Atomic Layer Deposition: A Case Study for the Trimethylaluminum/water Process. *J. Appl. Phys.* **2005**, *97*, 121301.
- (188) Liu, X.; Ramanathan, S.; Lee, E.; Seidel, T. E. Atomic Layer Deposition of Aluminum Nitride Thin Films from Trimethyl Aluminum (TMA) and Ammonia. *Mater. Res. Soc. symponisum Proc.* **2004**, *811*, D1.9.1–D1.9.6.
- (189) Goerke, S.; Ziegler, M.; Ihring, A.; Dellith, J.; Undisz, A.; Diegel, M.; Anders, S.; Huebner, U.; Rettenmayr, M.; Meyer, H.-G. Atomic Layer Deposition of AlN for Thin Membranes Using Trimethylaluminum and H<sub>2</sub>/N<sub>2</sub> Plasma. *Appl. Surf. Sci.* **2015**, *338*, 35–41.
- (190) Bosund, M.; Sajavaara, T.; Laitinen, M.; Huhtio, T.; Putkonen, M.; Airaksinen, V.-M.; Lipsanen, H. Properties of AlN Grown by Plasma Enhanced Atomic Layer Deposition. *Appl. Surf. Sci.* **2011**, *257*, 7827–7830.
- (191) Distefano, G.; Guerra, M.; Colonna, F. P.; Jones, D. Intense Shake-up Satellites in the XPS Spectra of Planar and Sterically Hindered N-Piperidyl-Nitrobenzenes and -Nitrothiophens. *Chem. Phys.* **1982**, *72*, 267–279.
- (192) Katrib, A.; El-Rayyes, N. R. Shake-up Energy in P-Nitroaniline Derivatwes. *Chem. Phys.* **1981**, *59*, 443–447.
- (193) Scientific, E.; Company, P.; Nakagaki, R.; Frost, D. C.; Mcdowell, C. A. Share-up Satellites in the Nitro N 1s Spectra of Highly Polar Nitro-Aromatic Amines. *J. Electron Spectros. Relat. Phenomena* **1982**, *27*, 69–73.
- (194) Guerra, M.; Jones, D.; Colonna, F. P.; Distefano, G. Decrease of the XPS Shake-up Intensity on Going from Paranitroaniline to Nitro-Amino Azabenzenes. *Chem. Phys. Lett.* **1983**, *98*, 522–526.
- (195) Distefano, G.; Guerra, M.; Jones, D.; Modelli, A.; Colonna, F. P. Experimental and Theoretical Study of Intense Shake-up Structures in the XPS Spectra of Nitrobenzenes and Nitrosobenzenes. *Chem. Phys.* **1980**, *52*, 389–398.
- (196) Pignataro, S.; Marino, R. Di; Distefano, G. Steric Inhibition of Resonance in Nitroanilines by ESCA. *J. Electron Spectros. Relat. Phenomena* **1974**, *4*, 90–92.
- (197) Nilsen, O.; Klepper, K. B.; Nielsen, H. Ø.; Fjellvåg, H. Deposition of Organic-Inorganic Hybrid Materials by Atomic Layer Deposition. *ECS Trans.* **2008**, *16*, 3–14.
- (198) Nilsen, O.; Fjellvåg, H. Measuring the Heat Evolved from Individual Reaction Steps in Atomic Layer Deposition. *J. Therm. Anal. Calorim.* **2011**, *105*, 33–37.

- 
- (199) Tynell, T.; Terasaki, I.; Yamauchi, H.; Karppinen, M. Thermoelectric Characteristics of (Zn,Al)O/hydroquinone Superlattices. *J. Mater. Chem. A* **2013**, *1*, 13619-13624.
- (200) Zhou, W.; Leem, J.; Park, I.; Li, Y.; Jin, Z.; Min, Y.-S. Charge Trapping Behavior in Organic–inorganic Alloy Films Grown by Molecular Layer Deposition from Trimethylaluminum, P-Phenylenediamine and Water. *J. Mater. Chem.* **2012**, *22*, 23935-23943.
- (201) Farmer, D. B.; Gordon, R. G. ALD of High-k Dielectrics on Suspended Functionalized SWNTs. *Electrochem. Solid-State Lett.* **2005**, *8*, G89-G91.
- (202) Cavanagh, A. S.; Wilson, C. a; Weimer, A. W.; George, S. M. Atomic Layer Deposition on Gram Quantities of Multi-Walled Carbon Nanotubes. *Nanotechnology* **2009**, *20*, 255602.
- (203) Farmer, D. B.; Gordon, R. G. Atomic Layer Deposition on Suspended Single-Walled Carbon Nanotubes via Gas-Phase Noncovalent Functionalization. *Nano Lett.* **2006**, *6*, 699–703.
- (204) Wang, X.; Tabakman, S. M.; Dai, H. Atomic Layer Deposition of Metal Oxides on Pristine and Functionalized Graphene. *J. Am. Chem. Soc.* **2008**, *130*, 8152–8153.



---

## List of publications

1. **Fan Yang**, Lianbing Zhang, Ana Zuzuarregui, Keith Gregorczyk, Le Li, Mikel Beltrán, Christopher Tollan, Jens Brede, Celia Rogero, Andrey Chuvilin, Mato Knez, Functionalization of Defect Sites in Graphene with RuO<sub>2</sub> for High Capacitive Performance. *ACS Applied Materials & Interfaces*. 2015, **7**, 20513–20519.
2. **Fan Yang**, Mikel Abadia, Weike Wang, Chaoqiu Chen, Le Li, Lianbing Zhang, Celia Rogero, Andrey Chuvilin, Mato Knez, Design of Oxygen Reduction Reaction Catalysts with Excellent Reactivity and Exceptional Stability by Embedding Co<sub>x</sub>O<sub>y</sub> Nanoparticles into Nitrogen-Doped Carbon. *Submitted*
3. Fundamental study of the interaction between trimethyl aluminum (TMA) and organic functional group (–OH, –NH<sub>2</sub> and –NO<sub>2</sub>). *In preparation*
4. Lianbing Zhang, Le Li, Alessandra Di Penta, Unai Carmona, **Fan Yang**, Regina Schöps, Matthias Brandsch, José L. Zugaza, Mato Knez, H-Chain Ferritin: A Natural Nuclei Targeting and Bioactive Delivery Nanovector. *Advanced Healthcare Materials*. 2015, **4**, 1305-1310.
5. Le Li, Maider Muñoz-Culla, Unai Carmona, Maria Paz Lopez, **Fan Yang**, Cesar Trigueros, David Otaegui, Lianbing Zhang, Mato Knez, Ferritin-mediated siRNA delivery and gene silencing in human tumor and primary cells. *Biomaterials*. 2016, **98**, 143–151.



---

# Acknowledgements

First of all, I would like to express my deepest grateful for my supervisor Prof. Dr. Mato Knez, for offering me the opportunity to conduct the interesting research here in nanoGUNE. Dr. Mato Knez has always been open and supportive for all my work and experiments, even sometimes those sounded a little bit crazy or weird. I sincerely appreciate all the inspiring discussions, valuable suggestions and constructive comments.

I also thank my colleague Dr. Lianbing Zhang, who has been helping me in both life and research problems since the first day I came to Donosti. Without him and his wife Dr. Le Li, my life would have been much tougher here.

I want to thank our technician Mikel Beltrán, whom I always bothered for ALD programming, the pumps, the IR set-ups and many other things. Without his help, the experiments might not have been conducted and finished. I also want to thank my colleague Unai Carmona for his help. He was a research collaborator and a language teacher for me not only for Spanish, but sometimes also Basque. Many thanks to all the other group members: Dr. Chaoqiu Chen, Dr. Ana Zuzuarregui, Dr. K. Gregorczyk, Weike Wang, Itxasne Azpitarte for the interesting and helpful discussions about science and life, and the great atmosphere in the group.

Many thanks to Dr. Christopher Tollan and Prof. Dr. Andrey Chuvilin in the Electron-Microscopy group for their great help in checking my samples with the Microscope. Thanks also to all the other colleagues in nanoGUNE: Ralph Gay for helping me to make those essential small pieces for my experiments; Dr. Wiwat Nuansing, Dr. Thales Oliveira, and Dr. Mitsuhiro Okuda for giving me samples and lending me some laboratory consumables; all the technicians, for their generous help on solving problems I met using those equipments; all the colleagues in nanoGUNE, for the great joy, the nice atmosphere and everything.

I am also thankful to my collaborators from the Centro de Física de Materiales in Donosti in Spain, Dr. Celia Rogero, Dr. Jens Brede, Mr. Mikel Abadia for their great help with the XPS characterization and discussion.

Many thanks to Miss Abulati Hairisha from the Tyndall National Institute, University College Cork in Ireland, for her great help on the theoretical calculations.

---

I also thank all the Chinese friends here: Dr. Lianbing Zhang, Dr. Le Li, Dr Chaoqiu Chen, Dr Xiangnan Sun, Dr. Wenjin Yan, Weike Wang, Dr. Peining Li, Kaike Yang, Jian Li, Shu Chen. I enjoyed quite a lot the time we spent together. Thanks for your company, I am much happier and less home sick.

Last but most importantly, I want to thank my parents, my sister. Without your support and love, I could never make it here. I want to share my every happiness and joy with you.